The Impact of Cosmic Ray and Ionizing Radiation on Galactic Structure and Associated Observational Diagnostics

by

Francisco Holguin

A dissertation submitted in partial fulfillment
of the requirements for the degree of
Doctor of Philosophy
(Astronomy and Astrophysics)
in The University of Michigan
2022

Doctoral Committee:

Associate Professor Mateusz Ruszkowski, Chair
Professor Oleg Gnedin
Professor Lee Hartmann
Associate Professor Carolyn Kuranz
Assistant Professor Hsiang-Yi Karen Yang

Francisco Holguin

opaco@umich.edu

ORCID iD: 0000-0002-8732-5427

ACKNOWLEDGEMENTS

Over the 6 years I have been a graduate student slowly putting together this thesis, I have benefited from the support of many people.

I thank the community at the University of Michigan, Department of Astronomy. Specifically, the graduate students for the collaborative atmosphere. Hearing about astronomy research across all scales in astronomy, from planets to galaxy clusters, reminded me of the bigger picture that my own work fits into. I also of enjoyed participating in many intramural sports as a part of the department team. I always looked forward to a game after a hard work day. Ryan Farber, I appreciate having working along side you for almost my entire time at Michigan. I benefited greatly from your advice, and being a year behind you I gained insight into what the next year would bring . It was great to see you again in Germany. I also thank the department office members and Ted Bergin for their generous support of my well-being. I thank my advisor, Mateusz Ruszkowski. I appreciate all of the support over the last 6 years through many road blocks and deadlines. A large part of my growth as a researcher has come from your guidance through research and navigation of the scientific community at large.

I thank all my research collaborators. In this thesis, Alex Lazarian and Chris Hayward greatly aided in conceptualizing and polishing the first and second projects respectively. I appreciate Jess Werk's valuable expertise for the third project. I also appreciate collaborators at Los Alamos National Laboratory, for research that is not in this thesis, but nonetheless expanded my scientific skills.

I acknowledge Megan Hagenhauer and John Basler for allowing me to rent a room in their house for most of my time at Michigan. Securing a place to live was the first challenge of moving to the area and I ended up in the perfect situation. I enjoyed my time living with you all, especially learning about numerous board games.

I thank my family for being in my life. The PhD process is long enough that younger siblings grow up a lot from start to finish. Tessy, I am happy to see that you found a solid career path and even start graduate school. It was great to see Ana and Oly finish high school, become adults, and start to find their own professional interests. I am incredibly thankful for my parents hard work throughout my life that has allowed me to follow this career path. I am grateful for my partner, Ashling, for all the support through the entire PhD process, especially for being willing to proofread documents.

The final acknowledgement is specifically to my mom Olivia and grandmother Ana, two people whose presence has influenced me the most. Their aptitude for mathematics and scientific thinking has been clear throughout my life. Under different circumstances, they would have long since presented their own PhD theses. Their support is what allowed me to begin the learning process leading to this thesis.

TABLE OF CONTENTS

LIST OF FIGURES

Figure

LIST OF TABLES

Table

ABSTRACT

Observations of galaxies have uncovered a complex, multiphase galactic environment structured by the effects of feedback mechanisms within and beyond the galaxy. Still, the exact properties of the galactic and circumgalactic medium remain uncertain. Plasma properties derived from diagnostic ions depend on the ionization mechanism assumed, for example collisional or photoionization. In other words, proper modeling of the radiation field is important. By analyzing cosmological galaxy simulations, I find that that the stellar contribution to the radiation field generally dominates up to roughly 0.1 - 0.2 $R_{\rm vir}$, so analyses within that radius should consider stellar sources in ionization assumptions. At the same time, cosmic rays have emerged as a potentially significant feedback mechanism, acting as a non-thermal pressure source, as well as imparting energy and momentum into gas. It is still unclear as to which model of cosmic ray transport is the most realistic. I conduct three dimensional simulations of a section of a Milky Way-like galactic disk. I study a model of cosmic ray transport that includes the effects of the turbulent and magnetized medium, and show that the galactic wind properties are sensitive to the strength of turbulence. Furthermore, I conduct similar galaxy disk section simulations, focusing on both radiative and cosmic ray feedback. I describe methods for producing synthetic spectral line diagnostics from highly-ionized species in simulations and find that models of fast cosmic ray diffusivity without cosmic ray streaming heating best agree with observed diagnostic values. This work illustrates how ultraviolet diagnostics could be useful tools to help differentiate between radiative and cosmic ray feedback models.

CHAPTER I

Introduction

1.1 Discovery of a Universe Beyond the Milky Way

Over the last 500 years, our astronomical understanding of the natural world in which we reside has undergone repeated refinements, including several large paradigm shifts. One such discovery in the last century was the idea that our own galaxy, the Milky Way, is simply one of many that populate the enormous volume of the observable universe. Evidence for this idea began accumulating at the turn of the 20^{th} century, leading to the 1920 'Great Debate' between Harlow Shapley and Heber Curtis (*Smith*, 1982), who debated whether observed spiral nebulae belonged to the Milky Way or if they were entire 'island universes' in their own right. Within the following decade, evidence pointed to the latter, drawing a new astronomical picture of a vast universe filled with individual galaxies and opening up extensive questions about the physical processes that led to the present-day universe.

Since then, numerous investigations have yielded an increasingly more accurate picture of the complicated multiscale processes driving the creation, evolution, and interaction of galaxies, as well as the medium in between. One of the most famous advances is the discovery of existence of dark matter. Evidence for unseen matter in an extended galactic halo began accumulating at roughly the same time as the 'island universes' (*Bergström and Hooper*, 2006), in particular key analysis of galaxy

clusters by Fritz Zwicky (*Zwicky*, 1937) and increasingly more thorough studies of galactic rotation culminating in the seminal paper led by Vera Rubin (*Rubin and Ford Jr*, 1970). The gravitational potential set by dark matter is the backdrop on which numerous physical processes shape the thermal and dynamical structures of a galaxy.

1.2 Thermal Equilibrium Models

Examining the equilibrium of galactic sources and sinks of thermal energy leads to a key insight, the idea of a two-phase medium within the galaxy (originally proposed by *Field et al.* (1969)). Atomic spectroscopic physics (i.e. *Sansonetti and Martin*, 2005), a theoretically and experimentally well-studied field, plays the primary role in determining both the heating and cooling rates of interstellar gas. We first discuss the cool and warm ($T < 10^4$ K) interstellar medium, characterized by energy injection processes on long timescales, and then discuss the hotter medium, dominated by shorter burst energy injections from supernovae.

Due to the tenuous nature of interstellar gas, thermal energy losses in gas are dominated by optically thin, collisionally-excited radiative losses. Interstellar gas composition is largely hydrogen (90 percent); however, the metal (heavier than helium) lines, particularly forbidden atomic transitions [CII] 158 μm and [O I] 63 μm, dominate the contribution to cooling (*Dalgarno and McCray*, 1972; *Draine*, 2010). It is not until $T \gtrsim 10^4 K$ that hydrogen transitions become significant. The total cooling rate in units of [erg s^{-1} cm^{-3}] is denoted by $\Lambda(\rho, T)$.

Thermal energy input in the interstellar medium (ISM) is dominated by ionization processes, namely ionizations by photons around the Lyman limit (13.6 eV) and by galactic cosmic rays (see *Osterbrock and Ferland* (2006) and *Draine* (2010) for a detailed description). Radiative heating $H_{\rm rad}$ occurs by the ionization of both single atoms (H, He, etc.) and interstellar dust (by photons below the Lyman limit), usually

labeled as 'photoionization' and 'photoelectric' heating respectively. The interstellar radiation field is set by the stars in a galaxy and by the extragalactic background (e.g. *Faucher-Giguere et al.*, 2009; *Haardt and Madau*, 2012). Photoionization heating in the Extreme Ultraviolet (EUV) ($h\nu > 13.6$ eV) part of the spectrum can contributes a heating rate $H_{\rm rad,EUV} \sim 10^{-24}{\rm ergs}^{-1}{\rm cm}^{-3}$ (e.g., *Reynolds et al.*, 1999). Figure 1.3a shows an optical image of a giant star forming nebula, the source of many of these ionizing photons. Photoelectric heating in Far Ultraviolet (FUV) (4.5 eV $<$ hν $<$ 13.6 eV) part of the spectrum contributes a heating rate $H_{\rm rad,FUV} \sim 10^{-25}{\rm ergs}^{-1}{\rm cm}^{-3}$ (*Reynolds and Cox*, 1992; *Weingartner and Draine*, 2001b). Ionization of atoms by galactic GeV cosmic rays provide a heating rate $H_{\rm CR,e} = 10^{-27}{\rm ergs}^{-1}{\rm cm}^{-3}$ (*Dalgarno and McCray*, 1972; *Draine*, 2010), for typical ionization rate of $\Gamma \sim 10^{-16}$ s^{-1} per H atom.

In a steady-state equilibrium interstellar medium with $H = \Lambda$, the total pressure P is constant, allowing us to connect the density n and temperature T via an ideal equation of state $P = nkT$ and solve the heating-cooling equilibrium equation. Figure 1.1 shows a plot of temperature vs. pressure for typical interstellar conditions. For pressures between 3000-4500 cm^{-3} K (number densities $n \sim 1 - 10$ cm^{-3}) there are three solutions at a given pressure, with the two stable solutions existing at $T \sim 200$ K and $T \sim 8000$ K. So we expect a colder, neutral phase (CNM: cold neutral medium) and a warmer phase (WNM: warm neutral medium) respectively, just below the temperature of hydrogen collisional ionization.

The two-phase interstellar medium is a useful picture for the neutral medium; however, this model does not include the significant and relatively rapid energy input of $\sim 10^{51}$ ergs per supernova occurring within the galactic disk. As a supernova remnant expands though the interstellar medium, it significantly heats gas via shock heating and sweeps material away from the galactic disk (the earliest solutions of which is the famed self-similar Sedov-von Neumann-Taylor blast wave *Sedov*, 1946;

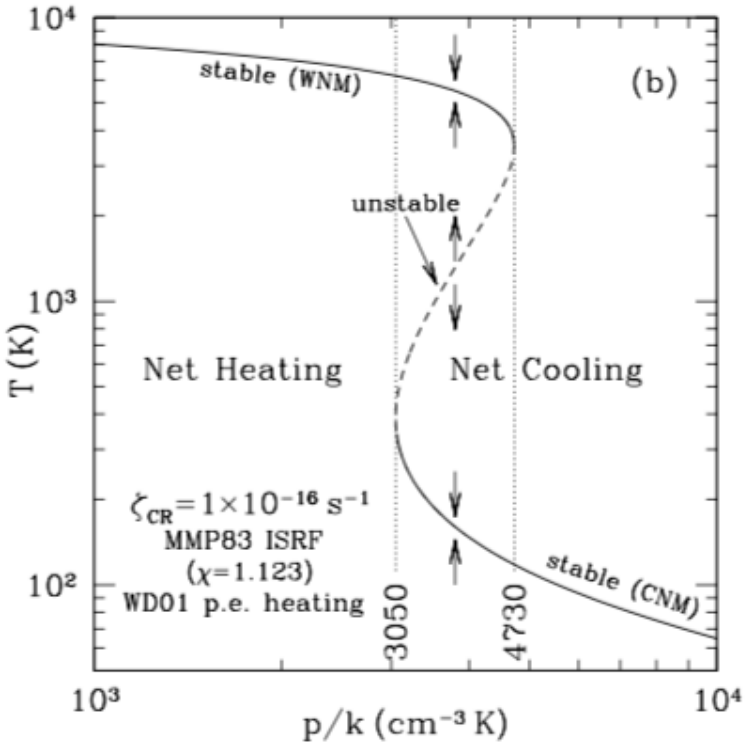

Figure 1.1: Figure from *Draine* (2010). Equilibrium temperature vs. pressure curve assuming typical heating and cooling in the interstellar medium. Between pressures of roughy 3000 and 4000 cm^{-3}K there are three possible gas phase solutions, the intermediate temperature is unstable.

Taylor, 1950). The cooling function (e.g. *Sutherland and Dopita*, 1993) above $T = 10^4$ K has a local minimum at $T = 10^6$ K and the cooling timescale is long on galactic timescales; shock heated gas at $T = 10^6$ is expected to be long-lived. *McKee and Ostriker* (1977) analytically examined the evolution of a supernova remnant as it interacts with the surrounding clumpy, multiphase medium and experiences radiative losses. They concluded the existence of a hot, ionized medium (HIM; $T \sim 10^6$ K) produced by galactic supernova energy injections and in pressure equilibrium with the CNM and WNM.

The three-phase ISM is a useful foundation on which to add more detailed models of galactic feedback processes. Detailed observations of the Milky Way's interstellar medium have found that the values of thermal, turbulent, magnetic field, and cosmic ray energy densities are all roughly eV/cm^3 (*Cox*, 2005; *Beck and Krause*, 2005). This equipartition of energy suggests that we must consider these additional physical phenomena in galactic model.

1.3 Galactic Feedback Models

A galaxy is a complex system of internal and external processes that couple non-linearly to shape its thermal and dynamical structure. In this thesis, we focus on halos of Milky Way mass or below, where stellar feedback is dominant. Figure 1.2 shows a galactic wind, a multiphase galactic phenomena that is observed across the universe (see the review by *Veilleux et al.*, 2005). The image is a multi-wavelength composite of M82, which is experiencing a strong galactic outflow. The blue color traces x-rays from the hot material powering the outflow out of the disk (traced by star light in green) and the red color traces infrared emission from interstellar dust in the colder gas being pushed far out of the galaxy.

The hot gas driving these outflows is likely powered by energy from supernovae and stellar winds. *Chevalier and Clegg* (1985) derives the solutions to the steady-

Figure 1.2: Multi-wavelength composite of M82 showing an outflow driven by hot gas. Blue: 1.5 keV X-rays. Green: stellar emission. Red: 8 μm infrared emission from dust. Credit: NASA/JPL-Caltech/STScI/CXC/Univ. of Arizona.

state, asymmetric hydrodynamic fluid flow assuming constant momentum and energy input at small radii. They defined useful parameters for characterizing the wind: $\alpha = \dot{E}_{\rm hot}/\dot{E}_{\rm SN}$, the thermalization efficiency and the instantaneous mass loading factor $\beta = \dot{M}_{hot}/{\rm SFR}$. They find that for reasonable parameters in M82 (e.g. *Strickland and Heckman*, 2009), such as a wind velocity ~ 2000 km/s and $\alpha \sim \beta$, the wind is made up of very hot $T \sim 10^7$ K gas. Figure 1.2 shows this hot, x-ray emitting gas in blue. The figure also shows the presence of interstellar dust, which exists in much colder gas. The presence of this cold phase suggests additional complexities that would allow the development of a multiphase wind.

Galactic winds in both low and high redshift galaxies have been observed to have multiphase components (see *Zhang*, 2018, and references within). The origin of these phases is still uncertain. For example, colder, denser material in the galactic midplane can be pushed out via ram pressure by the fast, hot phase or the cold phase could

condense out of the hot phase at larger radii. Similar works following *Chevalier and Clegg* (1985), which include radiative cooling, predict the existence of colder winds due to cooling of hot gas and also explore the α and β parameter space (e.g. *Thompson et al.*, 2016; *Bustard et al.*, 2016). In these models, existing cold material near the midplane is unable to survive interactions with the hot gas. Other wind launching mechanisms could be able to transport the colder phases of gas directly from the galaxy to significant fractions of the viral radii and even beyond the halo.

Radiation pressure from massive stars can also drive cold, neutral material out of the galaxy, since neutral material as a high interaction cross section with ionizing radiation. *Murray et al.* (2011) found that while one dimensional radiation pressure-driven winds might not accelerate gas to large velocities (i.e. thousands of km/s), this pressure is able to produce slower, but continuous outflows beyond 100 kpc. These winds however would only be expected in strongly star bursting galaxies. More comprehensive models adding inflow/outflow and cloud interaction/evaporation, like those in *Efstathiou* (2000), are able to produce a large-scale outflow in quiescent galaxies. Cosmic rays are another mechanism that could efficiently produce a multiphase galactic wind.

1.3.1 Cosmic Ray Observations and Production

Cosmic rays were first detected in ground based experiments (i.e. *Wulf*, 1910; *Pacini*, 1912) and their extra-terrestrial origin was confirmed by Victor Hess's atmospheric balloon experiments (*Hess*, 1912) leading to the 1936 Nobel Prize in Physics. The term 'cosmic ray' is a broad term that refers to any relativistic charged particles of natural origin. Cosmic rays consist primarily of protons, with lower abundances of higher mass nuclei (e.g. *Reedy et al.*, 1983; *Mueller et al.*, 1991). Electrons also contribute to the cosmic ray flux. More recently, antimatter has been found to contribute a small amount of cosmic ray flux (i.e. *Accardo et al.*, 2014). *Grenier et al.*

(a) Image of NGC 604 (located within M33), a giant HII region where massive stars are born. These massive stars emit ionizing photons that escape into the surrounding ISM/CGM. Credit: Hui Yang (University of Illinois) and NASA/ESA.

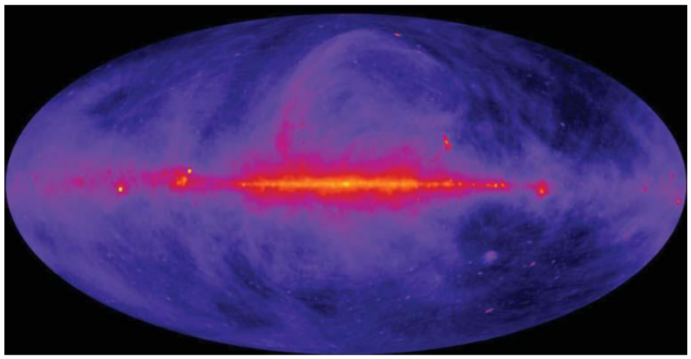

(b) All-sky map of 408 MHz synchrotron radio emission from cosmic ray electrons. Credit: NASA SkyView, Max-Planck Institute fur Radioastronomie.

Figure 1.3: Images showing (a) the origin of ionizing radiation from massive stars and (b) radio emission tracing cosmic rays around the Mikly Way.

(2015) shows recent references for energy flux and abundance measurements of many cosmic ray species.

The cosmic ray energy spectrum spans an extremely large energy range, extending from low-energy, $E \sim$ MeV, to a peak flux at $E \sim$ GeV, all the way to ultra-high energy of $E > 10^{12}$ GeV (*Hillas*, 2006). The lower MeV energy part of the observed cosmic ray spectrum is of solar origin, as the MeV cosmic ray flux is correlated with solar activity (*Pomerantz and Duggal*, 1974). GeV cosmic rays are thought to be of galactic origin, an idea first presented by *Baade and Zwicky* (1934) and *Zwicky* (1939). Ultra-high energy cosmic rays require acceleration mechanisms thought to be found in some of the most extreme galactic environments, such as active galactic nuclei. Due to their high energy, these particles are less deflected by large scale magnetic fields en route from the source to observer, allowing some works to correlate cosmic ray observations with known high-energy extragalactic sources (*Zaw et al.*, 2009; *Globus and Piran*, 2017).

As the peak of the cosmic ray energy spectrum is at GeV energies, these cosmic rays are expected to produce the bulk of influence on galactic processes. Direct measurement of galactic GeV and lower energy cosmic rays are challenging due to modulation at the heliosphere (*Strauss and Potgieter*, 2014), with in-situ measurements only recently possible due to the Voyager probes entering the heliopause (*Cummings et al.*, 2016). The effect of solar modulation decreases with higher particle energy, which by $\sim 50 - 100$ GeV is not significant. Theoretical calculations in tandem with indirect cosmic ray signatures have been the primary method in our understanding of the acceleration of cosmic rays and their interaction with the galactic environment. Figure 1.3b is an image showing synchrotron emission from cosmic ray electrons around the galaxy. These cosmic ray electrons are expected to trace the cosmic ray protons, so cosmic ray protons exist around the galaxy. Extragalactic surveys such as the CHANG-ES survey (*Wiegert et al.*, 2015), have detected large radio halos around

galaxies, demonstrating that cosmic rays have a significant presence even outside of the galactic disk.

The observed distribution of cosmic rays is isotropic (*Nagashima et al.*, 1998), which obscures the origin of galactic cosmic rays. Cosmic rays experience hadronic interactions with other nuclei, which produce gamma rays. Observed gamma ray emission from supernova remnants suggest that they are factories of cosmic rays. The detection of pion-decay signatures, the products of cosmic ray-interstellar medium interaction, confirms supernova remnants as sources of cosmic ray acceleration (*Ackermann et al.*, 2013).

The exact mechanisms of cosmic ray acceleration are still unclear, although significant progress has been made in discovering and characterizing possible mechanisms. Early work by *Fermi* (1949) proposed what is now known as second order Fermi acceleration, where interstellar clouds act as moving magnetic mirrors that reflect particles, imparting energy with each reflection. The role of the supernova shock has been studied extensively as a more efficient method of particle acceleration. It is an example of first order Fermi shock acceleration and naturally produces a power law in energy. Cosmic rays repeatedly cross the shock boundary, gaining a net increase in energy, and eventually escaping when they reach a threshold energy (e.g. *Krymskii*, 1977; *Blandford and Ostriker*, 1978; *Bell*, 1978). The details of this theory of *Diffusive Shock Acceleration* have been continuously updated since its first inception (see *Schure et al.*, 2012; *Bell*, 2013, for reviews), and modern kinetic/hybrid simulations have had success in a variety of observational predictions. Other astrophysical shocks, such as in stellar winds or in the interstellar medium, could also have a relevant contribution to the cosmic ray population.

1.3.2 Cosmic Ray Transport

Cosmic ray transport through the galactic environment is an active area of research with numerous unresolved questions. The range of scales relevant to the plasma physics of charged particle transport and the resulting galactic effects is extremely large: the gyroradius of GeV cosmic rays is $\sim$ AU for a typical $\sim \mu G$ galactic magnetic field, while galaxy scales are $\sim$ kpc ($\sim 10^8$ AU). Additionally, beyond cosmic ray physics, descriptions of a magnetized, turbulent medium are still incomplete. For the following section, we limit our discussion to GeV cosmic rays as this is the energy range relevant for dynamical and thermal effects on the galaxy.

There are a few clues that reveal key insights of how cosmic rays behave in a galactic environment. First, the isotropic nature of the cosmic ray flux demonstrates that the particles are significantly deflected from their sources. The scale height of the Milky Way's 'thick' disk is $\sim$ 1 kpc (*Gilmore and Reid*, 1983; *Chen*, 1997). Thus, freely propagating cosmic rays can escape the disk in less than 10^4 yr, an extremely short timescale considering the observed ISM cosmic ray energy density $e_{\rm cr}$ of 1 eVs^{-1}cm^{-3}. We can estimate the galactic supernova rate by dividing the total cosmic ray energy in the ISM by the cosmic ray energy injection rate per supernova within a cosmic ray residence time.

$$R_{\rm SN} \sim (e_{\rm cr} V_{\rm ISM})/(E_{\rm SN,cr}\tau_{\rm cr}), \tag{1.1}$$

assuming a cylindrical volume $V_{\rm ISM} \sim$ 1 kpc π(10 kpc)^2 for the Milky Way, a cosmic ray energy injection rate of $E_{\rm SN,cr} = 10^{50}$ ergs per supernova, and cosmic ray residence time $\tau_{\rm cr}$. Given the extreme luminosity of supernovae, the galactic supernova rate is well-constrained to 1 supernova per century (*Rozwadowska et al.*, 2021). For $\tau_{\rm cr} = 10^4$ years, roughly 1500 supernovae/century are needed, greatly inconsistent observations of the Milky Way throughout the last few centuries. Another clue about galactic

cosmic ray transport comes from abundance ratios of primary to secondary elements (e.g. boron to carbon). The secondary elements are over abundant in cosmic rays compared to ISM values because they are produced via spallation interations with ISM matter; these primary-secondary ratios act as diagnostics for the integrated ISM material ('grammage': the column density of matter that a cosmic ray interacts with from source to detection) that cosmic rays pass though and their residence time in the galaxy (*Strong et al.*, 2007). A typical diffusion coefficient from such measurements is $D \sim 5 \times 10^{28}$ cm^{2}s^{-1}, leading to a cosmic ray residence time of ~ 10 Myr within the thick disk , which is much longer than the free streaming estimate. Using $\tau_{\rm cr} = 10^7$ years in Eq. 1.1, we find a rate of 1.5 supernovae per century, consistent with the actual Milky Way rate.

Since the cosmic ray gyroradius is small compared to the galaxy, we expect cosmic rays to travel along the tangled galactic magnetic field lines. Many works have characterized transport in this context, including more standard results such as field line wandering and drifts (gradient and curvature) (e.g. *Giacalone*, 1998; *Schlickeiser and Jenko*, 2010) and more complicated mechanisms such as anomalous cross-field transport in a chaotic magnetic field (e.g. *Casse et al.*, 2001)

The cosmic ray residence time as a function of energy is inconsistent with confinement based purely on large-scale magnetic field geometric structure (*Zweibel*, 2013). The highly nonlinear, small-scale plasma physics interaction between cosmic rays and the magnetized ISM is essential to examine in detail. The general evolution of the cosmic ray distribution function can be written as a collisionless Boltzmann equation (*Pfrommer*, 2020):

$$\begin{aligned}\frac{\partial}{\partial t}f + \frac{\partial}{\partial x}v(x,p)f =& \frac{-1}{p^2}\frac{\partial}{\partial p}p^2 A(x,p)f + \frac{1}{p^2}\frac{\partial}{\partial p}p^2\Gamma(x,p)\frac{\partial}{\partial p}f \\ &+\frac{\partial}{\partial x}D(x,p)\frac{\partial}{\partial x}f + s(x,p),\end{aligned} \tag{1.2}$$

where f is the distribution function, v is the bulk velocity, p is the momentum, A

encodes cosmic ray energy gain/loss, D is the diffusion coefficient, and s is a source term. Hadronic and Coulomb losses are the dominant components of $A(x,p)$. *Zweibel* (2013) provides a concise summary of particle-magnetohydrodynamic (MHD) wave interactions relevant to cosmic rays in the galactic environment. Resonant scattering of cosmic rays by MHD waves is thought to be the dominant scattering mechanism.

Two main theories of effective cosmic ray confinement have been proposed, extrinsic turbulence and self-confinement. Extrinsic turbulence refers to the direct scattering of cosmic ray particles by the existing turbulent cascade of MHD waves, driven by galactic feedback such as supernovae. *Zweibel* (2013) notes that turbulence is unlikely to efficiently scatter cosmic rays, as the driving scale of $\sim 10 - 100$ pc is well-above the cosmic ray gyroradius and the effects from the smaller length scale part of the turbulent cascade are likely to cancel out over a gyro orbit. Although more work is needed before ruling out this senario.

In this work, we focus on the self-confinement model of cosmic ray transport. In this model, cosmic ray motion through the ISM is unstable, leading to generation of MHD waves that ultimately confine cosmic rays. The streaming instability (e.g. *Wentzel*, 1968; *Kulsrud and Pearce*, 1969) occurs when cosmic rays exceed the plasma Alfvèn speed V_A (usually $\ll c$). Other astrophysically relevant instabilities have been identified, such as the Bell (*Bell*, 2013) and the pressure-anisotropy (*Zweibel*, 2020) instabilities, however, we focus on the streaming instability as it is the most well-studied in the literature to date. The growth rate $\Gamma_{\rm st}$ of Alfvèn waves due to the streaming instability is

$$\begin{aligned}\Gamma_{\rm st} =& \frac{\pi}{4}\frac{\alpha-1}{\alpha}\Omega_0\frac{n_{\rm cr}(<p_{\rm min})}{n_{\rm i}}(\frac{V_{\rm D}}{v_{\rm A}}) \\ =& \Gamma_{\rm st}(n_i, n_{\rm cr}, B, V_{\rm D})\end{aligned} \tag{1.3}$$

assuming a power law distribution $f \propto p^{-\alpha}$ and where n_i is the plasma ion density, $v_{\rm D}$ is the bulk velocity of the cosmic rays along the mean magnetic field, $n_{\rm cr}$ is the

cosmic ray number density, $|B|$ is the magnetic field strength, Ω_0 is the gyro (Larmor) frequency, μ is the cosine of the pitch angle (relative to mean field line), m is the particle mass, and $p_{\rm min} = m\Omega_0/k$ is the minimum particle momentum to resonate with the waves. The positive dependence on $n_{\rm cr}$ and inverse dependence on $n_{\rm i}$ intuitively makes sense because more cosmic rays results in more generated Alfvèn waves, while higher plasma density makes it more difficult to generate those waves. The larger growth rate with gyro frequency (and thus magnetic field strength) reflects the fact that a more strongly magnetic system will respond proportionally powerfully to disturbances from cosmic ray propagation.

Cosmic rays are scattered by these waves, illustrated in Figure 1.4 by a schematic of this process in the frame of reference of the Alfvèn wave. A charged particle moving along a uniform magnetic field will gyrate around the field uniformly. When there is a transverse Alfvèn wave along the path, careful accounting of the $u \times B$ magnetic force along the particle orbit shows that there is a net force opposite the direction of particle velocity parallel to the magnetic field. By conservation of kinetic energy, perpendicular velocity increases. After many wave interactions, the parallel velocity is significantly reduced. In the lab frame, this means that the bulk motion of a population of cosmic rays is reduced to $v_{\rm A}$, the speed of Alfvèn wave propagation and the distribution is now isotropic. This particle-wave interaction also produces a collisionless heating (*Wiener et al.*, 2013b) mechanism for the medium, which provides $H_{\rm cr} = -v_{\rm A} \cdot \nabla P_{\rm cr}$ of energy losses from the cosmic rays to thermal energy.

Confining MHD waves are damped by various processes, so net cosmic ray transport will depend on the equilibrium of the wave growth instability and the wave damping $\Gamma_{\rm damp}$. Many wave damping processes are still poorly understood, but progress has been made via quasi-linear analysis. Wave damping mechanisms include ion-neutral friction (*Kulsrud and Pearce*, 1969), non-linear Landau damping (*Foote and Kulsrud*, 1979), interstellar dust (*Cramer et al.*, 2002), and turbulent damping (e.g. *Farmer*

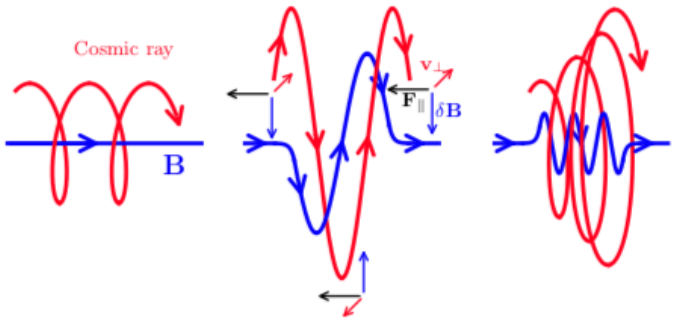

Figure 1.4: Diagram illustrating the gyromotion of a cosmic ray as it interacts with an Alfvèn wave. The result is a net force on the cosmic ray against the direction of particle motion. Credit: Jacob & Pfrommer, accessed from *Pfrommer* (2020), used with permission.

and Goldreich, 2004). Advances towards a more complete description of MHD turbulence (see *Goldreich and Sridhar*, 1995; *Yan and Lazarian*, 2004; *Lazarian*, 2016) have allowed better modeling of cosmic rays in the galactic environment, such as work completed for this thesis in *Holguin et al.* (2019) found in Chapter 2.

1.3.3 Cosmic Rays in a Galactic Context

Due to the small cosmic ray gyroradius compared to galactic scales and assuming weak anisotropy, we can simplify the equations by taking moments of Eq. 1.2, resulting in two conservation equations for momentum and energy in cosmic rays (*Zweibel*, 2013). These equations can by combined with traditional fluid equations, such as those studied *McKee and Ostriker* (1977). The resulting system of equations treats cosmic rays as a separate, collisionless fluid (with a relativistic equation of state) that advects with the plasma with diffusion, as well as energy and momentum exchange. We can employ a diffusion coefficient or directly solve for the cosmic ray bulk speed $V_{\rm D}$ via the equation $\Gamma_{\rm st}(n_i, n_{\rm cr}, B, V_{\rm D}) = \Gamma_{\rm damp}$, where the damping rate will depend on parameters of the cosmic rays and plasma (*Wiener et al.*, 2013a). In this two-fluid model (thermal and non-thermal fluids) (see *Yang et al.*, 2012, and references therein) cosmic rays play an important role in the system, as they do not experience

radiative losses, thereby helping store energy in the system. The cosmic ray fluid acts as an additional pressure support against gravitational collapse for star formation, experiences energy and momentum exchange with the plasma, and can accelerate gas due to large scale pressure gradients.

Cosmic rays have been added to idealized wind models (i.e. *Ipavich*, 1975; *Breitschwerdt et al.*, 1991; *Everett et al.*, 2008; *Wiener et al.*, 2017a) and in these models cosmic rays are able to continuously accelerate gas, even outside of the galaxy where thermal feedback is small, to large velocities matching observed fast $\gtrsim$ 1000 km/s outflows. These models also suggest that cosmic ray-aided winds have the potential to explain other observations of galaxies in γ-rays, x-rays, and radio. More extensive analysis, in particular with three-dimensional MHD galaxy simulations, is needed to further evaluate how cosmic rays influence galaxy evolution. Section 1.4 discusses progress on computationally expensive modeling of galaxies.

1.3.4 Circumgalactic Medium

We have discussed many feedback mechanisms that operate primarily from within or near the galactic disk. These feedback effects extend far beyond the galaxy. Careful accounting of baryons in galaxies has shown that galaxies are baryon-deficient relative to the cosmological average (*Bell et al.*, 2003): galactic feedback drives material far out of the galaxy and a complete accounting for these baryons is still debated. The circumgalactic medium (CGM) is the region between the galaxy and edge of the galactic halo, which recently has been pointed to as a significant reservoir of baryons (see *Tumlinson et al.*, 2017). The CGM is particularly important because it is the interface of internal (e.g. stellar feedback) and external (e.g accretion, halo mergers) galactic processes. Galactic and extragalactic feedback leaves an imprint on the CGM, therefore understanding the multiphase state of the CGM plasma will reveal key information about galaxy evolution.

Determining the properties of the CGM is challenging due to its low density, current gaps in observational instruments in wavelength (e.g. the hot phase is currently undetectable), and modeling uncertainties. Nonetheless, observational and theoretical modeling of the CGM has been increasingly more insightful. *Tumlinson et al.* (2017) provides a comprehensive summary of the state of the field. Absorption line studies have been the primary source of information about the CGM. A variety of diagnostic ions have been detected, from low (e.g. C-II, C-III, Si-II, Si-III), intermediate (e.g. C-IV, Si-IV, and O-IV), and high (e.g. O-VII and Mg-X) ionization states, which confirms the complex, multiphase structure of the CGM. The detection of intermediate ions in particular suggest a significant reservoir of gas at $10^5 - 10^6$ K, in between the traditional three-phase medium. Identifying the underlying plasma responsible for these ions is challenging (e.g. *McQuinn and Werk*, 2018). Absorption line observations measure the line-of-sight ion column density, so it is unclear for example whether the ions are found in numerous small or a few large clouds. Additionally the appropriate (non)equilibrium assumptions are unclear. For example, the calculated plasma state of the gas can be quite different based on assumptions of collisional or photo-ionization equilibrium, and whether the stellar or background radiation field modifies this analysis. Sections 3 and 4 of this thesis aim to illuminate some of the uncertainties related to the effects of the H ionizing spectrum on CGM diagnostics.

1.4 Development of Computational Models of a Galaxy

The development of many galactic feedback theories around the 1970's roughly coincides with the start of modern computing. Early simulations of galaxies were N-body simulations, representing a galaxy by a collection of particles and directly solving the graviational forces between them (*Von Hoerner*, 1963; *Aarseth and Hoyle*, 1963). *Moore* (1965) proposed 'Moore's law' which predicted that the number of transistors

would double every 1-2 years, a prediction that has remained quite accurate over the last 50 years. Modern processors can individually execute billions of operators per second. At the same time, algorithm development has made computers incredibly efficient at implementing physical models. For example, Tree (*Barnes and Hut*, 1986) and Fast-Multipole (*Greengard and Rokhlin*, 1987) methods have enabled computers to evolve many more particles than before per computational effort. The Millennium simulation (*Springel et al.*, 2005) followed more than 10 billion dark matter particles in a $\sim 700^3$ kpc^3 cube of the universe from redshift $z = 127$ to the present day.

Furthermore, the development of increasingly more complex three-dimensional hydrodynamic simulations has allowed us to initialize 'universe-in-a-box' experiments and observe galaxy evolution in real-time. The first hydrodynamic simulations appeared in the early 1990's, showing the evolution of thermal gas within a dark matter potential with simple prescriptions for heating/cooling (e.g. *Cen et al.*, 1990; *Katz and Gunn*, 1991). Subsequent works fine tuned models for cooling, star formation, and supernova injection, resulting in simulated galaxy populations that roughly matched observational 'laws' such the Kennicutt-Schmidt relation (*Kennicutt Jr*, 1998; *Stinson et al.*, 2006). One example issue in these models is the 'over-cooling' problem of supernova energy injection that hinders effective thermal feedback. When the supernovae are not properly resolved, the dense cells of gas quickly radiate most of the thermal energy away, severely reducing the effect of supernovae compared to analytic expectations. Various prescriptions are needed to avoid this issue.

As computational power increased, the impact of magnetic fields on galactic scales began to be studied in the late 2000's (*Wang and Abel*, 2009). It became clear that magnetic fields are naturally generated and self-sustained by the turbulent dynamo driven by evolution of the galaxy. Magnetic fields also provided the first non-thermal component coupled to the hydrodynamic equations. Magnetic fields help resist gas collapse, reducing the SFR, and shearing, helping ISM clouds remain intact. Turbu-

lence is another non-thermal phenomenon that has been modeled extensively. Turbulence can be implemented as a subgrid model evolving a separate field that is coupled to the hydrodynamics, also providing effects such as gas pressure support (e.g. *Schmidt et al.*, 2014).

The rapid computational advances in the last decade have allowed the development of highly realistic cosmological zoom-in simulations of galaxies. There are several examples of detailed simulations, but we mention the FIRE simulations (*Hopkins et al.*, 2014, 2018, 2020, 2022b) in particular. These simulations contain radiative cooling, star particle formation, star particle feedback (continuous mass loss and supernovae), radiative heating and pressure (including an approximate model of stellar particle radiation transport in several wavenlength bins), MHD effects, metal chemistry/evolution, and more recently cosmic rays. Comprehensive simulations have made it possible to study the the population properties of synthetic galaxies and compare to observational findings from large surveys.

The addition of cosmic rays and their transport in global three-dimensional galaxy simulations has only been computationally feasible in the last decade. Cosmic ray transport requires more stringent time step constraints compared to the hydrodynamics. Cosmic ray transport is usually treated simply by specifying the diffusion coefficient relative to magnetic field line directions (e.g. *Booth et al.*, 2013). Cosmic ray transport via the streaming instability can be treated similarly, with diffusion in the direction parallel to the magnetic field determined by the bulk cosmic ray speed $V_{\rm D}$, which is equal to $V_{\rm A}$ in the absence of MHD wave damping processes (*Uhlig et al.*, 2012; *Ruszkowski et al.*, 2017). In a realistic model including wave damping, cosmic ray transport will depend on the plasma properties of the local galactic environment. The first simulations of a section of a galactic disk accounting for ion-neutral (*Farber et al.*, 2018) and turbulent damping (*Holguin et al.*, 2019) suggest that cosmic ray microphysics can have a large impact on galaxy evolution. *Ji et al.* (2020) examined

the effect of cosmic rays in the CGM and found that cosmic ray-dominated pressure equilibrium allows the different gas phases to exist at roughly the same density. The colder, neutral phases in particular are able to exist at lower densities. Chapter 4 in this thesis discusses the implications of these changes of phase properties for plasma diagnostics in galactic simulations. Most recently *Hopkins et al.* (2021b) conducted a thorough investigation of the effects of many cosmic ray transport models within a cosmological context and found that cosmic ray feedback tends to be lessen with physically motivated transport and there is no clear model that stands out in the parameter space. Current cosmic ray transport also might be inconsistent with well-established observations *Hopkins et al.* (2021c), so even current simple models of transport may not be correct.

Significant advances are being made in cosmic ray transport algorithms which have allowed for higher simulation resolutions and a first look at energy dependent cosmic ray physics both in post-processing and recently by actually evolving the cosmic ray spectrum (e.g. *Yang et al.*, 2013; *Jiang and Oh*, 2018; *Thomas and Pfrommer*, 2019; *Hopkins et al.*, 2021a, 2022a). Computational challenges still remain. There are continued uncertainties in modeling the radiation field around galaxies and computational modeling of radiation is often prohibitively expensive. Understanding radiative effects on plasma diagnostics is especially key in studying the CGM, especially since cosmic rays also influence these diagnostics. Additionally, there are many uncertainties in how well subgrid models reproduce the underlying microphysics of cosmic ray transport. It is clear that smaller scale kinetic and hybrid-scale plasma simulations (e.g. *Haggerty and Caprioli*, 2020) will be essential in developing more realistic models of feedback.

1.5 Thesis Outline

In Chapter 2, we focus ionizing radiation, a feedback mechanism that produces uncertainty in theoretical and observational modeling. *Holguin et al.* (2022b) untangles the role of the stellar versus the background radiation field by calculating radial extent of stellar radiation in simulated galactic halos. This work finds that within $z < 3.5$, stellar radiation generally does not extend farther in the CGM than 0.2 $R_{\rm vir}$, and even less for $z < 1.5$. Analysis of the CGM outside of these regions likely can ignore the stellar contribution, while studies closer to the galaxy should account for the stellar component.

In Chapter 3, we describe work from *Holguin et al.* (2019), which ran three-dimensional coupled MHD+cosmic ray galactic-scale simulations with physically-motivated cosmic ray transport. This investigation produced the first simulations to include cosmic ray transport informed by on the state of the local magnetized and turbulent medium. The properties of the simulated galaxy are sensitive to the details of cosmic ray transport. In particular, the peak SFR is increased and the instantaneous mass loading factor of the wind is reduced with increasing levels of turbulence.

In Chapter 4, we explore both cosmic ray and ionizing radiation feedback within MHD+cosmic ray galactic-scale simulations. We develop and discuss a novel framework that integrates MHD simulation results with a *Cloudy*, a spectral synthesis code, allowing us to produce synthetic plasma diagnostics that depend on the three-dimensional, time-varying galactic structure, while remaining relatively computationally inexpensive.

Finally, we discuss conclusions from this thesis in Chapter 5.

CHAPTER II

Contribution of Stars Within the Host Galaxy to the Ionizing Radiation Field of the Circumgalactic Medium

2.1 Preface

For this chapter, I am the lead author, and it is coauthored by C. Hayward, X. Ma and the FIRE collaboration. This work is in preparation to be submitted to MNRAS.

2.2 Abstract

Elucidating the internal and external processes that shape the circumgalactic medium (CGM) is crucial for understanding galaxy evolution as the CGM is the interface between a galaxy and the rest of the universe. Characterizing the multiphase structure of the CGM reveals key details about these processes and their complex interactions. Absorption and emission diagnostics shed light on the phase and ionization structure of the CGM, but uncertainty about the ionizing radiation field may hamper inferences from such observations. Including ionizing radiation from local sources in photoionization models is significantly more complicated than is treating the metagalactic background field because the stellar ionizing radiation can

vary spatially and temporally depending on the evolution the galaxy. For this reason, local sources are typically ignored. To test this simplification, in this work, we investigate the contribution of stars within the galaxy to the CGM ionizing radiation field. We perform Monte Carlo radiation transfer on 12 cosmological zoom-in simulations from the Feedback in Realistic Environments (FIRE) project to quantify the radial extent of stellar ionizing radiation and determine the regions of parameter space in halo mass ($10^{10.5} - 10^{13}\,\mathrm{M}_\odot$) and redshift ($0 < z < 3.5$) in which stars within the host galaxy contribute appreciably to the ionizing radiation field as a function of radial distance from the galaxy. We find that on average, the contribution of stars within the galaxy is small beyond one-tenth of the virial radius, $R_{\rm vir}$, for $z < 1.5$. For $z > 1.5$, this transition radius is 0.1-0.2 $R_{\rm vir}$. For $M_{\rm halo} > 10^{12}\,\mathrm{M}_\odot$ and $z \sim 1.5 - 2.5$, the transition radius can exceed 0.2 $R_{\rm vir}$, but nowhere in the parameter space considered is the average transition radius greater than 0.4 $R_{\rm vir}$. We also compute the escape fraction of stellar ionizing photons at $R_{\rm vir}$, finding typical values of less than 0.1, except in higher-mass halos ($M_{\rm halo} \gtrsim 10^{12}\,\mathrm{M}_\odot$), which have consistently high values of $\sim 0.5 - 0.6$. Overall, our results indicate that for typical galaxies, it is reasonable to ignore the ionizing radiation from host-galaxy stars outside of 0.2 $R_{\rm vir}$.

2.3 Introduction

The evolution of galaxies from the early universe to the present day has been a long-standing challenge in astrophysics. The baryon content within a galaxy is depleted relative to the cosmological average (*Bell et al.*, 2003). Metals (*Songaila*, 2001) and dust (*Ménard and Fukugita*, 2012), formed deep in the galactic potential well, are observed in the galactic halo and intergalactic medium. Processes such as galactic winds (*Veilleux et al.*, 2005) transport metal-enriched gas out of the galaxy, while at the same time gas accretion onto the galaxy (*Fox and Davé*, 2017) replenishes the fuel supply for continued star formation. This cycle shapes the galactic dynamical

and thermal structure and ultimately results in the quenched galaxies seen today (*Peng et al.*, 2010). The properties of the circumgalactic medium (CGM), the region between the galactic disk and the virial radius, are closely tied with these physical processes shaping the galaxy, as the CGM is the interface between the galaxy and the intergalactic medium. Numerous process interact within the CGM, producing a complex and multiphase CGM structure: outflows and inflows not only transport material through the CGM (e.g., *Muratov et al.*, 2015; *Anglés-Alcázar et al.*, 2017a; *Hafen et al.*, 2019; *Pandya et al.*, 2021) but also drive turbulence (e.g., *Fielding et al.*, 2017); mergers between halos can strongly disturb the CGM (e.g., *Iapichino et al.*, 2013); thermal instabilities can develop (e.g., *McCourt et al.*, 2012); cosmic rays can further impart momentum into the gas (e.g., *Breitschwerdt et al.*, 1991; *Uhlig et al.*, 2012; *Booth et al.*, 2013; *Salem and Bryan*, 2014) and provide pressure that supersedes that of the gas thermal pressure (e.g., *Ji et al.*, 2020; *Butsky et al.*, 2020), all while experiencing various complicated and still debated coupling to the background medium (e.g., *Ruszkowski et al.*, 2017; *Farber et al.*, 2018; *Holguin et al.*, 2019; *Squire et al.*, 2021; *Hopkins et al.*, 2021b); radiation from the stellar sources (*Mathis*, 1986) and the metagalactic field can both heat and ionize gas (*Osterbrock and Ferland*, 2006). A complete understanding of galaxy evolution requires detailed investigation into these processes and their effects on the CGM.

Surveys of the CGM (e.g., *Tumlinson et al.*, 2017, and references therein) around galaxies have provided diagnostic information from which to begin analyzing the CGM. Despite the insight provided by these surveys, our picture of the CGM remains incomplete. The low density of the gas makes it challenging to observe emission lines, there are degenerate explanations for a given diagnostic, and we are currently unable to study the hot gas phase ($T > 10^{5.5}$ K) with x-rays (*Tumlinson et al.*, 2017). Ultraviolet (UV) absorption lines (e.g., Si-IV, C-IV, N-V) can trace gas in the warm CGM ($T \sim 10^{5.5}$ K) if collisionally ionized or the cool CGM ($T \sim 10^4$

K) if photoionized. Fixing the radiation field to a temporally and spatially constant metagalactic background field (e.g., *Faucher-Giguere et al.*, 2009; *Haardt and Madau*, 2012) is a common assumption when performing photoionization modeling to interpret absorption-line spectra (e.g., *Savage and Wakker*, 2009). The same assumption is employed when generating synthetic absorption-line spectra from simulations using tools such as *Trident* (*Hummels et al.*, 2017). This approach ignores the contribution of stars within the host galaxy to the ionizing radiation field in the CGM. This assumption is likely reasonable at large distances from the galaxy due to geometric dilution of the radiation field and absorption of ionizing radiation in the interstellar medium (ISM) and inner CGM, but there must be some distance at which local sources within the galaxy dominate the ionizing radiation field. How this 'transition radius', i.e., the distance at which the ionizing radiation field changes from being local source-dominated to metagalactic background-dominated, varies with galaxy properties has not been constrained in detail.

For present-day Milky Way-mass halos, back-of-the-envelope calculations considering simple geometric dilution of the ionizing radiation field and a fixed molecular cloud escape fraction suggest that the contribution of local sources to the ionizing radiation field equals that of the metagalactic background at $\sim$ 50 kpc at $z = 2.8$ (*Shen et al.*, 2013) and 50-200 kpc at $z \sim 0$ (*Sternberg et al.*, 2002; *Werk et al.*, 2014; *Sanderbeck et al.*, 2018). Both estimates are a significant fraction of the viral radius. However, this question has not been addressed with more realistic galaxy models. To better determine this transition radius, it is necessary to properly model the transfer of stellar ionizing photons from within the host galaxy through a time-varying, multiphase ISM/CGM. Moreover, how this transition radius depends on properties such as mass and redshift has not been thoroughly investigated.

Increasingly more sophisticated cosmological (magneto)hydrodynamic simulations of galaxies, such as the FIRE-2 cosmological simulations (*Hopkins et al.*, 2018), can be

used to address this question more thoroughly. *Fumagalli et al.* (2011) performed ionizing photon radiative transfer in post-processing on cosmological simulations. They find that the host-galaxy stars' radiation field's effect on the neutral gas column density $N_{\rm HI}$ dominates that of the metagalactic background at high column densities $N_{\rm HI} > 10^{21}{\rm cm}^{-2}$, which primarily exists closer to the galaxy. *Ma et al.* (2020) also performed radiative transfer on a set of cosmological simulations. They tracked the ionizing photons emitted by individual star particles and concluded that ionizing photons can have a high escape fraction from the galactic halo via low-column-density channels evacuated by previous feedback. The efficiency of this escape depends on the feedback history, which is a function of halo mass. These studies of the high-redshift universe focus primarily on the ionizing photon escape fraction from the entire galactic halo. The escape fraction as a function of radius out of the disk and through the CGM is less well-studied.

The goal of this project is to determine the relative importance of the local stellar ionizing field compared to the background metagalactic field in the CGM of star-forming galaxies in the mass range $10^{10.5}\,{\rm M}_\odot < M_{\rm halo} < 10^{13}\,{\rm M}_\odot$ and redshift range $0 < z < 3.5$. In this work, we post-process 12 galaxies from the Feedback in Realistic Environments (FIRE) project (*Hopkins et al.*, 2014) using a Monte Carlo radiative transfer (MCRT) code. We determine the radius at which the hydrogen-ionizing radiation field from stars within the host galaxy equals the extragalactic background. We calculate the average transition radius from the MCRT results and compare with a simple geometric dilution model. We also compute the ionizing photon escape fraction at several radii.

2.4 Analytical Toy Model

We first present predictions of a simple analytical toy model for how the transition radius depends on halo mass and redshift. The model is motivated by that presented

in Appendix B of *Sternberg et al.* (2002). The galaxy is treated as a point source emitting ionizing photons at a rate $Q_{\rm gal}$, which is assumed to be proportional to the star formation rate (SFR), as these photons are produced primarily by massive OB stars with age $\lesssim 10$ Myr. We use the scaling $Q_{\rm gal} \sim 1.5 \times 10^{53}$ photons s^{-1} at a SFR value of 1 $\mathrm{M_\odot yr^{-1}}$, based on $Q_{\rm gal}$ computed using STARBURST99 (*Leitherer et al.*, 1999), which is similar to the value for the Milky Way (*Sternberg et al.*, 2002). This model assumes that a fixed fraction, $f_{\rm esc}$, of ionizing photons escape the ISM. We take $f_{\rm esc} = 0.05$ (*Sternberg et al.*, 2002). Assuming no absorption of ionizing photons outside the ISM, the stellar photon flux $J^*_{\rm gal}$ at radial distance r is then

$$J^*_{\rm gal}(r) = \frac{f_{\rm esc} Q_{\rm gal}}{4\pi r^2} \quad [\mathrm{s^{-1}\ cm^{-2}}]. \tag{2.1}$$

Setting the galactic and metagalactic fluxes equal, we find the transition radius, $R_{\rm T}$:

$$R_{\rm T} = 280\ \mathrm{kpc} \sqrt{\left(\frac{f_{\rm esc}}{0.05}\right)\left(\frac{\mathrm{SFR}}{\mathrm{M_\odot\ yr^{-1}}}\right)\left(\frac{J^*_{\rm bkg}}{10^3\ \mathrm{cm^2\ s^{-1}}}\right)^{-1}}. \tag{2.2}$$

We use the metagalactic photon flux $\pi J^*_{\rm bkg}$ from *Faucher-Giguere et al.* (2009). Note that in this toy model, the transition radius scales as the square root of the escape fraction, SFR, and metagalactic background flux, so the predictions are relatively insensitive to the exact values used. To determine how the transition radius depends on halo mass and redshift, we use an empirically motivated $\mathrm{SFR}(M_{\rm vir}, z)$ relation. We use the following stellar mass–halo mass relation from *Behroozi et al.* (2013):

$$\log_{10}\left(\frac{M_*}{\mathrm{M_\odot}}\right) = \alpha\ \log_{10}\left(\frac{M_{\rm vir}}{10^{12}\ \mathrm{M_\odot}}\right) + 11, \tag{2.3}$$

where $\alpha = 2.3$ for $M_{\rm vir} < 10^{12}\,\mathrm{M_\odot}$ and $\alpha = 0.22$ for $M_{\rm vir} > 10^{12}\,\mathrm{M_\odot}$. We also employ

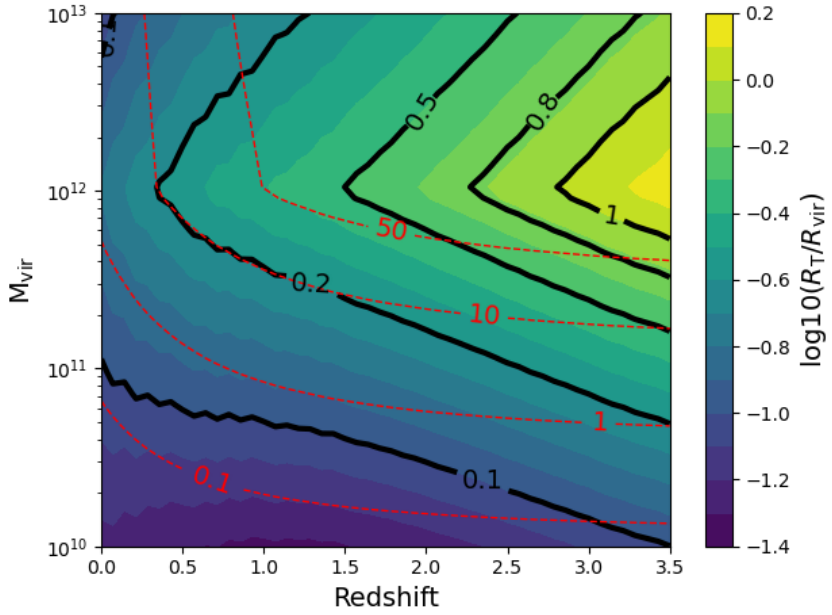

Figure 2.1: Transition radius $R_{\rm T}$ for ionizing radiation with energy 1 Ryd $< E <$ 2 Ryd predicted by the analytic model (using an empirical SFR($M_{\rm vir}, z$) relation and redshift-dependent UV background, assuming 5% of ionizing photons escape the host galaxy, and including geometric dilution). The black lines show contours of constant $R_{\rm T}/R_{\rm vir}$. The red lines show contours of SFR from the empirical relation. At fixed redshift, the threshold radius is maximal at a halo mass of $\sim 10^{12}\,{\rm M}_\odot$ due to the global star formation efficiency being maximal in such halos. At fixed halo mass, the threshold radius increases with redshift. The analytical model suggests that stars within the galaxy have a negligible contribution outside the inner CGM at low redshift, whereas at $z \gtrsim 1.5$ and $M_{\rm vir} \sim 10^{12}\,{\rm M}_\odot$, local stars contribute significantly to the ionizing radiation field in the CGM.

the following SFR-M_* relation from *Speagle et al.* (2014):

$$\begin{aligned} \log\ {\rm SFR} =& (0.84 - 0.026t(z))\log\ M_* \\ & - (6.51 - 0.11t(z)), \end{aligned} \tag{2.4}$$

where $t(z)$ is the current age of the universe in Gyr at a given redshift, SFR has units of ${\rm M}_\odot{\rm yr}^{-1}$, and M_* has units of ${\rm M}_\odot$.Combining the above, we obtain $R_{\rm T}(M_{\rm vir}, z)$.

Figure 2.1 shows how $R_{\rm T}/R_{\rm vir}$ depends on $M_{\rm halo}$ and redshift in the toy model; the colors indicate the $\log_{10}(R_{\rm T}/R_{\rm vir})$ value at a given $(M_{\rm vir}, z)$. The black lines are contours of constant $R_{\rm T}/R_{\rm vir}$ (labeled with their respective linear values), and the

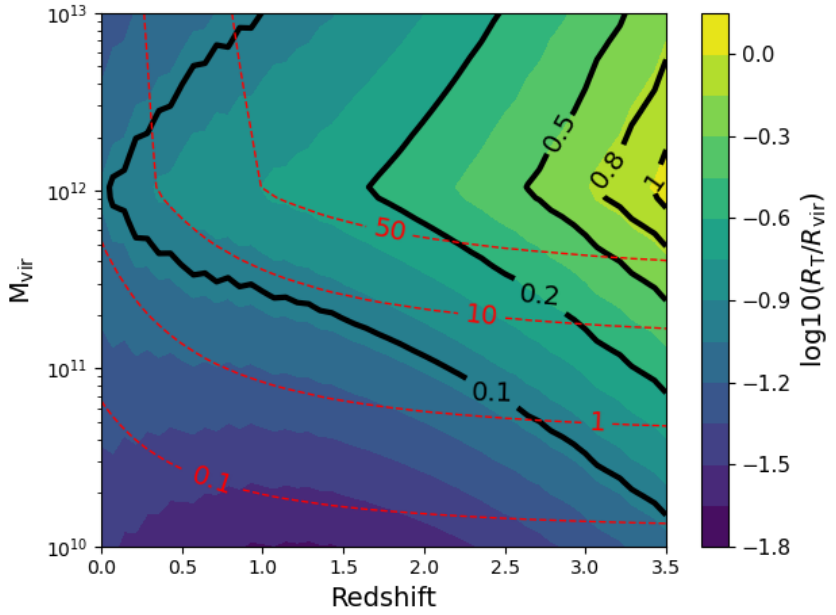

Figure 2.2: Transition radius $R_{\rm T}$ for soft x-rays ($E = 0.1 - 1$ keV) predicted by the analytic model. At fixed halo mass and redshift, the threshold radius is lower for soft x-rays than for photons with energy ~ 1 Ryd. The color scheme represents the same quantities as in Figure 2.1.

red lines are contours of constant SFR from the empirical relation. This figure shows that in the toy model, at a given redshift, the transition radius is maximal for halos of mass $\sim 10^{12}\,{\rm M}_\odot$ because this is the halo mass at which the global star formation efficiency peaks. For halos of this mass, local stars can contribute significantly to the ionizing radiation field deep into the CGM. At $z \lesssim 0.5$, for all halo masses, local stars are subdominant beyond 0.2 $R_{\rm vir}$. However, at higher redshift, the transition radius can exceed 0.2 $R_{\rm vir}$ for halos with $M_{\rm vir} \gtrsim 10^{11}\,{\rm M}_\odot$, meaning that local stars contribute significantly to the ionizing radiation field well into the CGM.

We also estimate $R_{\rm T}$ for soft x-rays, ignoring any active galactic nuclei (AGN). We assume a soft x-ray luminosity (primarily from supernova remnants) of $L_{\rm x} \sim 2.2 \times 10^{39}$ ergs s^{-1} (*Slavin et al.*, 2000; *Sternberg et al.*, 2002) for a Milky Way-like galaxy with SFR $\sim 1\,{\rm M}_\odot\,{\rm yr}^{-1}$ and assume that the soft x-ray luminosity scales linearly with SFR. The metagalactic soft x-ray flux $F_{\rm bkg}$ is taken from *Faucher-Giguere et al.*

(2009). We find

$$R_{\rm T} = 9.1 \text{ kpc} \sqrt{\left(\frac{L_{\rm x}}{10^{39} \text{ ergs s}^{-1}}\right)\left(\frac{\rm SFR}{\rm M_\odot \text{ yr}^{-1}}\right)\left(\frac{F_{\rm bkg}}{10^{-7}\text{ergs cm}^{-2} \text{ s}^{-1}}\right)^{-1}}. \quad (2.5)$$

Figure 2.2 shows the same contour plot as Figure 2.1, except for soft x-rays. More of the parameter space is within a transition radius of 0.2 $R_{\rm vir}$ compared to the plot for photons of energy ~ 1 Ry. For a Milky Way-like galaxy at $z = 0$, the transition radius is $R_{\rm T} \sim 0.1 R_{\rm vir}$. Halos with mass $M_{\rm halo} > 10^{11.5}$ at $z > 2$ can have larger regions in which local stars dominate the soft x-ray background, the transition radius is typically still < 0.5 $R_{\rm vir}$. We note that if an AGN is present, its contribution to the soft x-ray background likely dominates.

2.5 Methods and Data

2.5.1 Simulations

We analyze a set of 12 cosmological zoom-in simulations from the FIRE project[1] that were run using the FIRE-2 code (*Hopkins et al.*, 2018). We chose 4 simulations from each of the 'm11', 'm12', and 'm13' series, corresponding to present-day halo masses of approximately $10^{11}\,\rm M_\odot$, $10^{12}\,\rm M_\odot$, and $10^{13}\,\rm M_\odot$, respectively. The specific sample of simulations studied in this paper include the halos first presented in *Feldmann et al.* (2016), *Anglés-Alcázar et al.* (2017b) and *Hopkins et al.* (2018); see Table 2.1. We analyze the central galaxy within each simulation in the redshift range $0 < z < 3.5$. The selected mass and redshift range is motivated by the regime of parameter space spanned by current and forthcoming observational studies of the CGM. The properties of the simulated galaxies are summarized in Table 2.1.

[1] http://fire.northwestern.edu

Table 2.1: Information from FIRE-2 simulations analyzed in this work. The properties of the central halo within each simulation are listed.

Name	$M_{\rm h}$ [$\rm M_\odot$]	M_* [$\rm M_\odot$]	$m_{\rm b}$ [$\rm M_\odot$]	Ref
m11h	2.07×10^{11}	3.6×10^{9}	7100	*El-Badry et al.* (2018)
m11d	3.23×10^{11}	3.90×10^{9}	7100	*El-Badry et al.* (2018)
m11v	1.40×10^{11}	2.40×10^{9}	7100	*Hopkins et al.* (2018)
m11q	1.63×10^{11}	3.70×10^{8}	7100	*Hopkins et al.* (2018)
m12b	1.43×10^{12}	8.50×10^{10}	7100	*Garrison-Kimmel et al.* (2019)
m12m	1.58×10^{12}	1.10×10^{11}	7100	*Hopkins et al.* (2018)
m12f	1.71×10^{12}	7.90×10^{10}	7100	*Garrison-Kimmel et al.* (2017)
m12i	1.18×10^{12}	6.30×10^{10}	7100	*Wetzel et al.* (2016)
m13A1	3.92×10^{12} $(z = 1)$	2.75×10^{11} $(z = 1)$	33000	*Anglés-Alcázar et al.* (2017b)
m13A2	7.75×10^{12} $(z = 1)$	4.10×10^{11} $(z = 1)$	33000	*Anglés-Alcázar et al.* (2017b)
m13A4	4.54×10^{12} $(z = 1)$	2.34×10^{11} $(z = 1)$	33000	*Anglés-Alcázar et al.* (2017b)
m13A8	1.27×10^{13} $(z = 1)$	5.36×10^{11} $(z = 1)$	33000	*Anglés-Alcázar et al.* (2017b)

The simulations use the code GIZMO (*Hopkins*, 2015)[2], with hydrodynamics solved using the mesh-free Lagrangian Godunov "MFM" method. Both hydrodynamic and gravitational (force-softening) spatial resolution are set in a fully-adaptive Lagrangian manner; mass resolution is fixed. The simulations include cooling and heating from a meta-galactic background and local stellar sources from $T \sim 10 - 10^{10}$ K; star formation in locally self-gravitating, dense, self-shielding molecular, Jeans-unstable gas; and stellar feedback from OB & AGB mass-loss, SNe Ia & II, and multi-wavelength photo-heating and radiation pressure, with inputs taken directly from stellar evolution models. The FIRE physics, source code, and all numerical parameters are *exactly* identical to those in *Hopkins et al.* (2018).

2.5.2 Monte Carlo Radiative Transfer

We perform ionizing photon MCRT in post-processing on the $z < 3.5$ snapshots of the 12 central halos using the code from *Ma et al.* (2020). For each snapshot, we map the gas particles within the virial radius $R_{\rm vir}$ onto an octree grid, first by depositing the particles in a $(2\ R_{\rm vir})^3$ cube and then dividing this parent cell into 8 child cells until the final leaf cells contain no more than 2 particles. The physical properties of each cell are computed using a cubic spline smoothing from the nearest 32 particles.

The full MCRT calculation proceeds as follows (e.g., *Fumagalli et al.*, 2011; *Ma et al.*, 2015; *Smith et al.*, 2019). The rate of hydrogen ionizations of each star as a function of age and metallicity is computed using the Binary Population and Spectral Synthesis (BPASS) model (v2.2.1; *Eldridge et al.*, 2017). In this analysis, we do not include the effects of stellar binaries; however, we show in Appendix 2.10 that this choice does not significantly affect our results. 10^8 hydrogen ionizing photon packets are emitted isotropically from the star particle locations, sampled according to their ionizing photon emissivity. An equal number of photon packets are emitted inward

[2]http://www.tapir.caltech.edu/ phopkins/Site/GIZMO.html

at the domain boundary, representing an isotropic and uniform background radiation field with an intensity given by *Faucher-Giguere et al.* (2009). Each photon packet propagates until it either escapes the domain or is absorbed. Absorption occurs via two channels, by neutral hydrogen with a photoionization cross section from *Verner et al.* (1996) and from dust grains. Dust grains can also scatter the photon packets. We assume that 40% of the metals are locked into dust grains in gas below 10^6 K; gas cells with $T > 10^6$ K are assumed to be dust-free. We assume that the dust has a Small Magellanic Cloud grain-size distribution (*Weingartner and Draine*, 2001a), with a dust opacity of 3×10^5 cm^{2}g^{-1} and a Lyman limit albedo of 0.277. Using the cell gas temperature from the simulation, we calculate the ionization rate in each cell by assuming ionization equilibrium, including temperature-dependent collisional ionization (*Jefferies*, 1968) and recombination rates (*Verner et al.*, 1996). Transport of photon packets is iterated 10 times to reach convergence of the ionization state. The output of the radiative transfer code is an ionization rate $\Gamma_{\rm ion}$ and neutral fraction $n_{\rm HI}$ for each octree cell. For our analysis, we run the MCRT code for 4 different scenarios for each snapshot:

- *MCRT, stellar + background sources* (RT-full): This scenario includes both local stellar and metagalactic background photons. The ionization rate is denoted $\Gamma_{\rm ion}$. This run, with the most realistic ionization state correction, is used to determine the cells affected by ionizing radiation from stars within the host galaxy.

- *MCRT, suppressed stellar + background sources* (RT-supp): In this scenario, the ionizing photon production rates for star particles are suppressed by a factor of 10^{-4} (given the code infrastructure, this is simpler than removing the stellar sources entirely and has essentially the same effect). The ionization rate is denoted $\Gamma_{\rm ion,supp}$. By comparing the ionization state obtained in this scenario with the ionization state from RT-full (i.e., with all sources included), we can

determine if a cell has been affected significantly by ionizing radiation from stars within the host galaxy.

- *Geometric photon dilution only* (RT-geo): This scenario includes only stellar photons (i.e. the metagalactic background is ignored). The ionization state of all gas is set to be completely ionized, so there is no absorption of photons. The decrease in the ionization rate with radius is purely due to geometric dilution. The ionization rate obtained from these calculations is denoted $\Gamma_{\rm ion,geo}$. This run is useful in order to compare with other runs that do include photon absorption/scattering processes, allowing us to calculate the photon escape fraction. The motivation for performing such runs rather than simply doing a trivial analytic calculation is that it enables us to determine the exact ionizing photon production rate yielded by BPASS given the properties (i.e., ages and metallicities) of the star particles rather than assuming a constant ionizing photon production rate per unit SFR (as we do in the toy model).

- *Stellar sources-only, after MCRT* (post-RT-stellar): This run includes only stellar photons, similar to the geometric photon dilution case, except the gas ionization state is fixed to be that obtained in the full MCRT run (i.e., including both local stellar sources and the metagalactic background). The ionization rate is denoted $\Gamma_{\rm ion,post-RT}$. By comparing the radial profile of this ionization rate with that of RT-geo, we can estimate the ionizing photon escape fraction.

2.6 Results

Before examining the radiative transfer calculations, it is useful to compare the SFR between the simulations and the analytic estimates from Section 2.4 since the SFR is the key parameter in the toy model. Figure 2.3 shows filled contours of the simulated galaxies' median SFR value in log space. The empirical relation SFR

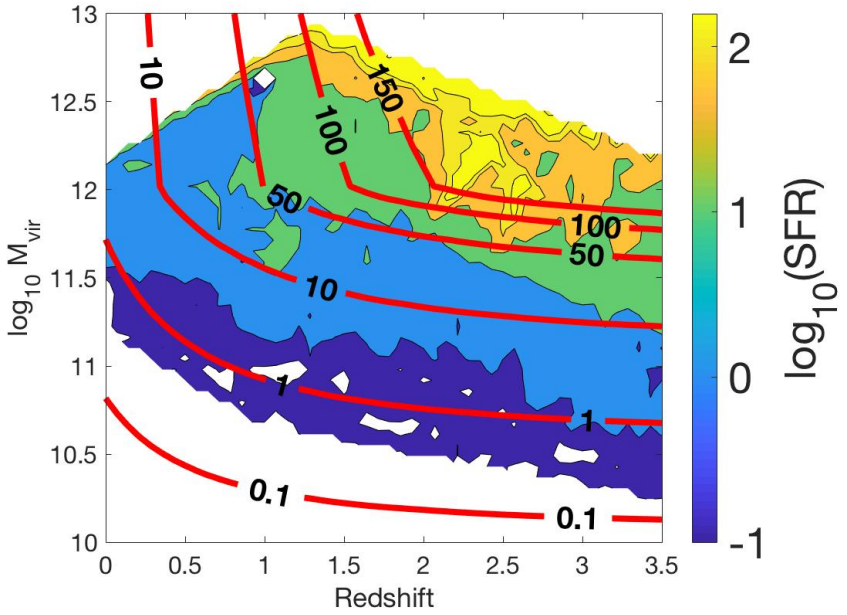

Figure 2.3: Comparison of mean SFR for the simulated galaxies and SFR from the empirical relation given in Section 2.4 in the $(M_{\rm vir}, z)$ parameter space. The filled contours show the logarithmic values of the simulations' SFR values in units of $\mathrm{M}_{\odot}\mathrm{yr}^{-1}$. The red contours show the linear SFR from the empirical relation. The simulated galaxies' and empirical SFR values have similar trends across the parameters space, but the simulations' SFRs are generally lower by a factor of ~ 10, and a factor of a few at $M_{\rm vir} \sim 10^{12.5}\,\mathrm{M}_{\odot}$.

values are overplotted as lines for the same range as Figure 2.1. The simulations and empirical relation show similar trends across the parameter space. The empirical relation is consistently greater than the median SFR of the simulated galaxies at a given stellar mass and redshift, up to 5 times larger at $\log_{10} M_{\rm vir} < 10^{11.5}$. We would thus expect smaller transition radii in the simulations compared to the toy model, though because $R_{\rm T}$ is proportional to the square root of the SFR, the SFR difference should result in a factor of at most ~ 2 difference in $R_{\rm T}$.

The output of the MCRT code is an ionization rate $\Gamma_{\rm ion}$ and neutral gas fraction $n_{\rm HI}$ in each of the cells within the central halo in a particular simulation. In order to determine the radius of influence from stellar radiation, we compare the RT-full and RT-supp versions of the radiative transfer calculations described in Section 2.5.2. The result of the RT-supp run is the ionization $\Gamma_{\rm ion,supp}$ and neutral fraction $n_{\rm HI,supp}$ that result from the metagalactic background alone (since the stellar ionizing photon rates are suppressed to negligible values). By comparing the two different ionization rates, we can determine which cells are influenced by ionizing photons from stars within the host galaxy.

We calculate the value of $R_{\rm T}$, the radius at which the stellar radiation becomes sub-dominant to the metagalactic field, by looking at the radial distribution of cells that satisfy the criterion

$$\left(\frac{\Gamma_{\rm ion,supp}}{\Gamma_{\rm ion}}\right) < 0.5, \tag{2.6}$$

i.e., the cells in which the ionization rate is reduced below a factor of two when host galaxy stellar sources are suppressed. We found similar results with ratio values of 0.1 and 0.2. There are several possible definitions of $R_{\rm T}$, and we chose $R_{\rm T}$ to be the median of the distribution of cells satisfying Eq. 2.6. We choose the median instead of the mean in order for the calculation to be less affected by incoming merging galaxies, which contain their own stellar sources. We compared the results of choosing the median, mean, and peak of the cell radius distribution and found that the results

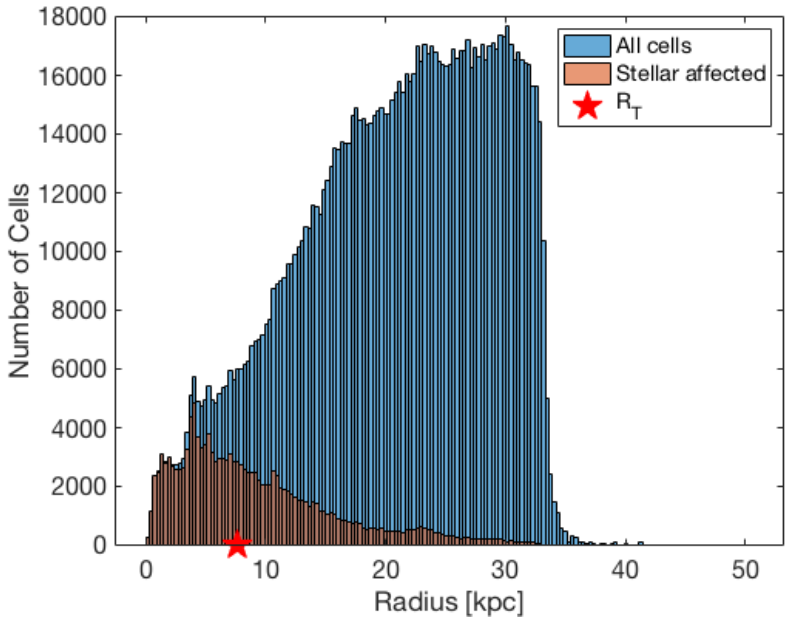

Figure 2.4: Demonstration of how the transition radius is calculated for the 'm12b' halo at redshift 3.5. The histograms show the distribution of radial distance from the galaxy center for cells in which local stars dominate the ionizing photon flux (red) and all cells (blue). The transition radius $R_{\rm T}$ is defined as the median radial distance of cells for which local stars dominate the ionizing radiation field and is denoted by the red star.

were similar. As an example, we show the radial distributions of all cells and cells affected by stellar radiation for the $z = 3.5$ snapshot of the 'm12b' simulation in Figure 2.4. As expected, the distribution of cells affected by stellar radiation peaks at lower radii compared to the distribution of all cells. The median radius value of this distribution is shown with a star marker; this is the $R_{\rm T}$ value for this snapshot.

We estimate the escape fraction at a given radius by comparing photoionization rate radial profiles from two of the MCRT runs with only stellar photons, RT-geo and post-RT-stellar, with ionization rates $\Gamma_{\rm ion,geo}$ and $\Gamma_{\rm ion,post-RT}$ respectively. The escape fraction at a given radius r is equal to the ratio of the number of ionizing photons at a given radius, $N_{\rm ion}(r)$, to the number of photons emitted by stellar sources, N_*. The ionization rate is related to the ionizing photon rate as follows: $N_{\rm ion}/r^2 \times$ Attenuation$(r) \propto \Gamma_{\rm ion}(r)$, where the no-attenuation case recovers the r^{-2} decay in the

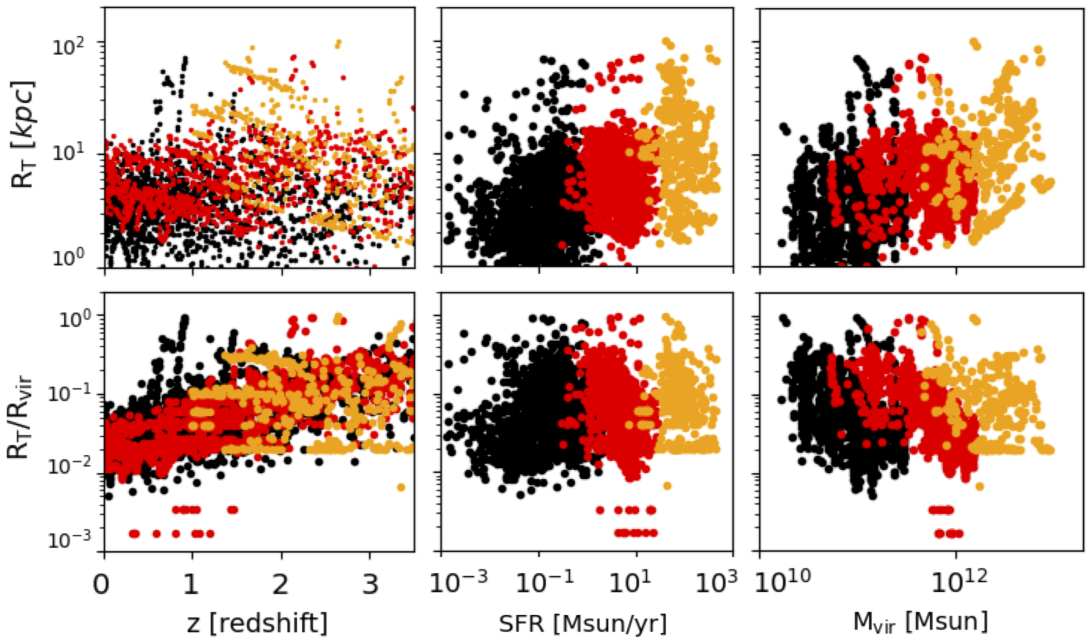

Figure 2.5: Transition radius in kpc (*top row*) and as a fraction of the virial radius (*bottom row*) versus redshift (*left column*), SFR (*middle column*), and halo mass (*right column*). The points are colored according to $z = 0$ halo mass: $\sim 10^{11}\,\mathrm{M}_\odot$ in *black*, $\sim 10^{12}\,\mathrm{M}_\odot$ in red, and $\sim 10^{13}\,\mathrm{M}_\odot$ in orange. The absolute value of R_T is slightly increasing with redshift and increases with both SFR and halo mass; as a fraction of the virial radius, $R_\mathrm{T}/R_\mathrm{vir}$ increases with redshift and exhibits no strong trend with SFR or halo mass. At fixed redshift, SFR, or halo mass, the simulations exhibit a broad range of transition radii, ranging from $\sim 0.01 - 1\ R_\mathrm{vir}$.

photon number density. The escape fraction as a function of radius within a given snapshot is equal to the ratio of the ionization rate expected without attenuation and the rate actually present,

$$f_\mathrm{esc} \sim \frac{\Gamma_\mathrm{ion,geo}(r)}{\Gamma_\mathrm{ion,post-RT}(r)}. \tag{2.7}$$

In Figure 2.5, we summarize the results of the MCRT calculations of the transition radius R_T for all 12 of the simulations (grouped into present-day halo mass bins of $\sim 10^{11}$, 10^{12}, and 10^{13} $\mathrm{M}_\odot$) between $z = 0$ and $z = 3.5$, except for the 'm13' halos, which stop at $z = 1$. Three parameters that influence R_T are the metagalactic field ionizing rate $\Gamma_\mathrm{ion,bkg}$ (a stronger background reaches closer to the galaxy), halo

mass $M_{\rm vir}$ (determines the value of $R_{\rm vir}$ and bulk galaxy properties), and the SFR (determines the ionizing photon production rate to zeroth order, as there is some 'second-order' dependence on the star formation history over the past $\sim 10-20$ Myr). In order to aid our analysis, we note that the metagalactic field strength increases (e.g., *Faucher-Giguere et al.*, 2009), the halo mass decreases (*Behroozi et al.*, 2013), and SFR increases with increasing z (*Speagle et al.*, 2014).

In general, the physical value $R_{\rm T}$ tends to be greater for increasing redshift and SFR, although there are some points with much larger radii within each galaxy halo mass bin. For example, the average transition radius for 'm11' galaxies is $R_{\rm T} \sim 5$ kpc, but values up to 50 kpc can briefly occur. All three of the galaxy mass types of 'm11', 'm12', and 'm13' span a large range of $R_{\rm T}$, but the high-mass groups tend to have more snapshots with higher $R_{\rm T}$. This trend makes sense when looking at the clear separation of mass type with SFR. Higher SFR will lead to more ionizing photons and larger $R_{\rm T}$. Within each mass type, a larger $M_{\rm halo}$ very weakly (and with large scatter) tends to have larger $R_{\rm T}$. Looking at the redshift trend, the mean $R_{\rm T}$ value is essentially constant with z, indicating that while the SFR increases with z, the corresponding increase in the strength of background ionizing radiation is enough to cancel out the increase in $R_{\rm T}$ that would otherwise result.

The transition radius relative to $R_{\rm vir}$ shows trends with SFR and mass type similar to but less pronounced than the ones described above. On the other hand, a trend of decreasing transition radius with redshift becomes clearer, with much less scatter. Also, the trend with halo mass reverses to increasing $R_{\rm T}$ with decreasing $M_{\rm halo}$. This demonstrates that relative to the halo, the average SFR change with redshift exceeds that of the metagalactic background, resulting in higher $R_{\rm T}/R_{\rm vir}$ for earlier universe galaxies. Generally, the halos have values clustered around $R_{\rm T} \sim 0.1$ or below.

We also produce a figure similar to Figure 2.1, which estimates the transition radius assuming purely geometric dilution of the stellar radiation field. Figure 2.6

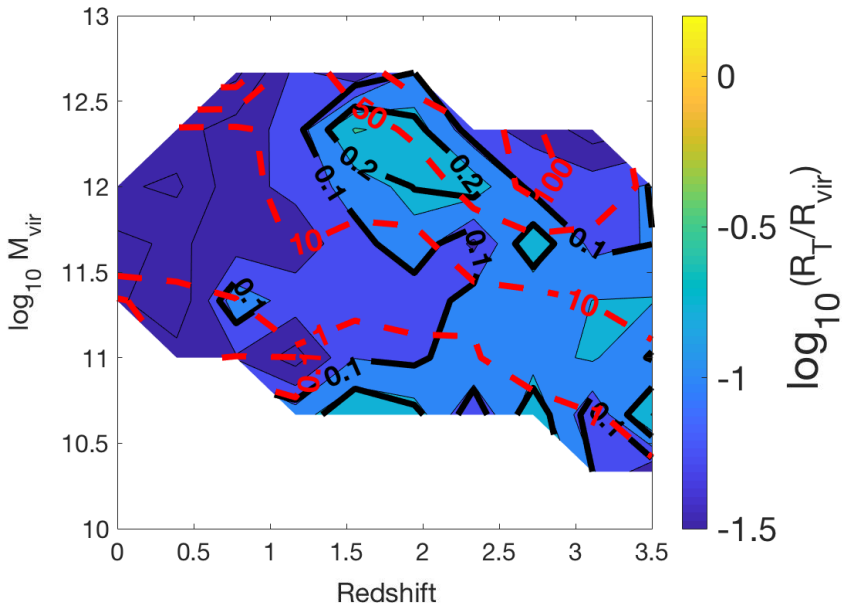

Figure 2.6: Median transition radius $R_{\rm T}$ relative to $R_{\rm vir}$ obtained from the MCRT calculations for ionizing UV radiation with energy 1 Ryd $< E <$ 2 Ryd as a function of halo mass and redshift; compare to the results for the analytic model shown in Figure 2.1. The black lines are contours of constant $R_{\rm T}/R_{\rm vir}$. The red dashed lines denote data SFR contours shown in Figure 2.3. The median transition radii for the simulated galaxies yielded by the MCRT calculations are typically less than the values predicted by the analytic model, partly because of the simulations typically having lower SFRs than the empirical relation. $R_{\rm T}/R_{\rm vir}$ is maximal for $\sim 10^{12}\,{\rm M}_\odot$ halos at $z \sim 2$. Nowhere in the parameter space considered does the typical transition radius exceed $\sim 0.3\ R_{\rm vir}$.

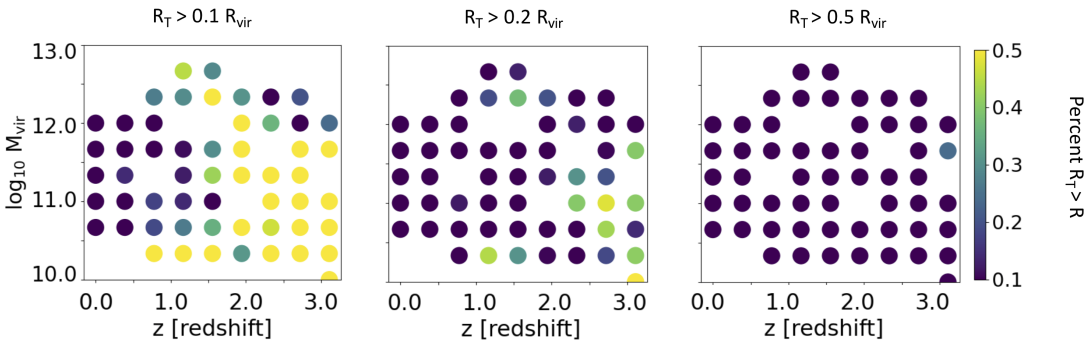

Figure 2.7: Fraction of snapshots in halo mass $M_{\rm vir}$ and redshift z bins that have $R_{\rm T}$ greater than 0.1 $R_{\rm vir}$ (*left*), 0.2 $R_{\rm vir}$ (*middle*), and 0.5 $R_{\rm vir}$ (*right*). At $z \gtrsim 1.5$, most snapshots have transition radii that are $\sim 0.1 - 0.2$ $R_{\rm vir}$. Across the full halo mass and redshift ranges considered $\lesssim 15$ per cent of halos have transition radii greater than 0.5 $R_{\rm vir}$. These results indicate that in the FIRE-2 simulations considered, the contribution of local stars to the ionizing radiation field is subdominant outside the very inner CGM.

shows that by including not only geometric dilution but also the three-dimensional spatial and phase structure of the CGM, the mean values of $R_{\rm T}$ are greatly suppressed compared to geometric dilution only. The transition radius is generally at or below 0.1 $R_{\rm vir}$ for halos at redshift $z < 1$. The transition radius increases at higher redshift. The greatest increase is seen for $M_{\rm halo} \sim 10^{12}$ at $z = 2$ (i.e. 'm13' halos), which have $R_{\rm T} \gtrsim 0.2$ $R_{\rm vir}$. Lower-mass halos also have an increased value of $R_{\rm T}$, greater than 0.1 $R_{\rm vir}$, though typically not > 0.2 $R_{\rm vir}$. Nowhere in the parameter space is there an average transition value greater than 0.4 $R_{\rm vir}$. We note that these contour plots represent the average values of $R_{\rm T}$ in a particular (z, $M_{\rm halo}$) bin, and as Figure 2.5 shows, some snapshots do have larger transition radius values.

In Figure 2.7 we plot the fraction of snapshots within the ($M_{\rm vir}$, z) bins (similar to Figure 2.1 and 2.6) that have $R_{\rm T}$ greater than 0.1, 0.2 or 0.5 $R_{\rm vir}$. The color axis is set to a maximum of 0.5 in order to clearly identify regions where the majority of halos have an $R_{\rm T}$ value greater than the specified fraction of the virial radius. In Figure 2.8, we plot the escape fraction $f_{\rm esc}$ at a given radius. We see that the majority of the $z < 1.5$ galaxies of all masses do not have significant stellar radiation influence

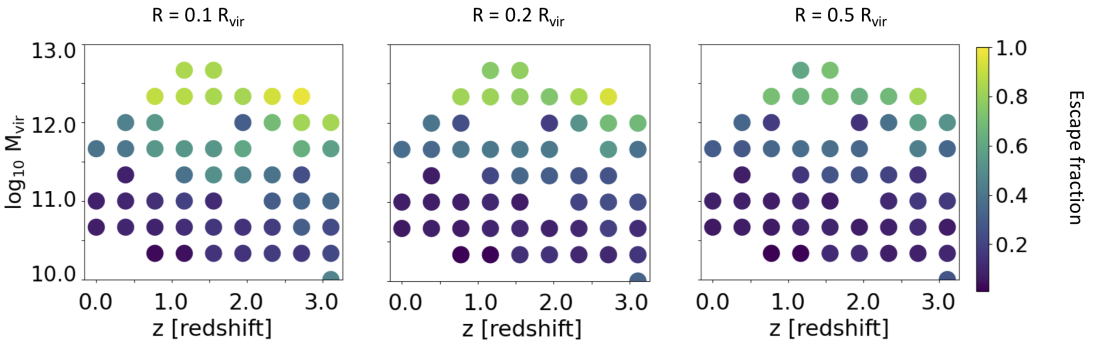

Figure 2.8: Mean escape fraction $f_{\rm esc}$ at a particular radius R in $M_{\rm vir}$ and redshift z bins: 0.1 $R_{\rm vir}$ (*left*), 0.2 $R_{\rm vir}$ (*middle*), and 0.5 $R_{\rm vir}$ (*right*). At fixed redshift and for all radii considered, the escape fraction increases from $\lesssim 20$ per cent at $M_{\rm vir} \sim 10^{10}\,{\rm M}_{\odot}$ to ~ 80 per cent or higher in the most-massive halos.

into the CGM ($R \sim 0.1 R_{\rm vir}$). For $z > 1.5$, most of the halos have a stellar radiation influence extending into the CGM, despite the escape fraction at this radius being low for the low-mass halos. Further into the CGM, at $R \sim 0.2\ R_{\rm vir}$, most of the domain has a majority halos with $R_{\rm T}$ less than that radius. Only lower-mass halos ($M_h \sim 10^{10.5}\ {\rm M}_{\odot}$) at $z \gtrsim 3$ have some areas where $R_{\rm T}$ is larger. At this radius, the high-halo-mass end of the plot is primarily dominated by the background radiation field. $f_{\rm esc}$ remains high, generally greater than 0.5. For $R \sim 0.5 R_{\rm vir}$, all of the halos are primarily dominated by background radiation field, with less than 10 percent of halos within any bin having a large $R_{\rm T}$. The escape fraction for the highest-mass halos remains relatively high at ~ 0.5.

2.7 Discussion

2.7.1 Explanations for behavior

The transition radius $R_{\rm T}$ depends on two key factors in the analytical analysis presented in Section 2.4, the SFR (proxy for injection of ionizing photons) and the escape fraction $f_{\rm esc}$. The attenuation factor of the metagalactic background field must also be taken into account, as closer to the galaxy the background field could begin to

experience significant attenuation. In a more realistic analysis, $f_{\rm esc}$ is a complicated three-dimensional quantity. If we ignore the spatial coordinates, we can make the approximation that $f_{\rm esc}$ depends on the average porosity and neutral density of the medium (i.e. how clumpy and how dense the medium is) (e.g., *Clarke and Oey*, 2002).

The average snapshot SFR is consistently smaller than that of the analytical model in many places of the $(M_{\rm halo}, z)$ parameter space, so at a fixed $f_{\rm esc}$ we would expect a lower value of $R_{\rm T}$ in the simulation data. Comparing Figures 2.1 and 2.6, we see that this suppression is indeed the case. For example, at $z < 1$ the SFR is the most different between data and the model. The halos we considered have $R_{\rm T} << 0.1\ R_{\rm vir}$, while the analytic model predicted $0.1 - 0.2\ R_{\rm vir}$, a difference in excess of a factor of 10. Part of this difference can be attributed to the lower SFR of the simulations. In contrast, the fact that the data contours of $R_{\rm T}$ do not follow the contours of SFR closely suggests additional complexities. Although the square root of the difference of SFR values, which is the scaling for $R_{\rm T}$, is at most $\sim \sqrt{5-10} \sim (2-3)$, and does not explain the factor of 10 difference in $R_{\rm T}$ values. For $M_{\rm halo} > 10^{12}\ M_{\odot}$ and redshift $z \sim 1.5 - 2.5$, the differences in $\sqrt{SFR}$ of $\sim 2 - 3$ are consistent with differences in $R_{\rm T}$ of a similar factor (differences between $R_{\rm T}$ values of 0.5 and 0.2). Although, the gap between the two values widens at $z > 3.0$ as the data transition radius does not exceed $0.2\ R_{\rm vir}$, while the model values continue increasing with increasing redshift. Interestingly, the lower mass $M_{\rm halo} < 10^{11.5}\ {\rm M}_{\odot}$ and redshift $z > 1.5$ region of the parameter space has similar values of transition radii between the model and simulated data, even while retaining a difference in SFR.

These findings indicate the effect of at least an additional parameter, such as the escape fraction, which is estimated in Figure 2.8. A decrease in the average $f_{\rm esc}$ below the value of 0.05 assumed in the analytic model would further suppress transition radius in the data, while an increase would have the opposite effect on the transition radius with the same square root scaling. Indeed, for low mass $M_{\rm halo} > 10^{11}\ M_{\odot}$,

lower redshift $z < 1.5$ halos, the escape fraction is on the order of 0.05 or lower. The similar values of $R_{\rm T}$, with different SFR values for lower mass $M_{\rm halo} < 10^{11.5}$ $M_\odot$ and redshift $z > 1.5$ also can also justified with a different escape fraction than 0.05. Since the values of $f_{\rm esc}$ are in excess of 0.1 at $R = 0.1$ $R_{\rm vir}$, a smaller SFR in the data can result in a larger transition radius than expected with a fixed $f_{\rm esc} = 0.05$. The explanation, however, does not work for the higher mass $M_{\rm halo} > 10^{11.5}$ $M_\odot$ halos, where the estimated escape fractions are consistently quite high, reaching 0.5 or above (factor of 10 larger than the model), even at $R \sim 0.5$ $R_{\rm vir}$ and independent of redshift. This high escape fraction implies a consistent increase in the transition radius of the high mass halos of at least a factor of 3 in the data at all redshifts, which is not in agreement with the values seen in the contour plot. In fact, for $z > 2.5$, there is a clear *decrease* in the transition radius in the simulation snapshots.

We can also examine the role of the metagalactic field. The evolution of the background field is accounted for in both the analytic and simulation calculations. The analytic model does not account for the attenuation of the metagalctic field closer the galaxy. An attenuated metagalatic field would depress R_T in the data relative to the analytic model, so our analytic estimates with an unattenuated metagalactic field can be thought of as an upper limit to the transition radius. This finding can help explain some of the discrepancies above, but is not easy to untangle it from the other effects. This parameter is challenging to describe because it is coupled to the state of the galaxy itself and outer CGM: the properties of the galaxy/inner CGM radially outward determine the escape of the stellar photons, and the properties of the outer CGM radially inward determine the attenuation of the metagalatic field.

Overall, we see that any analysis with a set of parameters, such as the escape fraction, does not adequately provide a clear explanation for the differences and similarities in Figures 2.4 and 2.6 across the entire parameter space we chose. Further investigation beyond our radial analysis of the influence of stellar radiation is needed

in order to untangle the exact contribution of each parameter discussed throughout the halo mass and redshift parameter space.

2.7.2 Relevance for Analysis of Simulations and Observations

Many analyses of CGM diagnostics suffer from degeneracies in the predicted underlying plasma properties. As mentioned in the introduction, purely collisional ionization equilibrium and complete photoionization equilibrium are two contrasting models that predict greatly different plasma properties of the CGM from a particular plasma diagnostic, obfuscating our understanding of the physics processes occurring (e.g., analysis of specific ions in works such as *Fox et al.*, 2005; *Werk et al.*, 2019). Even purely collisional ionization models could be modified by the presence of ionizing radiation, even if the radiation is not dominant (*Tumlinson et al.*, 2017). The metagalactic field is simpler to include in analyses compared to stellar sources because the metagalactic spectrum is more precisely constrained. The stellar spectrum can produce much more uncertainty in models. Estimating where the stellar spectrum is likely to be sub-dominant to the metagalactic field greatly simplifies the suite of models to be considered for a particular plasma diagnostic.

Figure 2.7 provides a guide for the galaxy parameter space where stellar radiation is likely to be important. It shows the regions in the ($M_{\rm halo}$, z) parameter space where stellar ionizing radiation effects (near hydrogen ionizing values) are likely to be at least as important as the background field. For $z < 1$, very few of the galaxy data points in each bin had stellar radiation that extended beyond 0.1 $R_{\rm vir}$ into the CGM, while at higher redshift, most of the galaxies extended beyond that radius. On the other hand, no bins in the entire parameter space showed significant data points that dominated beyond 0.5 $R_{\rm vir}$. The radial shell between 0.1 and 0.2 $R_{\rm vir}$ is where many $z > 1$ galaxies showed the transition between stellar to background dominated radiation field. This is also seen in the structure of the filled contour plot of $R_{\rm T}$ in

Figure 2.6, where there are fluctuations and islands in the contours of $R_{\rm T}$ between 0.1 and 0.2 $R_{\rm vir}$.

The radial extent of stellar effects on a plasma diagnostic varies with the particular ion in question. Since our MCRT analysis does not track the exact energy of the ionizing photons and the photon number decreases energy, we effectively are assuming that the photons are all emitted near the hydrogen ionizing energy of 13.6 eV. Our results are most relevant for the ions whose ionization potentials are near this energy. These ions are denoted 'low' ions by *Tumlinson et al.* (2017), as they have ionization energies of < 40 eV. Low ions include CII, CIII, SiII, SiIII, NII, and NIII. Our results are increasingly less relevant for ions at higher ionization energies both because of our single energy approximation and changing photon sources. First, stars emit much less photons at higher energies. Supernovae remnants (*Sternberg et al.*, 2002) and x-ray binaries (e.g., *Points et al.*, 2001), which dominate x-ray photon emission, are not included in our analyses. Second, 'high' ions with ionization potentials beyond 100 eV (0.1 keV) are more accurately described by our analytical estimate for soft x-ray $R_{\rm T}$ in Figure 2.2. For 'intermediate' ions with ionization energies between 40 and 100 eV, the value of $R_{\rm T}$ is probably a transition between the two limits.

Statistical analyses are increasingly more important as observational (e.g., James Web Space Telescope) and computational (e.g., IllustrisTNG, *Pillepich et al.* (2018)) data sets continue to improve, resulting in large galaxy data sets containing a wealth of information. It might be computationally impractical (or outright infeasible) to devote resources to accurate modeling of stellar radiation when analyzing a large galaxy dataset. Our results help support the choice to avoid more expensive modeling. For example, the tool Trident provides a simple, efficient method producing numerous different synthetic absorption sightlines for simulated galaxies, but does not include stellar ionizing sources. Our results denote a large part of the parameter space where Trident analyses are likely correct to use.

	$R/R_{\rm vir}$		
	0.1	0.2	0.5
a	0.124 (0.118, 0.13)	0.0865 (0.0813, 0.0916)	0.0617 (0.0566, 0.0668)
b	0.384 (0.375, 0.392)	0.353 (0.345, 0.361)	0.298 (0.290, 0.306)
c	-4.229 (-4.325, -4.132)	-3.889 (-3.985, 3.792)	-3.269 (-3.365, -3.174)

Table 2.2: Coefficients a,b,and c from Eq. 2.8, with each column representing (left to right) 0.1, 0.2, and 0.5 $R_{\rm vir}$ respectively. The 95 percent confidence intervals are shown in parentheses. Note: Values of $f_{\rm esc}$ should have a floor value, as the fit can produce negative values near $z = 0$.

Additionally, estimating a radially dependent ionizing photon escape fraction, while not the focus of this work, is a potentially useful result. In order to aid any statistical analyses using a photon escape fraction, we provide a simple linear fit to the data used in Figure 2.8. The data for $f_{\rm esc}$ had a relatively large scatter of $\sigma_{\rm esc} \sim 0.2$ consistently across the parameter space, which is not shown in Figure 2.8.

The fit is as follows

$$f_{\rm esc} = az + b\log_{10}M_{\rm halo} + c, \tag{2.8}$$

with the parameters a,b, and c noted in Table 2.2, including the 95 percent confidence intervals. With this fit, one can assign an escape fraction at a radius of interest to a galaxy of particular mass $M_{\rm halo}$ and redshift z by drawing from the distribution defined here. Alternatively, because the data has a consistent scatter of ~ 0.2, one can calculate the mean $f_{\rm esc}$ value from the equation and assume a standard deviation of 0.2, and randomly sample to assign the actual $f_{\rm esc}$. This large scatter is to be expected, as the escape of ionizing photons is facilitated by low column density channels formed by the three-dimensional, time-dependent, nonlinear feedback processes that constant structure the galactic medium. An appropriate floor for $f_{\rm esc}$ should be chosen, as the fit can produce negative values near $z = 0$, and of course, the data standard deviation of ~ 0.2 can be larger than the calculated $f_{\rm esc}$ from the equation.

2.7.3 Caveats and Further Work

1. Our analysis determines the dominance of stellar versus metagalactic background sources of ionzing photons based on the integrated total ionization rate. We do not consider the spectral slope of the radiation field, which is important in determining the effects of the radiation field on plasma diagnostics. We expect the the integrated ionization rate of the radiation field to be a good proxy for the relative influence of the stellar field, since if it is not dominant, it will not influence the overall spectral shape of the radiation field.

2. We do not consider non-stellar sources of ionizing photons, such as supernova remnants, x-ray binaries, or AGN. These sources are especially relevant at energies higher than 13.6 eV. Further analysis is required in order to properly explore the additional effects of these sources. The effect of AGN in particular introduces another temporally varying ionizing photon source that can effect the circumgalactic medium (i.e. *Segers et al.*, 2017; *Oppenheimer et al.*, 2018).

3. We used a selection of cosmological galaxy simulation results from the FIRE2 suite of simulations, containing one of the most realistic set of feedback models available. Of course, computational models of galaxies continue to be improved in response to higher computational power/algorithmic efficiency (e.g., increased physical resolution) and new research/observational constraints. In particular, the role of cosmic rays in shaping galaxy properties (e.g., *Hopkins et al.*, 2020, 2021b) and influencing plasma diagnostics (*Ji et al.*, 2020; *Holguin et al.*, 2022a) is still unclear. It would be interesting to complete the same MCRT analysis on additional simulations, such as those with cosmic rays (*Chan et al.*, 2019; *Hopkins et al.*, 2020) and those using the updated FIRE3 (*Hopkins et al.*, 2022b) model.

2.8 Conclusions

We performed MCRT on 12 cosmological zoom-in simulations from the FIRE project in order to determine the radial extent to which photons emitted by stars within the host galaxy dominate the hydrogen-ionizing radiation field within the CGM. We selected a set of simulations with present-day halo masses of $10^{11}, 10^{12}$, and 10^{13} $M_\odot$ and considered the redshift range $0 < z < 3.5$. We also compared the numerical results with the predictions of an analytic toy model that assumes a fixed 5 per cent of ionizing photons escape the ISM, employs an empirical SFR($M_{\rm vir}$,z) relation, and treats the radiation as being emitted by a point source and undergoing r^{-2} geometric dilution. Our main conclusions are the following:

1. The average transition radius $R_{\rm T}$, i.e. the radius at which the contribution from stars within the galaxy equals the metagalactic background, is typically $\lesssim 0.1 R_{\rm vir}$ at $z < 1.5$. At $z > 1.5$, the transition radius is a greater fraction of the virial radius. The transition radius is maximal for halos with mass $\sim 10^{12}\,M_\odot$ due to the global star formation efficiency being maximal in such halos. The average value of $R_{\rm T}$ never exceeds 0.4 $R_{\rm vir}$ in the parameter space considered. Our results suggest that for 'typical' galaxies, it is reasonable to neglect local sources when performing photoionization modeling of gas external to the inner CGM.

2. We also find that although the mean transition radius is roughly 0.1 $R_{\rm vir}$, there are periods, typically during and shortly after bursts of star formation, in which the transition radius is a more significant fraction of $R_{\rm vir}$. For $z > 1.5$, the majority of individual snapshots have $R_{\rm T}$ between 0.1 and 0.2 $R_{\rm vir}$; a sizable fraction of halos at $z > 2.5$ have $R_{\rm T} \gtrsim 0.2$ $R_{\rm vir}$. No area in the parameter space had greater than 10 per cent of halos with $R_{\rm T}$ greater than 0.5 $R_{\rm vir}$.

3. The average transition radius $R_{\rm T}$ in the simulated halos is smaller than the

value predicted by the toy model, in part because the SFRs of the simulated galaxies are less (factors of $\sim 2-5$) than the empirical SFR($M_{\rm vir}$,z) relation used.

4. Our calculations of the ionizing photon escape fraction through the CGM indicate a high escape fraction (> 0.5) for more massive $M_{\rm halo} > 10^{12}\,{\rm M}_\odot$ halos independent of redshift.

2.9 Hydrodynamic Simulation Resolution

The underlying resolution of a galaxy simulation can have an effect on both the resulting galaxy properties (e.g., *Weinberg et al.*, 1997; *Bourne et al.*, 2015) and radiative transfer post-processing (*Ma et al.*, 2020). We examine the effect of simulation resolution on results. Figure 2.9 compares the transition radius and SFR of the 'm11q' galaxy-type simulations at '7100' and '880' peak mass resolutions. The exact SFR profile is different between the simulations, but the mean values are relatively consistent. The profiles of $R_{\rm T}$ have similar values between the different resolutions. The higher resolution version has a lot more variability within $z < 1$, but the mean value roughly matches the lower resolution result. Overall, given the fact that resolution will cause divergence in simulation properties, the transition radius results are comparable.

2.10 Single vs. Binary Stellar Sources

In our work, we only considered single star ionizing photon models in MCRT analysis. Stellar binary source models extend the length of time that significant ionizing photon production occurs from a stellar population due mass transfer between stars (*Eldridge et al.*, 2017). In Figure 2.10, we examine the effects of single vs. binary stellar models on the transition radius at a fixed underlying simulation. The SFR

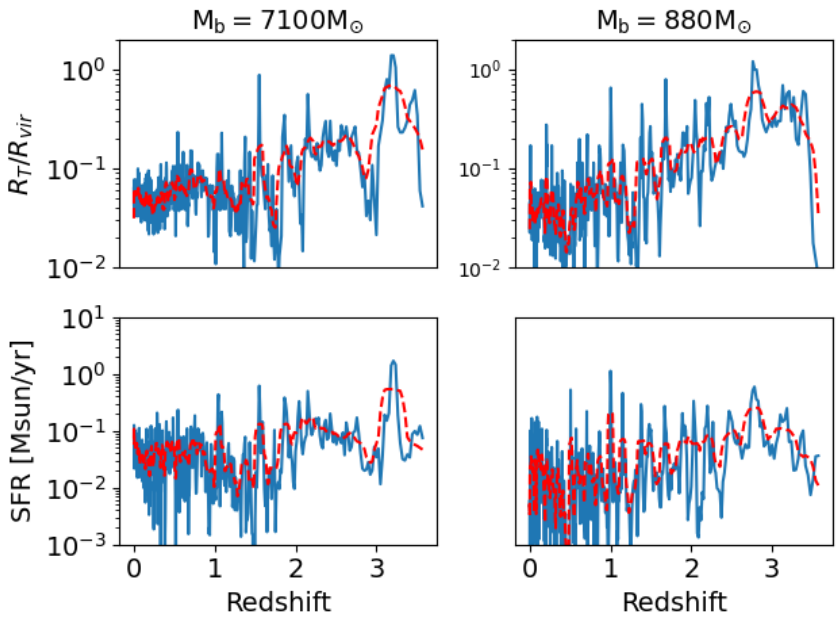

Figure 2.9: Comparison (top: relative transition radius $R_{\rm T}/R_{\rm vir}$, bottom: SFR) of results from two identical galaxy simulation setups at different resolutions. A smoothed version of the data is shown as a red, dashed line.

rate is the same in both examples as the MCRT is done in post-processing. The figure shows that including binary models smooths out some of the variability in the transition radius profile, but the overall mean values are quite similar. The decrease in variability could even reduce number of data points with transition radii larger than a given value, which is plotted in Figure 2.7.

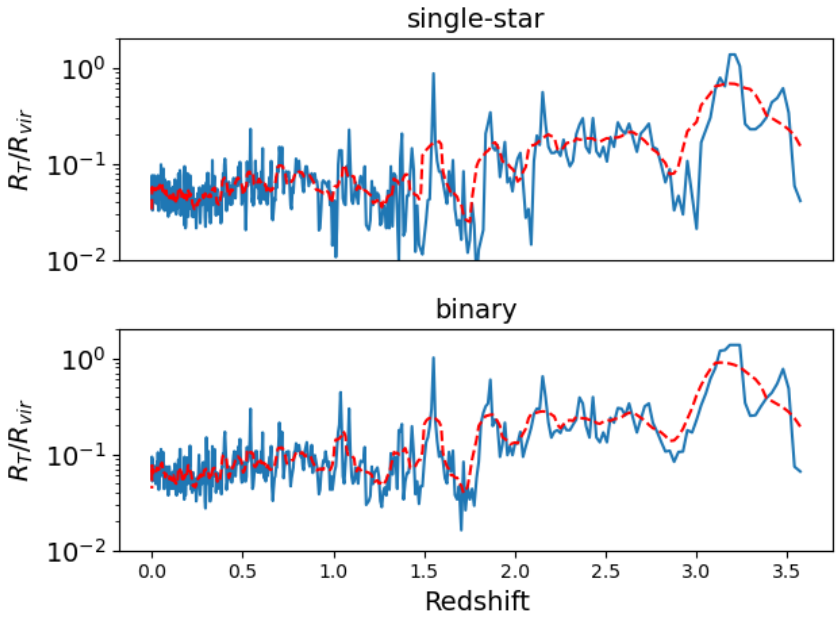

Figure 2.10: Comparison (top: relative transition radius $R_{\rm T}/R_{\rm vir}$, bottom: SFR) of results from the 'm11q7100' simulation analyzed with MCRT assuming only single stellar ionizing photon sources and with single and binary stellar sources included. A smoothed version of the data is shown as a red, dashed line.

CHAPTER III

Role of Cosmic-ray Streaming and Turbulent Damping in Driving Galactic Winds

3.1 Preface

This chapter is adapted from a work appearing in the Monthly Notices of the Royal Astronomical Society, Volume 490, Issue 1 (*Holguin et al.*, 2019). I am the lead author, and it is coauthored by M. Ruszkowski, A. Lazarian, R. Farber, and H.-Y. K. Yang.

3.2 Abstract

Large-scale galactic winds driven by stellar feedback are one phenomenon that influences the dynamical and chemical evolution of a galaxy, redistributing material throughout the circumgalatic medium. Non-thermal feedback from galactic cosmic rays (CRs)—high-energy charged particles accelerated in supernovae and young stars – can impact the efficiency of wind driving. The streaming instability limits the speed at which they can escape. However, in the presence of turbulence, the streaming instability is subject to suppression that depends on the magnetization of turbulence given by its Alfvén Mach number. While previous simulations that relied on a simplified model of CR transport have shown that super-Alfvénic streaming of CRs enhances

galactic winds, in the present paper we take into account a realistic model of streaming suppression. We perform three-dimensional magnetohydrodynamic simulations of a section of a galactic disk and find that turbulent damping dependent on local magnetization of turbulent interstellar medium (ISM) leads to more spatially extended gas and CR distributions compared to the earlier streaming calculations, and that scale-heights of these distributions increase for stronger turbulence. Our results indicate that the star formation rate increases with the level of turbulence in the ISM. We also find that the instantaneous wind mass loading is sensitive to local streaming physics with the mass loading dropping significantly as the strength of turbulence increases.

3.3 Introduction

The baryon-to-halo mass ratio in galaxies is considerably lower than the cosmological average (*Bell et al.*, 2003). At L_*, roughly the Milky Way (MW) luminosity, about 20 percent of baryons are accounted for when matching the observed luminosity to the halo mass function, while at higher or lower luminosities the discrepancy widens (*Guo et al.*, 2010). Additionally, absorption lines in background quasars provide evidence for the pollution of the intergalactic medium (IGM) with the products of stellar evolution formed only deep in the galactic potential well, such as dust (e.g., *Ménard and Fukugita*, 2012) and metals (e.g., *Songaila*, 2001), up to at least redshift $z = 6$, suggesting that galactic baryons were expelled due to feedback.

At higher luminosities than L_*, feedback from active galactic nuclei (AGN) dominates (e.g., *Croton et al.*, 2006). For lower luminosities, stellar feedback can drive galactic outflows, pushing and redistributing material, significantly affecting the dynamical and chemical evolution of galaxies (*Larson*, 1974; *White and Rees*, 1978; *Dubois and Teyssier*, 2010). Indeed, galactic winds have been observed in galaxies that have had recent and significant star formation (*Veilleux et al.*, 2005), driving

gas out at a rate of 0.01 to 10 times the star formation rate (SFR) (*Bland-Hawthorn et al.*, 2007).

The stellar feedback which drives winds is likely the result of several mechanisms combining in a non-linear manner (e.g., *Agertz et al.*, 2013). A detailed understanding of the exact mechanisms and their complex interactions remains uncertain, as many processes operate below the grid scale of simulations in galactic and cosmological simulations (*Somerville and Davé*, 2015).

Mechanisms used to explain winds are thermal (*Chevalier and Clegg*, 1985; *Joung et al.*, 2009) and momentum (*Kim et al.*, 2016) feedback from supernovae (SN), as well as radiation pressure from massive stars (*Murray et al.*, 2005, 2011; *Hopkins et al.*, 2012). Galactic cosmic rays (CRs), originating from shock acceleration in SN remnants (see *Bykov et al.*, 2018) and winds from massive stars (see *Bykov*, 2014) can also play a significant role in launching galactic winds. In the MW, the CR energy density is in rough equipartition with the turbulent and magnetic field energy densities (e.g., *Boulares and Cox*, 1990). Additionally, Fermi γ-ray observations of starburst galaxies M82 and NGC 253 suggest CR energy densities two orders of magnitude above the MW values (*Paglione and Abrahams*, 2012; *Yoast-Hull et al.*, 2013). These two findings hint at the importance of CRs in the evolution of galaxies. Theoretical considerations suggest that CRs can play important role in driving gas in galactic winds (*Everett et al.*, 2008; *Breitschwerdt et al.*, 1991). Three-dimensional hydrodynamical (*Uhlig et al.*, 2012; *Booth et al.*, 2013; *Salem and Bryan*, 2014) and magneto-hydrodynamical (MHD) (*Hanasz et al.*, 2013; *Girichidis et al.*, 2016; *Pakmor et al.*, 2016) simulations have demonstrated that CRs indeed influence the generation of global outflows and the local structure of the interstellar medium (ISM). The exact properties of the simulated outflows depend sensitively on how CR transport is modeled (*Simpson et al.*, 2016; *Ruszkowski et al.*, 2017; *Farber et al.*, 2018).

In the self-confinement model of CR transport, CRs propagating in one direction

along the magnetic field in the galaxy generate Alfvén waves that scatter CRs back, thus amplifying the waves. This process is called the streaming instability and in the absence of wave dissipation it was shown to reduce the CR bulk streaming speed u_s (relative to the gas) to the Alfvén speed u_A (see *Kulsrud and Pearce*, 1969). This effectively couples the plasmas with the CRs. In terms of galactic winds this means that the flux of CRs can transfer its momentum to the wind material.

If the dissipation of Alfvén waves is present, the streaming instability can still be present and the coupling of the waves and the wind is decreased. Historically, the damping of the Alfvén waves in the context of streaming instability suppression is associated with the ion-neutral linear damping process (*Kulsrud and Pearce*, 1969). This process is not efficient for the highly ionized matter expected to form galactic winds. However, it was noted in *Yan and Lazarian* (2002) that the streaming instability can be suppressed by turbulence. *Farmer and Goldreich* (2004) proposed a model for trans-Aflvénic strong MHD turbulence, corresponding to the Alfvén Mach number $M_A = u_L/u_A = 1$, where u_L is the injection velocity at the turbulence injection scale L. This study was generalized for the arbitrary M_A in *Lazarian* (2016), where it was shown that the damping significantly changes with M_A. Moreover, the latter study showed that the scaling for the dependences of the damping of the streaming instability for $M_A < 1$ is different for high energy CRs that induce waves that are non-linear damped by the *weak* Alfvenic turbulence (see *Lazarian and Vishniac*, 1999; *Galtier et al.*, 2000) that spans the range from LM_A^2 to L and the lower energy cosmic rays that induce waves that are non-linearly damped by the *strong* MHD turbulence existing at the scales less than LM_A^2. Note, that the terms *weak* and *strong* turbulence do not reflect the amplitude of Alfvénic perturbations, but the strength of non-linear interactions (see *Brandenburg and Lazarian*, 2013).

Observations of the MW suggest that the case of $M_A < 1$ is the most appropriate for the turbulence at high galactic latitudes corresponding to the action of the galactic

wind (see *Kandel et al.*, 2018). The magnetically dominated, i.e. low β [1] media is also expected for the galactic wind environment. Therefore we do not consider the non-linear Landau damping (*Zweibel*, 2013) that may be important for the damping of Alfven waves in high β media. The turbulent damping of the streaming instability is a robust process that depends only on the turbulence properties and does not depend on plasma β. Our present study is focused on studying the consequences of this process for the generation and the evolution of galactic winds and resulting galactic properties.

The important earlier work that considered the effects of the launching of the galactic winds with CRs and taking into account the effects of the streaming instability is *Ruszkowski et al.* (2017). There, a simple parameterization $u_s = f u_A$ was considered for the CR streaming speed in three-dimensional MHD simulations of an isolated galaxy (f was assumed to be constant). In these simulations, the CR streaming generally enhances the efficiency of galactic wind driving, as the CRs can escape from dense regions and interact with more tenuous gas that is easier to accelerate. As the efficiency of wind coupling with CRs is determined by the efficiency of the turbulent damping of the streaming instability, it is essential to properly model this process. In implementing a more physically motivated model compared to that adopted by *Ruszkowski et al.* (2017), we use the model of turbulent damping in *Lazarian* (2016) and provide the more accurate description of the turbulent damping of Alfvén waves. We calculate the resulting streaming speed that depends on the local properties of the ISM and halo. We perform three-dimensional MHD simulations of a section of a MW-like galactic disk in order to investigate the effects of locally-determined CR streaming controlled by the turbulent structure of the ISM. We include magnetic fields, radiative cooling, self-gravity, and stellar feedback (star formation and SN, with thermal and CR injection). In Section 2, we describe the treatment of numerical

[1] β is the ratio of the gaseous pressure to the magnetic pressure.

methods and physical models, while in Section 3 we discuss results, with conclusions in Section 4.

3.4 Methods

We run simulations with the adaptive mesh refinement MHD code FLASH 4.2 (*Fryxell et al.*, 2000; *Dubey et al.*, 2008) using a directionally unsplit staggered mesh (USM) solver (*Lee and Deane*, 2009; *Lee*, 2013), including CR physics (*Yang et al.*, 2012; *Ruszkowski et al.*, 2017; *Farber et al.*, 2018), in an elongated box of dimensions $2 \times 2 \times 40$ kpc^3.

We solve the MHD equations with a two-fluid model (*Salem and Bryan*, 2014; *Ruszkowski et al.*, 2017), including both thermal gas and ultra-relativistic CR fluid (composed of protons) characterized by adiabatic indices $\gamma = 5/3$ and $\gamma_{\rm cr} = 4/3$, respectively. We use a mean CR Lorentz factor $\gamma_{\rm rel} = 3$, and a slope $n = 4.5$ for the CR distribution function in momentum, which are typical values for galactic CRs.

We include CR advection, dynamical coupling between CRs and thermal gas, CR streaming along the magnetic field lines and the associated heating of gas by CRs, gas self-gravity, radiative cooling, star formation, and evolve the following equations:

$$\frac{\partial \rho}{\partial t} + \boldsymbol{\nabla} \cdot (\rho \boldsymbol{u}_g) = -\dot{m}_{\rm form} + f_* \dot{m}_{\rm feed} \tag{3.1}$$

$$\frac{\partial \rho \boldsymbol{u}_g}{\partial t} + \boldsymbol{\nabla} \cdot \left(\rho \boldsymbol{u}_g \boldsymbol{u}_g - \frac{\boldsymbol{B}\boldsymbol{B}}{4\pi} \right) + \boldsymbol{\nabla} p_{\rm tot} = \rho \boldsymbol{g} + \dot{p}_{\rm SN} \tag{3.2}$$

$$\frac{\partial \boldsymbol{B}}{\partial t} - \boldsymbol{\nabla} \times (\boldsymbol{u}_g \times \boldsymbol{B}) = 0 \tag{3.3}$$

$$\frac{\partial e}{\partial t}+\boldsymbol{\nabla}\cdot\left[(e+p_{\rm tot})\boldsymbol{u}_g-\frac{\boldsymbol{B}(\boldsymbol{B}\cdot\boldsymbol{u}_g)}{4\pi}\right]=\rho\boldsymbol{u}_g\cdot\boldsymbol{g} - \nabla\cdot\boldsymbol{F}_{\rm cr}-C+H_{\rm SN} \tag{3.4}$$

$$\frac{\partial e_{\rm cr}}{\partial t}+\boldsymbol{\nabla}\cdot(e_{\rm cr}\boldsymbol{u}_g)=-p_{\rm cr}\nabla\cdot\boldsymbol{u}_g-H_{\rm cr}+H_{\rm SN} - \nabla\cdot\boldsymbol{F}_{\rm cr} \tag{3.5}$$

$$\Delta\phi=4\pi G\rho_b \tag{3.6}$$

where ρ is the gas density, ρ_b is the total baryon density including both the gas and stars, $\dot{m}_{\rm form}$ is the density sink from stellar population particle formation, $f_*\dot{m}_{\rm feed}$ represents the gas density source from stellar feedback (see Section 4.4.2), $\boldsymbol{u}_g$ is the gas velocity, $\boldsymbol{B}$ is the magnetic field, G is the gravitational constant, ϕ is the gas gravitational potential, $\boldsymbol{g}=-\boldsymbol{\nabla}\phi+\boldsymbol{g}_{\rm NFW}$ is the gravitational acceleration (the sum of gas self-gravity, stellar particle, and halo dark matter contributions to the gravitational acceleration, described in Section 4.4.1) where $\boldsymbol{g}_{\rm NFW}$ is the gravity from the Navarro-Frenk-White (NFW) potential, $p_{\rm tot}$ is the sum of gas ($p_{\rm th}$), magnetic, and CR ($p_{\rm cr}$) pressures, $\dot{p}_{\rm SN}$ is the momentum injection due to stellar winds and SN. Furthermore, $e=\rho\boldsymbol{u}_g^2+e_g+e_{\rm cr}+B^2/8\pi$ is the total energy density per volume (the sum of gas, CR, and magnetic components, respectively), C is the radiative cooling rate per unit volume, and $H_{\rm SN}$ is the supernova heating rate per volume. CR advection and coupling to the gas are included using the same methods as in *Ruszkowski et al.* (2017) (see *Yang et al.*, 2012, 2013; *Sharma et al.*, 2009) with the CR streaming flux denoted by $\boldsymbol{F}_{\rm cr}$ and an associated CR heating of the gas denoted by $H_{\rm cr}$. The streaming flux is $\boldsymbol{F}_{\rm cr}=(e_{\rm cr}+p_{\rm cr})\boldsymbol{u}_s$, with the streaming speed along the magnetic field down the CR gradient $\boldsymbol{u}_s\propto-{\rm sgn}(\hat{\boldsymbol{b}}\cdot\nabla e_{\rm cr})\simeq\tanh(h_c\hat{\boldsymbol{b}}\cdot\nabla e_{\rm cr}/e_{\rm cr})$, where $\hat{\boldsymbol{b}}$ is the magnetic

direction vector. When damping processes are included, we write $\boldsymbol{u}_s = f\boldsymbol{u}_A$, where f is a function of local gas properties (see Section 2.4). The regularization parameter $h_c = 10$ kpc helps avoid prohibitively small time-steps due to discontinuities in $\boldsymbol{F}_{\rm cr}$ near extrema of the CR energy density distribution (*Sharma et al.*, 2009). The streaming speed is limited to 200 km/s for computational efficiency. We have tested higher ceilings finding no significant change in the results. Additionally, we sub-cycle four times over the CR streaming term to further accelerate computations.

3.4.1 Gravity

The gravitational acceleration has contributions from the gravity of gas, stellar particles, and dark matter halo vertical component. We do not include a pre-existing stellar potential, instead we allow the gravitational contribution from stars to be set up by the stellar particles. For the self-gravity of baryons, we solve the Poisson equation with the Barnes-Hut tree solver (*Barnes and Hut*, 1986) implemented by *Wunsch et al.* (2018). We also include the gravitational contribution from the overall dark matter halo (*Navarro et al.*, 1997). Since the domain is a thin slice of a galaxy, we only use the vertical component of gravity

$$g_{\rm NFW}(z) = -\frac{GM_{200}}{|z|^3}\frac{\ln(1+x) - x/(1+x)}{\ln(1+c) - c/(1+c)} \tag{3.7}$$

where G is the gravitational constant, M_{200} is the halo virial mass, z is the height above the mid-plane, $x = |z|c/r_{200}$, c is the halo concentration parameter, and r_{200} is the virial radius. Table 3.1 summarizes the parameters we use.

3.4.2 Radiative Cooling

We use the Townsend cooling method (*Townsend*, 2009; *Zhu et al.*, 2017) implemented as in *Farber et al.* (2018). The cooling function $\Lambda(T)$ is a piecewise power law with a floor temperature of 300 K (*Rosen and Bregman*, 1995) given in units of

erg cm^{3}s^{-1} by

$$\Lambda(T) = \begin{cases} 0 & \text{if } T < 300 \\ 2.2380 \times 10^{-32} T^{2.0} & \text{if } 300 \leq T < 2000 \\ 1.0012 \times 10^{-30} T^{1.5} & \text{if } 2000 \leq T < 8000 \\ 4.6240 \times 10^{-36} T^{2.867} & \text{if } 8000 \leq T < 10^5 \\ 1.7800 \times 10^{-18} T^{-0.65} & \text{if } 10^5 \leq T < 4 \times 10^7 \\ 3.2217 \times 10^{-27} T^{0.5} & \text{if } 4 \times 10^7 \leq T, \end{cases} \tag{3.8}$$

where T is the gas temperature in K. This cooling function is an approximation to the radiative cooling functions in *Dalgarno and McCray* (1972) and *Raymond et al.* (1976), accurate for a gas of solar abundance that is completely ionized gas at $T = 8000$ K. The Townsend scheme does not impose restrictions on the cooling time step.

3.4.3 Star Formation and Feedback

Star formation follows the approach of *Cen and Ostriker* (1992) (see also *Tasker and Bryan*, 2006; *Bryan et al.*, 2014; *Salem and Bryan*, 2014; *Li et al.*, 2015), where star formation occurs when all of the following conditions are met: (i) gas density exceeds 1.67×10^{-23}g cm^{-3} (*Gnedin and Kravtsov*, 2011; *Agertz et al.*, 2013); (ii) the cell mass exceeds the local Jeans mass; (iii) $\nabla \cdot \boldsymbol{u}_g < 0$; (iv) gas temperature reaches the floor of the cooling function or the cooling time becomes shorter than the dynamical time $t_{\rm dyn} = \sqrt{3\pi/(32G\rho_b)}$. When these conditions are satisfied, a stellar population particle is formed instantaneously at a random position in the cell, with the same velocity as the gas, and mass $m_* = \epsilon_{\rm SF}(dt/t_{\rm dyn})\rho dx^3$, where $\epsilon_{\rm SF} = 0.05$ is the star formation efficiency, dt is the timestep, and dx is the local cell size. There is a corresponding removal of gas mass from the surrounding cell.

In order to keep the number of particles manageably small we set a minimum

particle mass $m_{*,\rm min} = 10^5 M_\odot$. We still permit particles with $m_* < m_{*,\rm min}$ to form; their masses are given by $m_* = 0.8\rho dx^3$ forming with a probability $m_*/m_{*,\rm min}$.

We include stellar feedback from winds and SN by adding gas mass, thermal energy, and CR energy into the cell surrounding a particle. For this feedback, the assumed stellar mass within a particle is not modeled as instantaneous, as stars form and evolve over time. The stellar mass increases at a rate of $\dot{m} = m_*(\Delta t/\tau^2)\exp(-\Delta t/\tau)$, where Δt is the time since formation of the particle, and $\tau = \max(t_{\rm dyn}, 10\ {\rm Myr})$. Gas mass is added at a rate $f_*\dot{m}_{\rm feed} = f_*\dot{m}$ into the cell surrounding a stellar population particle. The injected gas has a velocity equal to that of the source particle, thermal energy equal to $(1 - f_{\rm cr})\epsilon_{\rm SN}\dot{m}c^2$, and CR energy equal to $f_{\rm cr}\epsilon_{\rm SN}\dot{m}c^2$, where $f_{\rm cr}$ is the fraction of total SN energy given to CRs. We assume $f_* = 0.25$ for the fraction of returned mass from the star to the ISM and $\epsilon_{\rm SN} = 10^{51}$ erg/($\rm M_{\it sf} c^2$) for the energy injected by one supernova per $\rm M_{sf} = 100 M_\odot$ (*Guedes et al.*, 2011; *Hanasz et al.*, 2013) of mass of a newly formed stellar population particle, corresponding to a *Kroupa* (2001) initial mass function. The mass of the stellar population particle is reduced appropriately after the gas injection into the ISM. The parameter choices are summarized in Table 3.1.

3.4.4 Cosmic Ray Streaming

In the self-confinement model of CR transport through the ISM, CRs stream along magnetic field lines, exciting Alfvén waves due to the streaming instability, subsequently limiting the CR streaming speed to the Alfvén speed (*Zweibel*, 2013).

As relativistic, charged particles (usually protons), CRs gyrate around a local magnetic field line at the frequency $\Omega_0/\gamma_{\rm rel}$ and gyro-radius $r_L = \gamma_{\rm rel} c/\Omega_0$, where c is the speed of light, $\gamma_{\rm rel}$ is the Lorentz factor, $\Omega_0 = eB/m_p c$ is the non-relativistic cyclotron frequency, and m_p and e are the proton mass and charge, respectively. CRs strongly interact with Alfvén waves when the resonance condition $k_{||} = 1/(\mu r_L)$ is

Table 3.1: Model parameters

Halo	
$M_{200}^{(1)}$	$10^{12}\mathrm{M}_{\odot}$
$c^{(2)}$	12
Disk	
$\rho_o^{(3)}$	5.24×10^{-24} g cm^{-3}
$z_o^{(4)}$	0.325 kpc
$\Sigma_o^{(5)}$	100 $\mathrm{M}_{\odot}$ pc^{-2}
$T_o^{(6)}$	10^4 K
$B_o^{(7)} = B_{o,x}$	3 μG
Star Formation	
$n_{\mathrm{thresh}}^{(8)}$	10 cm^{-3}
$T_{\mathrm{floor}}^{(9)}$	300 K
$m_{*,\mathrm{min}}^{(10)}$	10^5 $\mathrm{M}_{\odot}$
$\epsilon_{\mathrm{SF}}^{(11)}$	0.05
Stellar Feedback	
$f_*^{(12)}$	0.25
$f_{cr}^{(13)}$	0.1
$\epsilon_{\mathrm{SN}}^{(14)}$	$10^{51}\mathrm{erg}/(\mathrm{M}_{\mathrm{sf}}\mathrm{c}^2)$
$M_{\mathrm{sf}}^{(15)}$	100 $\mathrm{M}_{\odot}$

Notes. From top to bottom the rows contain: (1) halo mass; (2) concentration parameter; (3) initial midplane density; (4) initial scale height of the gas disk; (5) initial gas surface density; (6) initial temperature; (7) initial magnetic field strength; (8) gas density threshold for star formation; (9) floor temperature; (10) minimum stellar population particle mass; (11) star formation efficiency; (12) fraction of stellar mass returned to the ISM; (13) fraction of supernova energy bestowed unto CRs; (14) SN energy per rest mass energy of newly formed stars; (15) rest mass energy of newly formed stars per SN.

met; the Alfvén parallel wavevector $k_{||}$ (with respect to the local magnetic field) is of order the inverse of the CR gyro-radius projected onto the plane of the wave by the cosine of the pitch angle μ. At smaller gyro-radii, the local magnetic field does not change much over a CR orbit reducing the interaction, and at larger gyro-radii, the CR samples a large enough spatial region that the effects of the fluctuating field cancel out over the orbit.

Alfvén waves are amplified by resonant scattering of CRs at a rate shown by *Kulsrud and Pearce* (1969) and *Wentzel* (1974)

$$\Gamma_g \approx \frac{\pi}{6}\Omega_0 \frac{n_{\rm cr}(>\gamma_{\rm rel})}{n_i}\left(\frac{u_s}{u_A}-1\right), \tag{3.9}$$

where $n_{\rm cr}(>\gamma_{\rm rel})$ is the number density of CRs with sufficiently large gyro-radii (directly dependent on $\gamma_{\rm rel}$ and also the CR energy) to be resonant with the Alfvén wave, n_i is the ion number density, and u_A is the Alfvén speed. CRs with larger gyro-radii can still be resonant as the projection of the orbit to the plane of the wave can meet the resonance condition. Amplification of Alfvén waves occurs until the CRs become isotropic in the wave frame and stream at u_A. In addition to growth, Alfvén waves experience damping by various mechanisms, in particular by ion-neutral friction, non-linear Landau damping, or turbulent damping. As a result of this damping, CR motion will be super-Alfvénic to a degree depending on the damping rate.

Given that the galactic astrophysical environment is magnetized, turbulent, and significantly ionized (*McKee and Ostriker*, 2007; *Sharma et al.*, 2009; *Brandenburg and Lazarian*, 2013), we consider the effects of MHD turbulence stirred up by SN feedback. This was originally suggested by *Yan and Lazarian* (2002) and quantified in *Farmer and Goldreich* (2004) using the strong, incompressible MHD cascade (*Goldreich and Sridhar*, 1995).

As Alfvén waves pass through turbulent eddies, they are irreversibly distorted. The turbulent eddies are anisotropic and aligned with the magnetic field (e.g., *Higdon*,

Table 3.2: Summary of CR streaming speed boost $f-1$ above Alfvénic streaming for four different regimes of MHD turbulence (*Lazarian*, 2016) with given inertial range, where M_A is the turbulent Mach number, r_L is the CR gyro-radius, and L is the turbulence injection scale. The ratio $l_{\rm min}/L << 1$, where the $l_{\rm min}$ is the thermal ion gyro-radius.

Turbulence	M_A	Inertial Range	Γ_d	$f-1$
Weak	<1	$M_A^4 < \frac{r_L}{L} < M_A$	$\frac{u_A M_A^{8/3}}{r_L^{2/3} L^{1/3}}$	$\frac{u_A}{\Omega_0}\frac{n_i}{n_{\rm cr}}\frac{M_A^{8/3}}{r_L^{2/3} L^{1/3}}$
Strong	<1	$\left(\frac{l_{\rm min}}{L}\right)^{4/3} < \frac{r_L}{L} < M_A^4$	$\frac{u_A M_A^{2}}{r_L^{1/2} L^{1/2}}$	$\frac{u_A}{\Omega_0}\frac{n_i}{n_{\rm cr}}\frac{M_A^{2}}{r_L^{1/2} L^{1/2}}$
Strong	>1	$\left(\frac{l_{\rm min}}{L}\right)^{4/3} M_A < \frac{r_L}{L} < M_A^{-3}$	$\frac{u_A M_A^{3/2}}{r_L^{1/2} L^{1/2}}$	$\frac{u_A}{\Omega_0}\frac{n_i}{n_{\rm cr}}\frac{M_A^{3/2}}{r_L^{1/2} L^{1/2}}$
Hydro	>1	$M_A^{-3} < \frac{r_L}{L} < 1$	$\frac{u_A M_A^{3/2}}{r_L^{2/3} L^{1/3}}$	$\frac{u_A}{\Omega_0}\frac{n_i}{n_{\rm cr}}\frac{M_A^{3/2}}{r_L^{2/3} L^{1/3}}$

1984). As a result of this anisotropy, the Alfvén waves that experience the least amount of distortion are those with wave vector parallel to the local magnetic field, which is exactly the case for the waves generated by the streaming instability.

The damping rates depend on the properties of turbulence that exists in the environment, which is characterized by the turbulent Alfvén Mach number $M_A = \frac{\sigma}{u_A}$, where σ is the gas velocity dispersion, and the inertial range of the turbulence, depending on the ratio of the CR gyro-orbit to the injection length scale. Turbulence can be sub-Alfvénic, $M_A < 1$, and either strong or weak, depending on whether r_L/L is greater or less than M_A^4 respectively. L is the length scale at which turbulence is driven. Turbulence can also be super-Alfvénic, $M_A > 1$, and either strong or hydro-like, depending on whether r_L/L is greater or less than M_A^{-3} respectively. *Lazarian* (2016) provides a general study of the Alfvén wave damping rates Γ_d for each regime of turbulence. The results are summarized in Table 3.2.

Following *Wiener et al.* (2013b) and *Ruszkowski et al.* (2017), we can parameterize the CR transport speed by balancing the Alfvén wave growth and turbulent damping rates. As an example, we derive the CR streaming speed assuming the weak, sub-

Alfvénic turbulent damping rate $\Gamma_{d,\mathrm{weak}}$ and compare it to the streaming instability growth rate

$$\begin{aligned} \Gamma_g &= \Gamma_{d,\mathrm{weak}} \\ \frac{\pi}{6}\Omega_0 \frac{n_{\mathrm{cr}}(>\gamma_{\mathrm{rel}})}{n_i}\left(\frac{u_s}{u_A}-1\right) &= \frac{M_A^{8/3}}{r_L^{2/3}L^{1/3}}u_A \end{aligned} \tag{3.10}$$

we then solve for the streaming speed u_s

$$u_s = u_A\left(1+\frac{u_A}{\Omega_0}\frac{n_i}{n_{\mathrm{cr}}\left(>\gamma_{\mathrm{rel}}\right)}\frac{M_A^{8/3}}{r_L^{2/3}L^{1/3}}\right). \tag{3.11}$$

We set the length scale $L = 10$ pc (*Iacobelli et al.*, 2013). A similar analysis using the damping rates appropriate for the other turbulence regimes yields the remaining three expressions for the streaming speed. In general, we write

$$u_{\mathrm{s}} = u_A f(n_i, n_{\mathrm{cr}}, B, \sigma), \tag{3.12}$$

where the proportionality f is a function of ion and CR number densities, n_i and n_{cr}, magnetic field strength B, and velocity dispersion σ.

The streaming speed boost above the Alfvén speed ($f-1$) is listed in the last column in Table 3.2. The expressions for the boost show expected dependencies on the environment. The streaming boost is proportional to n_i and σ and inversely proportional to B and n_{cr}. For higher ion density or velocity dispersion, all other parameters fixed, stronger turbulence can more efficiently damp Alfvén waves, leading to faster CR propagation. On the other hand, a higher magnetic field strength results in higher growth rate of Alfvén waves due to the streaming instability, trapping CRs more effectively and thus reducing their effective speed. Similarly, a greater density of CRs generates more Alfvén waves, also trapping CRs more effectively and slowing

down CR propagation. In our simulations we use a constant velocity dispersion. The assumption of constant velocity dispersion is consistent with the decay of the turbulence strength from central star formation regions to the halo (*Stone et al.*, 1998) as the turbulent Alfvén Mach number, M_A, still decreases with height above the midplane because the Alfvén speed increases. We compare results of simulations with two different gas velocity dispersion values $\sigma = 5$ km/s and 10 km/s, which are representative of turbulence in the disk, as the turbulent structure near the disk (where the wind is launched) will most likely dictate the resulting galactic wind structure and evolution (*Kim and Ostriker*, 2018). Therefore, we do not expect the results to change significantly if instead of considering constant σ, we use a σ profile declining with distance from the midplane. We choose constant σ also because quantifying σ on-the-fly in the simulation would pose additional challenges associated with averaging velocities over finite volumes.

CRs experience an effective drag force as they propagate down the pressure gradient $\nabla p_{\rm cr}$ and scatter off MHD waves, leading to heating of gas. The collisionless heating term $H_{\rm cr} = |\boldsymbol{u}_A \cdot \nabla p_{\rm cr}|$ depends on the Alfvén speed u_A and not the potentially super-Alfvénic streaming speed u_s because the transfer of energy from CRs to the gas is only due to the portion of streaming caused by MHD waves (see the Appendix in *Ruszkowski et al.*, 2017). We do not include loss of CR energy due to hadronic or Coulomb losses (collisional heating of gas) in the $H_{\rm cr}$ term.

3.4.5 Simulation Setup

We simulate a section of a galactic disk in an box of dimensions $2 \times 2 \times 40$ kpc^3, elongated in the direction z above the mid-plane. Previous work has shown the importance of including sufficient height in these types of slab simulations in establishing a realistic temperature distribution in the halo (*Hill et al.*, 2012). We choose the vertical extent of the box to be equal to 40 kpc. A box of such height is

sufficiently extended to limit the above-mentioned problem, while not compromising feasibility of our computations.

We use periodic boundary conditions for the box sides perpendicular to the disk plane and diode boundary conditions for those parallel to the disk plane. The diode boundary conditions do not allow in-fall back into the box (e.g., *Sur et al.*, 2016). We do not include the effects of differential rotation due to large scale galactic motion in order to simplify the simulation and focus on feedback processes. We use static mesh refinement that varies according to height $|z|$ above the mid-plane, achieving a maximum resolution of 31.25 pc in the disk for $|z| < 2$ kpc, and progressively coarser resolution of 62.5 pc for 2 kpc $< |z| <$ 5 kpc, and a minimum resolution of 125 pc elsewhere in the halo.

We initialize the simulation with the vertical equilibrium density solution for a stratified, isothermal self-gravitating system (*Spitzer Jr*, 1942; *Salem and Bryan*, 2014) within a stratified box model (e.g., *De Avillez and Breitschwerdt*, 2007; *Walch et al.*, 2015; *Farber et al.*, 2018) as follows

$$\rho(z) = \begin{cases} \rho_0 \operatorname{sech}^2\left(\frac{z}{2z_0}\right) & \rho(z) > \rho_{\rm halo} \\ \rho_{\rm halo} & \text{otherwise,} \end{cases} \tag{3.13}$$

where ρ_0 is the initial mid-plane density and z_0 is the vertical scale height. We can define the initial disk surface gas density as $\Sigma_0 = \int_{-20\rm kpc}^{20\rm kpc} \rho(z)\mathrm{d}z$. $\rho_{\rm halo} = 1.0 \times 10^{-28}\mathrm{g/cm}^3$ is the initial density of the halo.

The parameters that we chose for the spatial distribution of the gas correspond to total gas surface density of around 100 100 $M_\odot/\mathrm{pc}^2$. This value of the surface density is computed by averaging within a radius of 10 kpc the isothermal self-gravitating solution described by Eq. 4.16, assuming MW-type baryon fraction. The initial gas surface density is on the order of the average gas surface density at a radius of around $r = 8$ kpc.

The overall gravitational potential is comparable to that of other works. When most of the stellar particles have formed, the stellar particle surface density in the simulations approaches about 20 $M_\odot$ pc^{-2}, which is comparable to the pre-existing stellar surface density of 30 $M_\odot$ pc^{-2} assumed by *Walch et al.* (2015). However, *Walch et al.* (2015) assumes an initial gas surface density of 10 $M_\odot$ pc^{-2}, so the gravitational potential due to gas is lower in our simulations.

The magnetic field is initially oriented along a horizontal direction and its magnitude follows the density distribution such that $B(z) \propto \rho(z)^{2/3}$ with the mid-plane value $B_0 \approx 3\mu G$. We initialize the simulation with a constant temperature $T = 10^4$ K. The setup is initially out of thermal equilibrium. At the beginning of the simulation, the gas distribution will collapse due to radiative cooling, and begin the formation of stellar population particles. Subsequent stellar feedback will suppress star formation at about 50 Myr in the simulation. Some previous works such as *Kim and Ostriker* (2017) initially drive turbulence in the disk in order to achieve convergence in the simulation more quickly. We choose not to include initial artificial pressure support. The resulting steady-state properties are insensitive to the choices for initial artificial pressure support (*Kim and Ostriker*, 2017).

In the Alfvén wave damping formualae, we assume the gas is completely ionized so $n_i = n_{\rm gas}$, where $n_{\rm gas} = \rho/m_p$ is the total number gas density, composed of purely hydrogen. Since the wind is launched in the diffuse, ionized medium above the mid-plane, this is a good approximation. Of course, in the denser disk, near-complete ionization of gas not necessarily the case. In these regions, the CR streaming speed boost determined with turbulent damping is overestimated as the CR streaming speed is proportional to the n_i, which will increase significantly. However, there are two reasons why our approximation is still justified. First, the dense regions are not volume filling, so the impact of approximation is mitigated. Second, fast CR streaming likely occurs anyways in realistic scenarios, as other damping processes (i.e. ion-neutral

damping) dominate in denser regions.

3.5 Results

We compare five simulations that differ in the value of the CR steaming speed $u_s = f u_A$ (see columns in Figure 3.6). The first case includes CRs without transport processes beyond advection with gas ($f = 0$). The second case is purely Alfvénic CR streaming with $f = 1$, where there is no dissipation of Alfvén waves. The third and fourth cases correspond to locally-determined CR streaming following Eq. 3.12 using the appropriate turbulence regime for the environment. The local streaming simulations assume a constant velocity dispersion, $\sigma = 5$ km/s or 10 km/s, in the turbulent damping formulae from Table 3.2. These values of velocity dispersion are on the order of the sound speed. The actual velocity dispersions reached at peak mass flow within the kpc wind launching region vary roughly between 10 to 25 km/s, which includes our assumed velocity dispersion of 10 km/s. Observationally, these values are plausible. For example, *Boettcher et al.* (2016) found an upper limit of 25 km/s for turbulent velocity dispersion from optical emission-line spectroscopy in the edge-on galaxy NGC 891. The fifth case assumes constant $M_A = 1$ (trans-Alfvenic turbulence) in the damping formulae, corresponding to the damping from *Farmer and Goldreich* (2004).

Since the wind is launched [2] from a roughly one kpc tall region just above the dense and thin galactic disk, we first examine where this region in our simulations falls in the parameter space of the CR streaming speed. A discussion of the parameter space is important as we can only consider a limited number of simulations. Examining the parameter space allows us to develop intuition for the possible results of a simulation.

[2]We refer to the outflow as a 'wind' even though the outflow velocity may not exceed the escape velocity of the halo. Cosmic rays continuously accelerate gas, so even if the velocity is not greater than the escape velocity near the disk, the gas can still reach the virial radius. Furthermore, in a global 3-dimensional gravitational potential, it is easier to launch a wind, compared to a one-dimensional potential, as the field strength decays faster *Martizzi et al.* (2016).

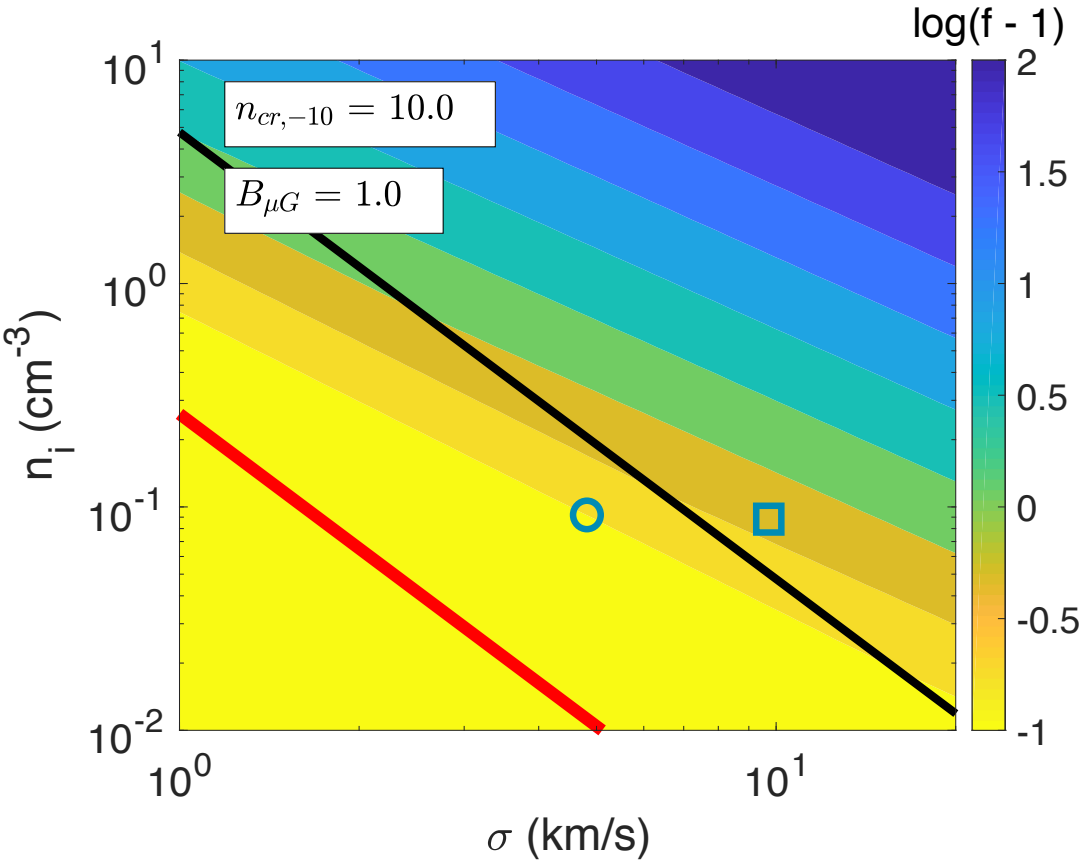

Figure 3.1: The parameter space for the CR streaming speed boost $f - 1$ factor for fixed magnetic field strength B and CR number density $n_{\rm cr}$, and varying ion density n_i and velocity dispersion σ. The magnetic field strength is shown in units of μG and the CR number density is units of 10^{-10} cm^{-3}. The damping formulae in Table 3.2 are used. Below a value of $\log(f - 1)$ = -1, shown in yellow, there is no significant super-Alvénic CR streaming and turbulent damping is ineffective. The black line indicates the boundary $M_A = 1.0$ and the red line indicates the transition from weak to strong, sub-Alfvénic turbulence. The parameters we use for the plot correspond to approximate values of quantities within the kpc size ionized ISM, above the thin galactic disk. The circle and box denote $n_i = 0.1$ cm^{-3} and velocity dispersions of 5 km/s and 10 km/s respectively.

Average values of the ionized ISM in our simulations are $n_{\rm cr} \sim 10^{-9}$ cm^{-3}, $B \sim \mu G$, and $n_i \sim 10^{-1}$ cm^{-3}. Figure 3.1 shows the parameter space for these values, where CR streaming is expected to be nearly Alfvénic with $\log(f-1) < 0.1$, and also shows the transition to significantly super-Alfvénic streaming. At a velocity dispersion $\sigma = 10$ km/s, the parameter space plot indicates that super-Alfvénic streaming is significant for the typical density of $n_i \sim 10^{-1}$ cm^{-3} in the launching region, as labeled by a blue box in the figure. Furthermore, since the typical ion density value we see is an average over all of the cells at a given height above the mid-plane, we can expect cells of even faster or slower CR streaming compared to u_A from the slightly over or under-dense regions (see the slice plots in Figure 3.2 for a qualitative look at the variation in density). Additionally, for the parameters shown, the wind launching regions is close to the black $M_A = 1$ line where turbulence transitions from $M_A < 1$ to $M_A > 1$. While we expect $M_A < 1$ farther out in the halo, closer to the disk the properties of turbulence will vary depending on the local conditions. In particular, an increase in the magnetic field strength will shift the $M_A = 1$ line to higher densities. This indicates that in the higher turbulence simulation, there will be regions where turbulence is super-Alfvénic because of lower magnetic field strength or higher ion density than average. At a velocity dispersion of $\sigma = 5$ km/s, the typical gas density falls mostly in the region of Alfvénic streaming, as labeled by a blue circle in the figure. However, the average density is large enough that slightly over-dense cells can still move into the super-Alfvénic regime, indicating that turbulent damping will still influence the global wind.

Figure 3.1 also illustrates the drastic effect that M_A has on the CR streaming speed in the galaxy. The black line in the figure denotes the line at $M_A = 1.0$, where the turbulent damping formulae from *Lazarian* (2016) are equivalent to the *Farmer and Goldreich* (2004) damping formula for strong turbulence. The streaming speed at $M_A = 1.0$ given fixed $n_i, n_{\rm cr}$ and B is always higher than the streaming speed for

sub-Alfvenic turbulence as σ decreases and other parameters are fixed. For example, on the $M_A = 1$ line at $\sigma = 5$ km/s, the *Farmer and Goldreich* (2004) formula predicts a streaming speed boost $\log(f-1)$ greater than 0.5, in the regime where turbulent damping is effective. If M_A decreases, by lowering the velocity dispersion to $\sigma = 1$ km/s, at the same density, the streaming speed is essentially Alfvénic with $\log(f-1)$ below a value of -1, where turbulent damping is not effective. All in all, not accounting for a decrease in M_A results in an overestimation of the streaming speed. This effect is greater as M_A decreases due to the steep dependence of the damping rates (and thus the streaming speed) on M_A, as shown in Table 3.2. Such a decrease will change the average profile of streaming speed with height above the midplane in Figure 3.5. Furthermore, if the CR streaming speeds are different, the overall wind will be different, as will be shown in the subsequent part of the discussion regarding Figure 3.6.

Further comparisons we discuss here are between the Alfvénic and stronger turbulence ($\sigma = 10$ km/s) cases, as the weaker strength turbulence results follow similar trends to that of the stronger turbulence. Figure 3.2 shows a qualitative comparison between the Alfvénic streaming and streaming with turbulent damping simulations in ion and CR density slices at a snapshot of 200 Myr, when the SFR and wind settles down. Figure 3.3 shows the volume-weighted profiles of ion and CR density versus height above the mid-plane for the Alfvénic case, as well as the profiles for streaming with turbulent damping relative to the Alfvénic one. These profiles are volume-weighted to provide a fair comparison between the slice images and the averaged ion and CR densities. At 200 Myr there is a systematically more extended ion and CR distribution in the local turbulent damping case compared to the Alfvénic case. The slices show that the ion and CR densities is higher in the mid-plane for local streaming. There is also a noticeable increase in the ion and CR densities farther away from the mid-plane at the top of the figure ($|z| = 5$ kpc). The far right column

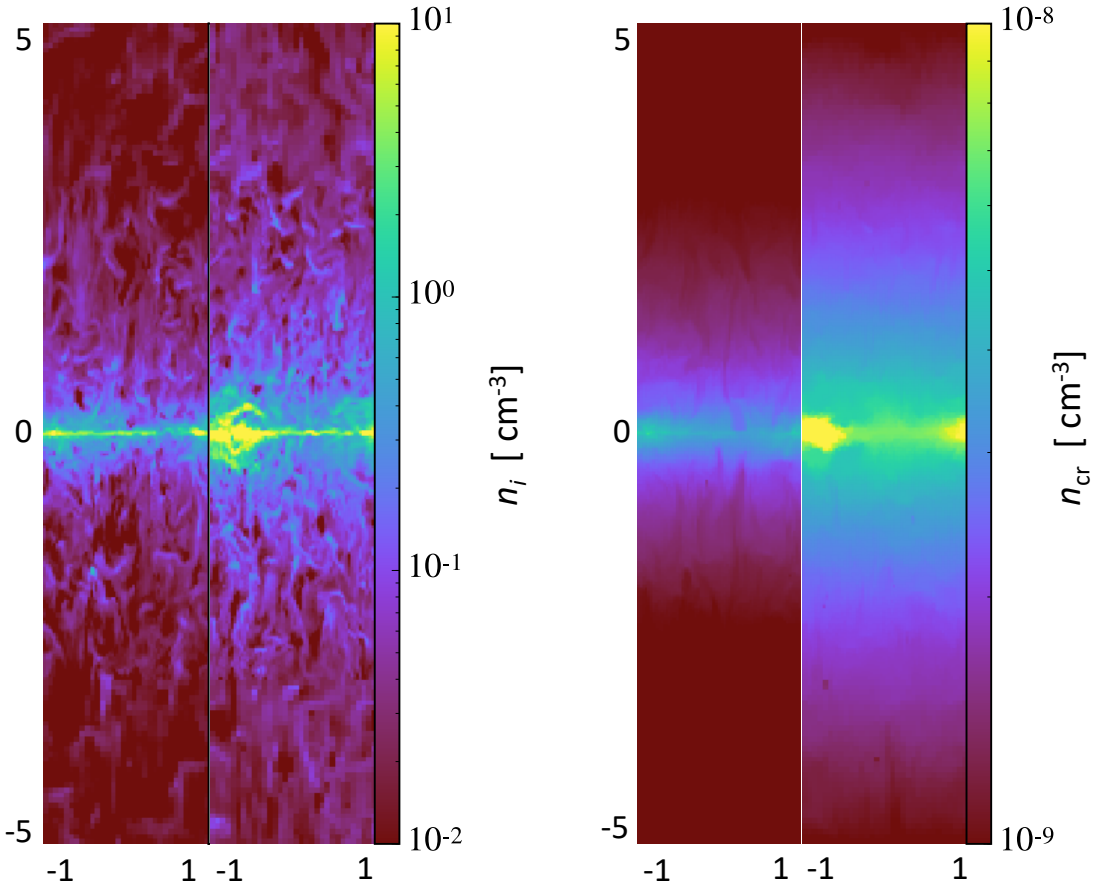

Figure 3.2: Ion and CR number density slice of dimensions ±5 kpc along z direction perpendicular to the midplane, for two simulations at 200 Myr: Alfvénic streaming and streaming including turbulent damping ($\sigma = 10$ km/s). The Alfvénic simulation results are on the left hand side of each pair of plots, and the turbulent damping simulations are on the right side of each pair. The gas distribution (left pair) is slightly more extended in the turbulent damping simulation than for the Alfvénic streaming simulation. Similarly, the CR distribution (right pair) is significantly more extended in the turbulent damping simulation.

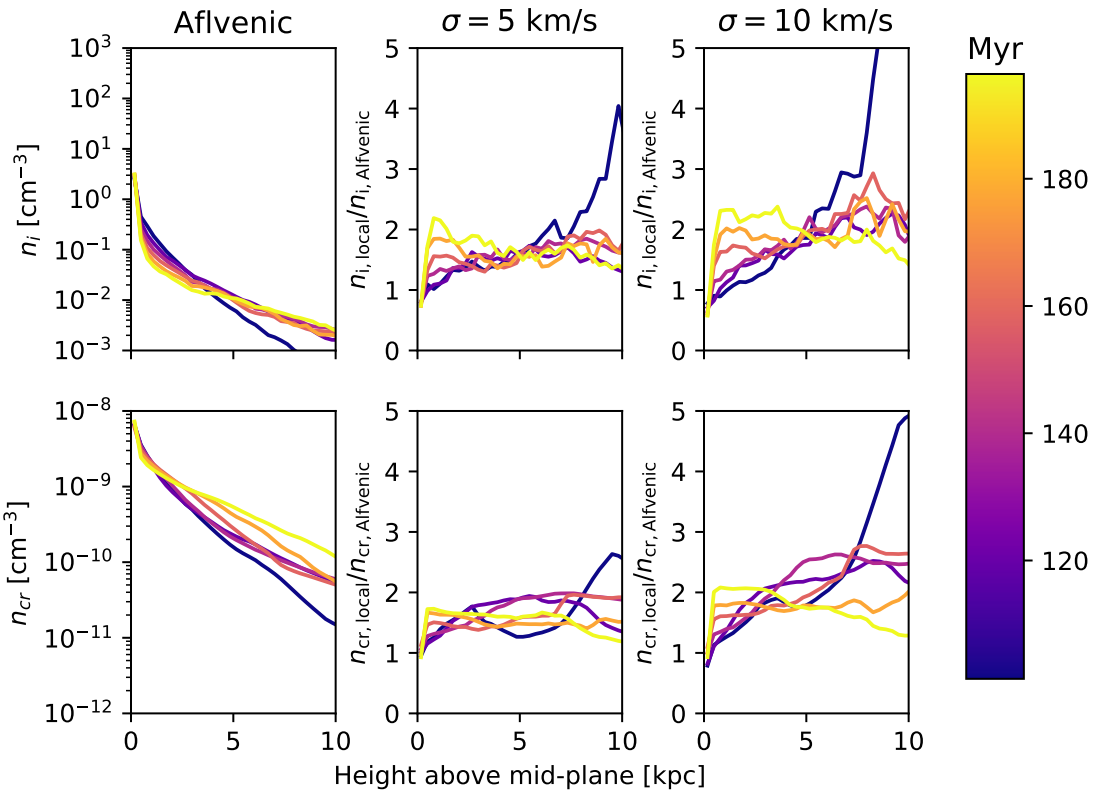

Figure 3.3: Ion and CR number density volume-weighted profiles up to 200 Myr. Left column: Alfvénic streaming. Middle and Right columns: Profiles of the ratio of number densities found in different CR streaming simulations, turbulent damping for two strengths of turbulence, and the Alfvénic streaming. The ratio is systematically greater than one for most of the evolution.

of Figure 3.3 quantifies these observations with relative profiles of ion and CR density. The general shape of the ion and CR density profiles with height is similar between simulations with Alfvénic streaming and those with damped streaming, as the relative density profile at later times in the simulation are roughly a constant factor different. The simulations with turbulent damping, however, have a systematically higher ion and CR density profile values at a given height compared with the Alfvénic streaming simulation. Within 5 kpc of the mid-plane, the average number density of both ions and CRs is about twice as large at a given height compared to the Aflénic streaming simulation. Additionally, at the mid-plane the CR number density profile approaches that of the Alfvénic streaming simulation. These results are due to the enhanced CR streaming near the mid-plane. With a boost in streaming, there is enhanced feedback–CRs can more effectively leave the dense mid-plane, allowing interaction with more tenuous gas and providing less pressure support against self-gravity of the midplane gas. This leads to an increased SFR.

In addition to denser gas on average, simulations with faster CR streaming also display differences in the relative clumping of the gas, which we quantify using the clumping factor

$$C_p = \frac{<\rho^2>}{<\rho>^2}, \tag{3.14}$$

where the averages are volume-weighted, as *Girichidis et al.* (2018) calculates with simulations of a similar geometry as ours. Figure 3.4 compares the average value of C_p between simulations with Alfvénic CR streaming and the strongest turbulent damping case, within three regions: near the midplane ($|z| < 0.1$ kpc), intermediate height above the midplane (0.1 kpc $< |z| <$ 1 kpc), and the lower halo (1 kpc $< |z| <$ 2 kpc). Near the midplane, C_p remains relatively constant throughout both of the simulations, with $C_p \approx 5 - 8$ in the Alfvénic streaming case and $C_p \approx 11 - 15$ for the turbulent damping case. The increased clumping in the turbulent damping case is consistent with the decreased stability in dense gas mentioned previously, as

CRs more easily leave the midplane and the CR pressure support is reduced. In the intermediate height region, C_p shows a strong temporal evolution in the Alvénic streaming simulation, starting relatively smooth with $C_p \approx 2$ and eventually reaching $C_p \approx 10$. The gas in this region is structured by supernovae (*Girichidis et al.*, 2018), consistent with the increased star formation rate (Figure 3.6) and clumping of gas with time. This increased clumping contrasts with the turbulent damping simulation, where C_p begins at the same value as in the Alfvénic streaming simulation, and remains around $C_p \sim 2$ for the entire duration. The suppression of C_p is due to the increased average density in this region relative to the Alfvénic streaming case (Figure 3.3), and that it is more difficult for supernovae to structure denser gas. In the lower halo up to 2 kpc in height, the gas remains consistently smooth in both simulations.

The boost in streaming speed is seen in the mass-weighted profile of CR streaming speed shown in Figure 3.5, where the stronger turbulence case is shown in blue. The profile is mass-weighted because we are interested in the influence that CRs have in accelerating gas. Near the mid-plane the boost factor f is large and remains above $f = 2$ within the thin galactic disk ($|z| < 500$ pc), and weakly super-Alfvénic at larger heights as turbulent damping becomes ineffective.

Since we do not track the CR spectrum or include energy dependent processes in our simulations, we cannot make predictions about observational signatures (e.g., synchrotron emission) produced by CRs. Generally, a CR distribution more extended in height above the mid-plane does result in stronger radio emission in the halo around a galaxy (*Wiegert et al.*, 2015). CR feedback could also influence the radio luminosity through its affect on the SFR (e.g. *Li et al.*, 2016). Observational signatures derived from simulations with modeling of the CR spectrum (*Yang and Ruszkowski*, 2017) will be investigated in future work.

The trends for the weaker turbulence strength follow those described for stronger turbulence, although, as expected, they are closer to the Alfvénic streaming results,

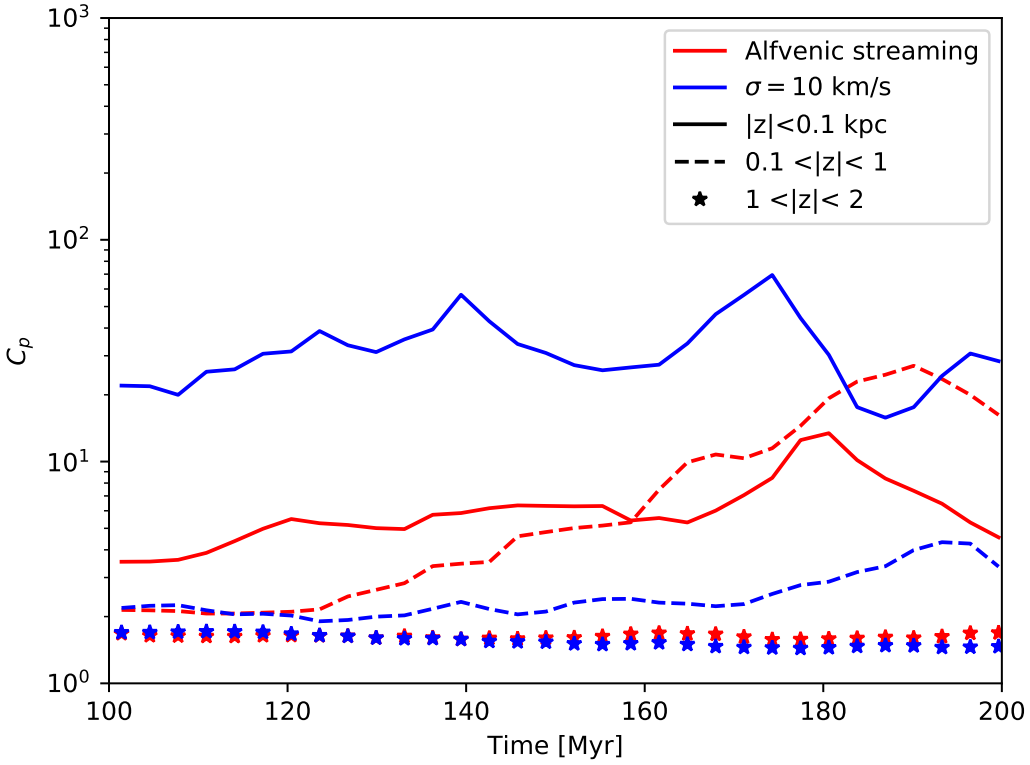

Figure 3.4: Clumping factor of density C_p for two simulations, Alfvénic (red) streaming and turbulent damping with $\sigma = 10$ km/s (blue), in three separate regions around the midplane. We focus on the second half of the simulation, from beginning of the wind at 100 Myr and the end of the simulation at 200 Myr. Close to the midplane ($|z| < 0.1$ kpc), clumping is relatively constant for both simulations, but there is stronger clumping for faster CR transport. In the intermediate region (0.1 kpc $< |z| < 1$ kpc), faster CR transport suppresses temporal changes in the clumping factor, leading to low values clumping. Farther out from the midplane (1 kpc $< |z| <$ 2 kpc), clumping is low for both simulations.

due to the corresponding reduction in the strength of turbulence. Halving the velocity dispersion produces a significant reduction in streaming speed. For example, $f - 1 \propto \sigma^2$ for strong, sub-Alfvénic turbulence, so halving σ will reduce average streaming by a factor of four. Figure 3.5 shows that both cases have high CR average streaming near the mid-plane and weakly super-Alfvénic streaming at larger heights, with the weaker turbulence run having a systematically smaller f values.

The transition from no CR transport to progressively faster CR transport is seen in Figure 3.6. The figure shows a comparison for the SFR, mass outflow, and mass loading of five simulations: from left to right they are, 'No transport' where $f = 0$, 'Alfvénic' where $f = 1$, and finally three simulations with different turbulence strengths, two with constant velocity dispersion, and one with constant $M_A = 1$. The mass flux and integrated mass flux are calculated across two different surfaces (2.5 and 5.0 kpc) above the midplane. The SFR plots include the result of a simulation without CRs. This case can also be thought of as the limiting case for maximal CR transport or equivalently no confinement of CRs.

For times up to 50 Myr, the simulations appear similar as there has not been significant and sustained CR production. After 70 Myr, there are enough CRs to influence feedback and the SFR profiles diverge. In the simulation without CRs, gas cools and collapses more easily to form stars due to the absence of CR pressure. For our specific implementation, this stellar feedback fails to launch a significant wind. The result is a comparatively greater peak SFR than in the other simulations with CRs. After the bulk of stellar particles form, the SFR in all of the simulations reaches an equilibrium around 0.5 $M_\odot$/yr, agreeing with the expected SFR of approximately 0.5 $M_\odot$/yr for a gas surface density of 80 $M_\odot/\mathrm{pc}^2$ (*Kennicutt Jr*, 1998).

In the case where there are CRs injected by feedback, but no streaming (i.e., $f = 0$), CRs are transported by advection with the gas. CRs cannot escape the mid-plane effectively, halting further cold gas gravitational collapse through additional

pressure support that is not radiated away, unlike that of the gas. The first column of Figure 3.6 shows the SFR and wind properties for a simulation with the CR transport being solely advection. There is a weak galactic wind, low SFR, and puffed-up disk morphology. These results agree with other works (see *Salem and Bryan*, 2014; *Girichidis et al.*, 2016; *Simpson et al.*, 2016; *Ruszkowski et al.*, 2017; *Farber et al.*, 2018).

When CR transport is added, CRs can escape the dense disk, influencing the evolution of the simulation. *Ruszkowski et al.* (2017) included comparisons between no CR transport ($f = 0$) and Alfvénic CR transport ($f = 1$), finding an increased SFR and stronger wind in the Alfvénic streaming case. They find the same trend of an increasing and more sustained SFR with progressively faster CR streaming, up to $f = 8$ or 8 times the Alfvén speed. Our simulations agree with this trend as the SFR increases for stronger turbulence, which leads to faster CR transport in our simulations. Our simulations extend their treatment of CR physics by allowing for spatial and temporal variations in the CR transport speed. The higher streaming speed in the ISM allows CRs to escape the dense mid-plane, allowing for further gas collapse. Indeed, as the velocity dispersion increases, the SFR increases and approaches the peak SFR of a simulation without CRs. The differences in time evolution of the outward mass flux (bottom row in Figure 3.6) are weaker for increasing CR transport. The peak mass flux is similar for the simulations of Aflvénic streaming and both simulations with constant velocity dispersion; however, the mass flux does increase when turbulent damping is included in CR transport.

Furthermore, the results in Figure 3.6 confirm the idea, motivated by Figure 3.1, that accounting for the M_A dependence of the damping formulae is essential. The fifth column of the figure shows the results for a simulation with constant $M_A = 1$ in the damping formulae. For sub-Alfvénic turbulence as is found in the wind launching region, at $M_A = 1$ the CR streaming speed is higher at a given n_i, $n_{\rm cr}$, and B

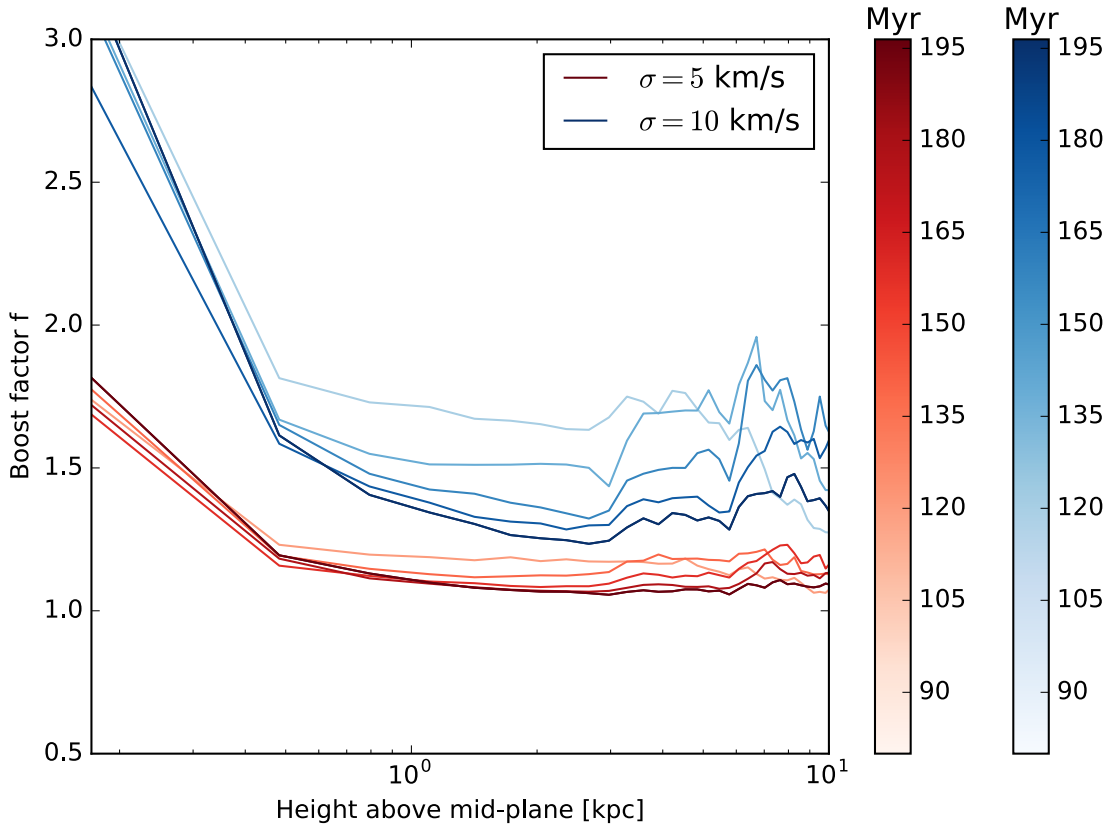

Figure 3.5: Mass-weighted CR streaming speed parameter f for local streaming with $\sigma = 5$ km/s (red) and $\sigma = 10$ km/s (blue). The profile in the streaming speed boost factor f is systematically higher for the stronger turbulence case, but both profiles approach near-Alfvénic streaming values away from the midplane.

compared to the case where the velocity dispersion is constant. At a given n_i and B, u_A is constant, so the velocity dispersion is a factor of M_A different (smaller, for $M_A < 1$) than the equivalent value at $M_A = 1$. Correspondingly, the peak SFR is greater in the $M_A = 1$ case compared to the stronger velocity dispersion case of $\sigma = 10$ km/s, as CRs leave the midplane more quickly and allow more stars to form. The peak mass flux is also much greater for the fifth simulation.

The increase in the SFR has a significant impact on instantaneous mass loading (ratio of the outward mass flux $\dot{m}_w$ to the SFR), seen in the top row of Figure 3.6. We find that the instantaneous mass loading is almost an order of magnitude smaller for

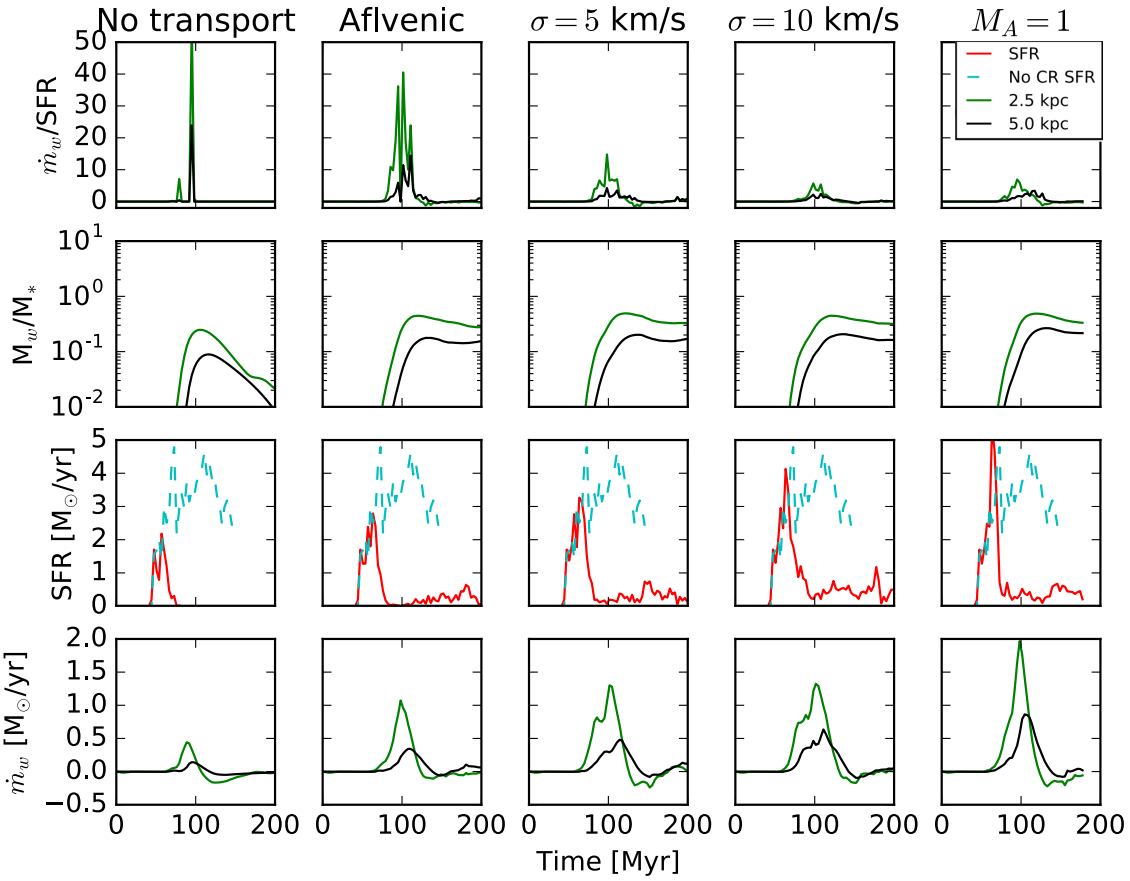

Figure 3.6: Comparison of instantaneous mass loading (top row) through two surfaces above the mid-plane, integrated mass loading (second row), SFR (third row) and mass outflow (fourth row), between five different CR streaming implementations. The first column shows results from a simulation without CR transport, the second column shows results from simulations with Alfvénic streaming ($f = 1$), while the third and fourth show results from simulations with streaming including turbulent damping ($f = f(n_i, n_{\rm cr}, B, \sigma = 5$ km/s) and $f = f(n_i, n_{\rm cr}, B, \sigma = 10$ km/s) respectively), and fifth column shows results for constant $M_A = 1$, where the damping rates from 3.2 equal those from *Farmer and Goldreich* (2004).

the stronger turbulence simulation compared to Alfvénic streaming. This is because for stronger turbulence, CR transport is faster and the SFR is larger. This fact, combined with weaker sensitivity of the mass flux to CR transport speed, makes the instantaneous mass loading a decreasing function of the velocity dispersion. We plot the mass loading through two surfaces 2.5 kpc and 5 kpc above the mid-plane, finding similar trends. For the Alfvénic CR streaming simulation, the mass loading peaks at a value of about 40, while for the stronger turbulence simulation, it peaks at about 5. These values are consistent with observational constraints, which constrain instantaneous mass loading in range 10^{-2} and 10^{1} (*Bland-Hawthorn et al.*, 2007). For example, *Newman et al.* (2012) use optical emission lines from a sample of galaxies and find mass loading factors of around 0.2-1 for the SFR surface density in our simulations. Furthermore, in our simulations we only studied a single halo mass, a MW-like halo, rather than a variety of halo masses. However, we expect that the feedback effects would be stronger for lower mass halos, and should follow trends similar to those we described above. *Jacob et al.* (2018) studied a set of isolated galaxies (although CR transport was modeled with diffusion, rather than streaming as in this work) with halo masses ranging from $10^{10} M_{\odot}$ to $10^{13} M_{\odot}$ and found that mass loading scales like M_{200}^{n}, with $-2 < n < -1$, so lower mass halos have larger mass loading. Mass loading values exceeding 10, as we find in the Alfvénic CR streaming case, can be suppressed by the presence of turbulence, landing within the observational constraints, as shown in the mass loading of the stronger turbulence simulation.

On the other hand, we find that the integrated mass loading (ratio of the total wind mass $M_w = \int_0^{200\mathrm{Myr}} \dot{m}_w \, \mathrm{d}t$ to the stellar mass M_*), is almost insensitive to the parameters we considered. The values we find for the integrated mass loading are about 0.2-0.3, roughly consistent with values from isolated slab simulations (e.g., *Farber et al.*, 2018) and also global simulations (e.g., *Ruszkowski et al.*, 2017). While

Ruszkowski et al. (2017) found that the integrated mass loading increased with faster CR streaming, their simulations were global.

3.5.1 Other Relevant Physical Processes

Our simulations do not account for various aspects of CR transport and CR interaction with the gas.

1. We focus on the streaming model of CR transport. CR transport is also modeled with diffusion (e.g. *Salem and Bryan*, 2014; *Girichidis et al.*, 2016; *Simpson et al.*, 2016), with parallel and perpendicular diffusion coefficients with respect to the magnetic field, usually taken to be constant in space and time. Unlike in the streaming model, CRs do not heat the gas. *Wiener et al.* (2017b) compared simulations with either the diffusion or streaming model of CR transport and found that galactic winds are weaker with streaming compared to diffusion. However, they did not include magnetic fields in their simulations, using the sound speed instead of the Alfvén speed for the streaming speed. The question of which model more accurately describes CR transport in the galaxy and halo remains without a definitive answer.

2. We do not include additional Alfvén wave damping processes such as ion-neutral damping and non-linear Landau damping. As ion-neutral damping is important when the medium that the CRs pass through is not completely ionized. The effects of ion-neutral damping on the galactic wind have been studied recently by *Farber et al.* (2018). Non-linear Landau damping occurs due to wave-particle interactions (*Kulsrud*, 2005). It is expected that this damping will not be dominant in astrophysical settings because it is self-regulating (see *Lazarian*, 2016).

3. Our implementation of turbulent damping of Alfvén waves from *Lazarian* (2016),

while still dependent on the local properties of the ISM and halo, is not completely self-consistent. First, we assumed a constant gas velocity dispersion in the turbulent damping rates, which strictly speaking is not true as turbulence will decay farther away from the star forming regions. However, this assumption is sufficient in our case because the properties of the launching region (close to the mid-plane) should determine the properties of the overall wind. Despite this assumption, the turbulent Alfvén Mach number (velocity dispersion divided by the Alfvén speed) nevertheless decays with height above the mid-plane as expected because the Alfvén speed increases with height. The streaming speed profile in Figure 3.5 also decays with height as expected, approaching Alfvénic streaming in the halo. However, the assumption of constant velocity dispersion does not allow us to study in detail the different regimes of turbulence presented in *Lazarian* (2016), as the halo turbulence strength (i.e. away from the wind launching zone) will be significantly overestimated. Second, we do not account for the level of ionization in the ISM and halo gas in determining the CR streaming speed. Only the ionized gas will participate in the growth and damping of Alfvén waves. However, since the ISM and halo are significantly ionized, especially in the wind launching region just above the dense mid-plane, we did not specifically estimate the level of ionization in the gas and assume that the gas is fully ionized.

4. We also do not account for energy-dependent processes. The CR streaming speed boost $f - 1$ increases with energy (or $\gamma_{\rm rel}$), so higher energy CRs will escape faster. In a simple picture, we might expect that the CR spectrum will steepen from the initial spectrum. Furthermore, we do not account for loss of energy by CRs, due to hadronic losses as well as Coulomb losses, where CRs interact inelastically with atoms in the ISM.

5. There are also additional feedback mechanisms we did not implement. One example is the mechanism based on the radiation pressure from massive stars onto ISM dust in driving a galactic wind (*Hopkins et al.*, 2012; *Zhang and Thompson*, 2012). Including this mechanism involves calculating the radiation field using radiative transfer models, and including components of the ISM that interact with the field, such as dust, and is beyond the scope of this paper.

6. Finally, CR propagation depends on the details of the MHD turbulent cascade. In our model, we assume that turbulence only interacts with the CR-generated Alfvén waves and not the CRs themselves. In the extrinsic turbulence picture, turbulence scatters CRs as they propagate through the ISM with fast modes identified as the major agent of CR scattering (*Yan and Lazarian*, 2002). A realistic magnetic topology is also important since CRs gyrate and follow the magnetic field and can also diffuse across field lines, potentially even super-diffusively (i.e., *Lazarian and Yan*, 2014). We expect the galactic winds to be mostly sub-Alfvénic with the magnetic field not being strongly tangled, so the Alfvénic perturbations arising from galactic-scale turbulence will not scatter CRs efficiently (*Yan and Lazarian*, 2002, 2004, 2008). Instead, the Transient-Time damping (TTD) processes (see *Xu and Lazarian*, 2018) dominates the effect interactions of CRs with galactic-scale turbulence cascade. Overall, all of these processes interact in a non-linear fashion over a large range of scales, so a more complete description of CR transport in a galaxy remains to be fully understood.

3.6 Conclusions

We perform three-dimensional magnetohydrodynamical simulations of a section of a galactic disk considering the impact of locally-determined cosmic ray (CR) trans-

port on the properties of galactic winds. CR transport is treated within the self-confinement model, where the balance between wave growth and its decay by turbulent damping of self-excited Alfvén waves determines the bulk CR streaming speed relative to the gas. We employ the model of the streaming instability damping in *Lazarian* (2016) and find that the coupling of CRs experience significant spatial variations. Due to turbulent damping, the CRs are weakly coupled within the regions of the interstellar medium with higher level of sub-Alfvenic turbulence. We compared simulations with and without turbulent damping of the CR streaming instability. Our conclusions are as follows:

1. We find that the star formation rate (SFR) increases when turbulent damping is included in the CR transport model and continues to increase with the strength of turbulence. Stronger turbulence damps confining Alfvén waves and leads to a corresponding boost in the average CR streaming speed. As the CRs can leave the dense mid-plane more easily, the reduced pressure support from CRs allows gas to collapse and form stars more effectively.

2. We show that the cumulative mass loading factor, the ratio of integrated wind mass to cumulative stellar mass, is insensitive to the impact of turbulent damping on the CR streaming speed. For both strengths of turbulence tested, the cumulative mass loading factor asymptotes to the same value as the Alfvénic streaming run.

3. We show that the instantaneous mass loading is very sensitive to increased CR streaming speed due to turbulent damping.

4. We demonstrate that the increased CR streaming speed due to turbulence results in more extended gas and CR density distributions. The larger SFR results in more stellar feedback, directly increasing the number of CRs produced in the

mid-plane. These CRs escape the dense mid-plane more quickly with an increased streaming speed, widening the CR distribution in height. Escaping the central regions allows CRs to interact with lower density gas, which is easier to accelerate into the galactic wind, widening the gas distribution in height.

CHAPTER IV

Effect of Cosmic Rays and Ionizing Radiation on Observational Ultraviolet Plasma Diagnostics in the Circumgalatic Medium

4.1 Preface

For this chapter, I am the lead author, and it is coauthored by R. Farber and M. Ruszkowski. This work is in preparation to be submitted to MNRAS.

4.2 Abstract

Computational models of galaxies have included increasingly more detailed feedback mechanisms, successfully reproducing a variety of galaxy properties. Nonetheless, the relevance of some feedback mechanisms, in particular cosmic ray feedback, has been challenging to definitively describe in a galactic context, especially far outside the galaxy in the circumgalactic medium (CGM). At the same time, the uncertainty in ionization mechanisms in CGM, such as the role of the stellar radiation field, prevent conclusive interpretations of multiphase CGM properties derived from ultraviolet (UV) diagnostics. We conduct three dimensional magnetohydrodynamic simulations of a section of a galactic disk, including radiative heating and cosmic

ray feedback. We post-process them in a parallel-plane approximation, including the galactic radiation field, in order to derive spatially and temporally varying synthetic UV diagnostics. We find that radiative effects alone are not able to produce synthetic diagnostics that match observed ranges. For low cosmic ray diffusivity $\kappa_{\rm cr} = 10^{28}$ cm^{2}s^{-1}, the model cosmic ray streaming heating produces diagnostics around observed ranges, in the regions affected by an outflow. Losses from collisionless heating from cosmic ray streaming are significant enough that galactic outflows are weakened. The model most favored by UV diagnostics is the one that includes higher cosmic ray diffusivity $\kappa_{\rm cr} = 10^{29}$ cm^{2}s^{-1} and radiative heating, while lacking cosmic ray streaming heating. Our work demonstrates UV plasma diagnostics have potential use as a tool for differentiating between cosmic ray feedback models.

4.3 Introduction

Simulations of the galactic and cosmological environment have greatly improved over the last decade. More detailed models of stellar and radiative feedback, along with increased computational power, have allowed modern three dimensional galactic (e.g., *Guedes et al.*, 2011; *Hopkins et al.*, 2012; *Rosdahl et al.*, 2013) and full cosmological-scale (e.g., *Vogelsberger et al.*, 2014; *Pillepich et al.*, 2018) models to reproduce many global properties observed in real galaxies, such as the efficiency of stellar feedback for sub-Milky Way and Milky Way mass halos (*Hopkins et al.*, 2012), SFR variability (*Orr et al.*, 2017; *Sparre et al.*, 2017), or gas velocity dispersion (e.g. *Orr et al.*, 2020). Previously neglected processes have also been implemented, such as turbulence (*Schmidt et al.*, 2014), magnetohydrodynamics (MHD) (e.g. *Wang and Abel*, 2009; *Dolag and Stasyszyn*, 2009; *Hopkins et al.*, 2018), cosmic rays (CRs) (e.g. *Booth et al.*, 2013; *Hopkins et al.*, 2020), and radiative feedback (*Rosdahl et al.*, 2013; *Kannan et al.*, 2022; *Katz*, 2022). These galactic simulations facilitate better interpretations of astronomical measurements from real galaxies as they are a

'universe-in-a-box' allowing us to isolate and closely examine the effects of individual physical processes.

Here we focus on Milky way-like galaxies, where stellar feedback (including cosmic rays) is likely to play a role in galactic evolution (i.e., *Hopkins et al.*, 2012, 2014). Radiation and CR phenomena are similar in that small-scale physics, much below the resolution scale of a galactic simulation, plays a key role in global transport. For example, two opposing limits–the free-streaming and diffusive limits–must be adequately modeled (e.g., *Hopkins et al.*, 2022a). The stellar radiation field likely extends well past the galactic disk and into the inner CGM up to roughly 0.1-0.2 $R_{\rm vir}$ for Milky Way-like, low redshift galaxies (*Holguin et al.*, 2022b). Therefore, it is important to consider the influence of this spatially and temporally varying field on the ionization state in the inner CGM. Three dimensional radiative transfer is incredibly computationally expensive as the radiation field acts non-locally.

CR physics is challenging to model as there are large uncertainties in the underlying assumptions about the interaction of CR and the magnetized environment. CRs are known to have a galactic confinement time much larger than the free streaming time and their arrival distribution measured at the Earth for Tev-PeV cosmic rays is measured to be isotropic to 10^{-4} (*Nagashima et al.*, 1998). CR confinement is primarily described by two ideas, extrinsic turbulence and self-confinement (see *Zweibel*, 2013). Within both of these descriptions, many models have been theorized and even implemented in galactic simulations (see *Zweibel*, 2013, 2017; *Thomas and Pfrommer*, 2019). However, distinguishing between these models based on observational evidence of CRs, such as the total column density of matter traversed by CRs ('grammage') (*Strong et al.*, 2007), radio synchrotron (e.g., the CHANG-ES radio halo survey *Irwin et al.* 2012) or gamma-rays (e.g., *Ackermann et al.*, 2012) has been difficult. *Hopkins et al.* (2021d) compares a wide range of CR transport parameters in dwarf and MW-type galaxy simulations and identifies a set of models that

are consistent with observational evidence. These allowed models of CR transport, including more physically motivated ones, still have significant uncertainties. They require some fine-tuning, tend to produce similar effects on galaxy and inner-CGM (¡10 kpc) properties, and are not well-constrained observationally farther out into the CGM (*Hopkins et al.*, 2021b). These models are also problematic with regards to constraints from the CR spectrum (*Hopkins et al.*, 2021c). The unresolved tension in CR transport motivates the introduction of additional constraints.

Ultraviolet (UV) ion diagnostics contain a wealth of information about the plasma state of the CGM from the cold, neutral medium to the hot, ionized galactic corona (see *Tumlinson et al.*, 2017, and references therein). These diagnostics have highlighted the CGM as a significant reservoir of baryons existing in a multiphase medium. The exact properties of the plasma that produces some of these observed diagnostics is uncertain, as modeling often requires assumptions about the local ionization equilibrium. For example, similar diagnostic signals can occur from collisionally ionized $T \sim 10^5$ K and photoionized $T \sim 10^4$ K plasmas. In addition to the radiation field, CRs can also influence the properties of the multiphase plasma (e.g. *Ji et al.*, 2020; *Butsky et al.*, 2020), potentially affecting these diagnostics. Galactic computational simulations can aid in untangling these degeneracies, especially with the continuously improving CR feedback models constrained by other methods.

Our goal is to provide a proof-of-concept for constraining simulation results using CGM UV diagnostics. In Section 4.5 we describe results from updated parallel-plane elongated slab simulations from (*Holguin et al.*, 2019) with simplified radiative heating, improved supernova (SN) feedback, and CR collisional losses. In these six simulations, we explore several limiting cases in the parameter space of CR and radiation heating feedback. In Section 4.6 we describe a parallel-plane post-processing approximation, including the stellar and metagalactic radiation field, that can estimate the ionization state of the plasma throughout the domain. We also examine theoreti-

cal expectations for CR and radiation feedback effects on UV diagnostics tracing gas phases between $T = 10^4$ K and $T = 10^6$ K. In Sections 4.7 and 4.8, we describe resulting synthetic diagnostic predictions and broadly compare them to typical observed values. Finally, in Section 4.9 we provide concluding remarks.

4.4 MHD Simulation Methods

The simulations we run are similar to those from *Holguin et al.* (2019), with updated stellar feedback methods and additional radiative heating and CR loss models. The simulations are run with the adaptive mesh refinement MHD code FLASH 4.2 (*Fryxell et al.*, 2000; *Dubey et al.*, 2008) using a directionally unsplit staggered mesh solver (*Lee and Deane*, 2009; *Lee*, 2013), including CR transport physics (*Yang et al.*, 2012; *Ruszkowski et al.*, 2017; *Farber et al.*, 2018) in an elongated box geometry with dimensions $2 \times 2 \times 40$ kpc^3. We solve a coupled MHD-CR two-fluid model (*Salem and Bryan*, 2014; *Ruszkowski et al.*, 2017) composed of thermal gas and ultrarelativistic CR fluid with adiabatic indices $\gamma = 5/3$ and $\gamma_{\rm cr} = 4/3$ respectively. The CR fluid represents a single energy channel of typical galactic CRs with mean CR Lorentz factor $\gamma_{\rm rel} = 3$ and momentum distribution slope $n = 4.5$. Both hadronic and Coulomb CR losses are included (*Guo and Oh*, 2008). CR transport includes advection, dynamical coupling with gas, and streaming along magnetic field lines relative to the thermal gas. Heating of the gas occurs due to radiative heating from both non-ionizing and ionizing UV stellar spectrum, CR streaming and hadronic losses, and supernova feedback. Cooling of gas occurs via radiative cooling. Gas dynamics is impacted by self-gravity, stellar momentum feedback, and dynamical coupling with CRs. Star formation occurs according to established criteria, resulting in the creation of a stellar population particle and equal mass loss of gas. The following equations summarize the model:

$$\frac{\partial \rho}{\partial t} + \boldsymbol{\nabla} \cdot (\rho \boldsymbol{u}_g) = -\dot{m}_{\rm form} + f_* \dot{m}_{\rm feed} \tag{4.1}$$

$$\frac{\partial \rho \boldsymbol{u}_g}{\partial t} + \boldsymbol{\nabla} \cdot \left(\rho \boldsymbol{u}_g \boldsymbol{u}_g - \frac{\boldsymbol{B}\boldsymbol{B}}{4\pi} \right) + \boldsymbol{\nabla} p_{\rm tot} = \rho \boldsymbol{g} + \dot{p}_{\rm SN} \tag{4.2}$$

$$\frac{\partial \boldsymbol{B}}{\partial t} - \boldsymbol{\nabla} \times (\boldsymbol{u}_g \times \boldsymbol{B}) = 0 \tag{4.3}$$

$$\begin{aligned} \frac{\partial e}{\partial t} + \boldsymbol{\nabla} \cdot \left[(e + p_{\rm tot}) \boldsymbol{u}_g - \frac{\boldsymbol{B}(\boldsymbol{B} \cdot \boldsymbol{u}_g)}{4\pi} \right] &= \rho \boldsymbol{u}_g \cdot \boldsymbol{g} \\ - \nabla \cdot \boldsymbol{F}_{\rm cr} - C + H_{\rm SN} + H_{\rm rad} + \Gamma_{\rm cr,gas} & \end{aligned} \tag{4.4}$$

$$\begin{aligned} \frac{\partial e_{\rm cr}}{\partial t} + \boldsymbol{\nabla} \cdot (e_{\rm cr} \boldsymbol{u}_g) = & - p_{\rm cr} \nabla \cdot \boldsymbol{u}_g - H_{\rm cr} + \Gamma_{\rm cr} + H_{\rm SN} \\ & - \nabla \cdot (\boldsymbol{\kappa}_{\rm cr} \cdot \nabla e_{\rm cr}) \end{aligned} \tag{4.5}$$

$$\Delta \phi = 4\pi G \rho_b \tag{4.6}$$

where ρ is the gas density, ρ_b is the total baryon density including both the gas and stars, $\dot{m}_{\rm form}$ is the density sink from stellar population particle formation, $f_* \dot{m}_{\rm feed}$ represents the gas density source from stellar feedback (see Section 4.4.2), $\boldsymbol{u}_g$ is the gas velocity, $\boldsymbol{B}$ is the magnetic field, G is the gravitational constant, ϕ is the gas gravitational potential, $\boldsymbol{g} = -\boldsymbol{\nabla}\phi + \boldsymbol{g}_{\rm NFW}$ is the gravitational acceleration (the sum of gas self-gravity, stellar particle, and halo dark matter contributions to the gravitational acceleration, described in Section 4.4.1) where $\boldsymbol{g}_{\rm NFW}$ is the gravity from the Navarro-Frenk-White (NFW) potential, $p_{\rm tot}$ is the sum of gas ($p_{\rm th}$), magnetic, and

CR ($p_{\rm cr}$) pressures, $\dot{p}_{\rm SN}$ is the momentum injection due to stellar winds and SNe. Furthermore, $e = \rho \boldsymbol{u}_g^2 + e_g + e_{\rm cr} + B^2/8\pi$ is the total energy density per volume (the sum of gas, CR, and magnetic components, respectively), C is the radiative cooling rate per unit volume, $H_{\rm rad}$ is the radiative heating rate per unit volume, $\Gamma_{\rm cr}$ is the CR energy loss rate per unit volume, $\Gamma_{\rm cr,gas}$ is the energy rate gained by the gas from the CR losses, $\kappa_{\rm cr}$ is the CR diffusion coefficient, and $H_{\rm SN}$ is the supernova heating rate per volume.

4.4.1 Gravity

The gravitational acceleration has three components: baryons, stellar particles, and the dark matter halo. Self-gravity from baryons is computed by solving the Poisson equation with the Barnes-Hut tree solver (*Barnes and Hut*, 1986), which is implemend in FLASH by *Wunsch et al.* (2018). For the dark matter halo gravity modeled as an NFW potential (*Navarro et al.*, 1997), we include the vertical component of gravity as the domain is thin and much smaller than the halo. The halo gravitational acceleration is

$$g_{\rm NFW}(z) = -\frac{GM_{200}}{|z|^3} \frac{\ln(1+x) - x/(1+x)}{\ln(1+c) - c/(1+c)} \tag{4.7}$$

where G is the gravitational constant, M_{200} is the halo virial mass, z is the height above the mid-plane, $x = |z|c/r_{200}$, c is the halo concentration parameter, and r_{200} is the virial radius. Table 4.1 summarizes our choices of these parameters.

4.4.2 Star formation and supernova feedback

Following the approach of *Cen and Ostriker* (1992) (see also *Tasker and Bryan* 2006; *Bryan et al.* 2014; *Salem and Bryan* 2014; *Li et al.* 2015), the creation of a stellar population particles occurs when all of the following conditions are instantenously met: (i) gas number density exceeds 10 cm^{-3} (*Gnedin and Kravtsov*, 2011; *Agertz*

et al., 2013); (ii) the cell mass exceeds the local Jeans mass; (iii) the divergence of the gas velocity $\boldsymbol{u}_g$ is negative, $\nabla \cdot \boldsymbol{u}_g < 0$; (iv) gas temperature reaches the floor of the cooling function or the cooling time becomes shorter than the dynamical time $t_{\rm dyn} = \sqrt{3\pi/(32G\rho_b)}$. The particle is formed with a velocity equal to the surrounding gas, mass $m_* = \epsilon_{\rm SF}(dt/t_{\rm dyn})\rho dx^3$, where $\epsilon_{\rm SF} = 0.05$ is the star formation efficiency, dt is the timestep, and dx is the local cell size. A mass equal to the particle mass is removed from the gas. We set a minimum particle mass $m_{*,\rm min} = 10^5 M_\odot$ in order to manage the number of particles formed, but we still permit particles with $m_* < m_{*,\rm min}$ to form with a probability $m_*/m_{*,\rm min}$ and mass $m_* = 0.8\rho dx^3$.

In order to model feedback due to stellar winds and SNe, we inject gas thermal energy and momentum, as well as CRs energy. The gas and CR energy is injected into the particle's local cell, while the momentum is injected into the immediately surrounding cells as in *Farber et al.* (2022). [1] The inclusion of momentum feedback is essential when the resolution does not sufficiently resolve the cooling radius, as the energy injected can be quickly radiated away and fixes such as delayed cooling over predict the late-time SN evolution (*Martizzi et al.*, 2015). The full details of the momentum feedback are found in *Farber et al.* (2022) and we briefly summarize here. We use the following model for SNe evolution in an inhomogeneous medium, found in Eq. 12 of *Martizzi et al.* (2015), where we assume solar metalicity:

$$
\begin{aligned}
\alpha &= -11 \left(\frac{n_{\rm H}}{100{\rm cm}^{-3}}\right)^{0.114} \\
R_{\rm c} &= 6.3 \text{ pc} \left(\frac{\rm n_H}{100{\rm cm}^{-3}}\right)^{-0.42} \\
R_{\rm r} &= 9.2 \text{ pc} \left(\frac{\rm n_H}{100{\rm cm}^{-3}}\right)^{-0.44} \\
R_0 &= 2.4 \text{ pc} \left(\frac{\rm n_H}{100{\rm cm}^{-3}}\right)^{-0.35} \\
R_{\rm b} &= 8.0 \text{ pc} \left(\frac{\rm n_H}{100{\rm cm}^{-3}}\right)^{-0.46} .
\end{aligned}
\tag{4.8}
$$

[1] *Holguin et al.* (2019) did not include this addition of momentum feedback.

The momentum $P_{\rm r}(R)$ deposition at a particular distance R from center of the cell containing a stellar particle is written as

$$P_{\rm r}(R)/P_0 = \left(\frac{R}{R_0}\right)^{1.5} \Theta(R_{\rm b} - R) + \left(\frac{R_{\rm b}}{R}\right) \Theta(R - R_{\rm b}) \tag{4.9}$$

where $\Theta(x)$ is the Heaviside step function, $P_0 = f_{*,\rm mom}\sqrt{2\phi\epsilon_{\rm SN}N_{\rm SN}0.9M_{\rm ej,0}}$. The parameter $f_{*,\rm mom}$ represents a boost to the momentum received by the surrounding gas (*Agertz et al.*, 2013; *Semenov et al.*, 2018), to compensate for advection errors, clustering of supernovae (*Gentry et al.*, 2017, 2020) and backreaction of cosmic rays (*Diesing and Caprioli*, 2018).

4.4.3 Radiative Cooling

Radiative cooling is calcuated using the Townsend cooling method (*Townsend*, 2009; *Zhu et al.*, 2017), updated from *Farber et al.* (2018, 2022) to include net heating. We approximate the radiative cooling functions from *Dalgarno and McCray* (1972) and *Raymond et al.* (1976) with a piecewise power law cooling function $\Lambda(T)$ in units of $\rm cm^3 s^{-1}$ as

$$\Lambda(T) = \begin{cases} 0 & \text{if } T < 300 \\ 2.2380 \times 10^{-32} T^{2.0} & \text{if } 300 \leq T < 2000 \\ 1.0012 \times 10^{-30} T^{1.5} & \text{if } 2000 \leq T < 8000 \\ 4.6240 \times 10^{-36} T^{2.867} & \text{if } 8000 \leq T < 10^5 \\ 1.7800 \times 10^{-18} T^{-0.65} & \text{if } 10^5 \leq T < 4 \times 10^7 \\ 3.2217 \times 10^{-27} T^{0.5} & \text{if } 4 \times 10^7 \leq T, \end{cases} \tag{4.10}$$

where T is the gas temperature in K. This cooling function is appropriate for a gas of solar abundance, which is completely ionized at $T = 8000$ K.

4.4.4 Radiative Heating

Radiative heating from stellar sources is calculated using a temporally-varying parallel-plane model, similar to (*Kim and Ostriker*, 2017), including from both FUV (6 eV $< h\nu <$ 13.6 eV, far ultraviolet) and ionizing (or EUV, $h\nu >$ 13.6 eV, extreme ultraviolet) spectrum ranges. Photoelectric heating occurs when FUV radiation interacts and frees electrons from interstellar dust grains (*Weingartner and Draine*, 2001b). Photoionization heating occurs when ionizing radiation frees electrons from a hydrogen atom and the electron eventually recombines, having lost some energy to the surrounding plasma (*Osterbrock and Ferland*, 2006).

The radiative heating rates in those two ranges $H_{\rm rad,FUV}$ and $H_{\rm rad,EUV}$, are proportional to the total stellar population particle intensities $L_{\rm FUV}$ and $L_{\rm EUV}$ respectively, at a given simulation time. Due to the parallel-plane approximation, the position of the particles does not matter. We calculate the individual stellar particle immensities using STARBURST99 (*Leitherer et al.*, 1999), which gives a spectrum (erg $\rm s^{-1}Hz^{-1}M_{\odot}^{-1}$) of a stellar population at a fixed mass M and age $t_{\rm p}$. We integrate the spectrum in the FUV and EUV ranges to derive the time-dependent luminosity-to-mass ratio $\Psi(t_{\rm p})$ shown in Figure 4.1. Since hydrogen photoionization cross section drops rapidly above 13.6 eV, we consider the EUV range to be 13.6 eV $< h\nu <$ 27.2 eV.

We calculate the total luminosity in each band by summing the luminosity of each particle, given its age and mass from Ψ. Radiative heating occurs only in neutral gas. *Kim and Ostriker* (2017) models the transition between neutral and ionized gas regimes with a temperature dependent mean molecular weight interpolation, following results from *Sutherland and Dopita* (1993). We instead use sharp transition between neutral and ionized regimes at a temperature $T_{\rm ion} = 1.5 \times 10^4$ K. This transition temperature is also used to determine the regime of CR losses. We use the photoelectric heating rate $\Gamma_{\rm pe}$ from *Kim and Ostriker* (2017), assuming a 4 $\rm kpc^2$

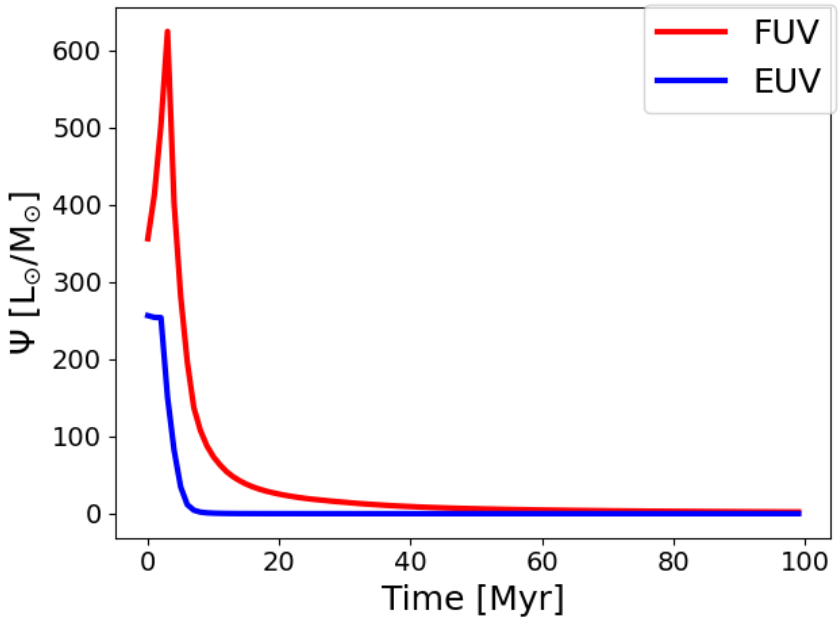

Figure 4.1: Luminosity-to-mass ratio ($L_\odot$ per $M_\odot$) from Starburst99 in the FUV and EUV wavelength ranges as a function of stellar population age. Using these data points, we assign a a luminosity to each stellar population particle, and the total luminosity is used to calculate the radiative heating rates in Eqs. 4.11 and 4.12.

cross section for our parallel-plane domain.

$$\begin{aligned} H_{\rm rad,FUV} &\sim \Gamma_{\rm pe,0}\, n_{\rm H} \left(\frac{\Sigma_{\rm FUV}}{\Sigma_{\rm FUV,0}} + 0.0024 \right) \\ &\sim 2 \times 10^{-26} \left(\frac{n_{\rm H}}{\rm cm^{-3}} \right) \left(\frac{1}{2.8} \left(\frac{L_{\rm FUV}}{10^7 L_\odot} \right) + 0.0024 \right) \ {\rm erg\ s^{-1} cm^{-3}} \end{aligned} \tag{4.11}$$

where $\Sigma_{\rm FUV} = L_{\rm FUV}/(l_{\rm x} l_{\rm y})$ and $l_{\rm x} = l_{\rm y} = 2$ kpc.

The photoionization heating rate for hydrogen (*Osterbrock and Ferland*, 2006) is given by

$$H_{\rm rad,EUV} = n_{\rm H} \int_{\nu_0}^{\infty} \frac{4\pi J_\nu}{h\nu} \sigma_\nu h(\nu - \nu_0) {\rm d}\nu, \tag{4.12}$$

where $n_{\rm H}$ is the neutral hydrogen number density, $h\nu_0 \approx 13.6$ eV $= 1$ Ryd is the hydrogen ionization energy , J_ν is the specific intensity, σ_ν is the frequency-dependent ionization cross section of neutral hydrogen. We integrate in the range $h\nu = [1$ Ryd,

2 Ryd] and assume J_ν is roughly constant over this interval. For a slab geometry with attenuating gas, the mean intensity is given by $4\pi J_{\rm EUV} = \Sigma_{\rm EUV}(1 - E_2(\tau_\perp/2))/\tau_\perp = \Sigma_{EUV} A(z)$ (*Ostriker et al.*, 2010), where A(z) is the attenuation factor accounting for absorption of ionizing radiation by neutral hydrogen as a function of height z above the galactic midplane, E_2 is the second exponential integral, $\tau_\perp = \kappa_{\rm ion}\Sigma(z)_n$, $\Sigma_{\rm n,gas}$ is the neutral column density from the midplane to a given z. . All together $J_\nu \sim \frac{J_{\rm EUV}}{\Delta\nu} \sim \frac{L_{\rm EUV}}{\Delta\nu\ 4\ {\rm kpc}^2}$ for our geometry. The heating rate is calculated as follows

$$
\begin{aligned}
H_{\rm ion} &= n_{\rm H} \int \frac{4\pi J_\nu}{h\nu} \sigma_\nu h(\nu - \nu_0) {\rm d}\nu \\
&\sim n_{\rm H} \left(\frac{J_{\rm EUV}}{\Delta\nu}\right)\ A(z)\ \int 4\pi\sigma_\nu \frac{h(\nu-\nu_0)}{h\nu} {\rm d}\nu \\
&\sim 5\times10^{-22} \left(\frac{n_{\rm H}}{{\rm cm}^{-3}}\right)\left(\frac{L_{\rm EUV}}{10^7 L\odot}\right)\ A(z)\ \ {\rm erg\ s^{-1} cm^{-3}} \\
&\sim 10^{-26} \left(\frac{n_{\rm H}}{{\rm cm}^{-3}}\right)\left(\frac{L_{\rm EUV}}{10^7 L_\odot}\right)\left(\frac{\Sigma_{\rm n}(z)}{50 M\odot/{\rm pc}^2}\right)^{-1}\ {\rm erg\ s^{-1} cm^{-3}}
\end{aligned}
\tag{4.13}
$$

The total radiative heating is $H_{\rm rad}(n_{\rm H}, L_{\rm FUV}, L_{\rm EUV}, z) = H_{\rm rad,FUV} + H_{\rm rad,EUV}$. The overall net energy recieved by gas is $(H_{\rm rad} - \Lambda)$, which can take a positive or negative value. The addition of net heating requires an modification of the Townsend cooling code. Appendix 4.10 describes the updated algorithm and tests.

We do not include dynamical coupling between the radiation field and gas. The FUV portion of the stellar spectrum exerts pressure on the dust, which is coupled to the gas. Generally, for winds driven by radiation pressure to be efficient, the stellar flux must be near the dust Eddington limit, which is usually the case in in high redshift and/or star bursting galactic environments (*Zhang*, 2018). In both observed and simulated Milky Way-like galaxies, the regime that our work focus on, other parts of stellar feedback likely dominate the acceleration of galactic winds (*Andrews and Thompson*, 2011; *Hopkins et al.*, 2012).

4.4.5 Cosmic Ray Physics

CR coupling to gas via advection and diffusive transport follows a similar model as in *Farber et al.* (2018). We use a constant value $\kappa_{\rm cr}$ for the CR diffusivity parallel. We do not use the CR streaming model from *Ruszkowski et al.* (2017); *Holguin et al.* (2019). As CRs travel through the ISM, they interact inelastically with particles in the ISM. We include both hadronic and Coulomb losses with a model from *Guo and Oh* (2008), as implemented in *Chan et al.* (2019), modeling $\Gamma_{\rm cr}$, the energy loss rate of the CRs, and $\Gamma_{\rm cr,gas}$, the amount of the CR loss rate that is absorbed by the gas (with the rest of the energy lost as gamma rays):

$$\begin{aligned}\Gamma_{\rm cr} &= -5.86\times10^{-16}\,(1+0.282\,x_e)\left(\frac{n_{\rm n}}{\rm cm^{-3}}\right)\left(\frac{e_{\rm cr}}{\rm erg\ cm^{-3}}\right)\ {\rm erg\ cm^{-3}s^{-1}}\\ \Gamma_{\rm cr,gas} &= 0.98\times10^{-16}\,(1+1.7\,x_e)\left(\frac{n_{\rm n}}{\rm cm^{-3}}\right)\left(\frac{e_{\rm cr}}{\rm erg\ cm^{-3}}\right)\ {\rm erg\ cm^{-3}s^{-1}}\end{aligned} \tag{4.14}$$

where $n_{\rm n}$ is the number of nucleons, x_e is the number of free electrons per nucleon, and $e_{\rm cr}$ is the CR energy density. Appendix 4.11 further describes the algorithm implementation and tests of its validity.

In the self-confinement model of CR transport (*Zweibel*, 2013, 2017), CR streaming along the magnetic field lines is subject to the streaming instability, resulting in the generation of Alfvèn waves. The subsequent wave-particle interactions between the population of CRs and Alfvèn waves limits the bulk CR transport speed to the Alfvèn speed. This process also leads to energy transfer from the CRs to the thermal gas via collisionless heating, according to

$$H_{\rm cr} = -v_{\rm A}\cdot\nabla P_{\rm cr}, \tag{4.15}$$

where $v_{\rm A}$ is the Alfvèn speed and $P_{\rm cr}$ is the CR pressure (*Wiener et al.*, 2013b). We do not include CR streaming in our simulations, only cosmic ray diffusion. The

tangling of magnetic field lines in the turbulent galactic environment likely results in CR streaming effectively looking like CR diffusion. Following this idea, we allow for CR streaming heating even though we do not include streaming itself.

4.4.6 Simulation Domain and Initial Conditions

The elongated $2 \times 2 \times 40$ kpc three-dimensional box geometry represents an approximately parallel-plane section of a galactic disk. The maximum midplane height of ± 20 kpc is chosen to ensure a realistic temperature distribution (*Hill et al.*, 2012), while maintaining the parallel-plane approximation. The horizontal x and y coordinate sides have periodic boundary conditions, while the z coordinate 'top' and 'bottom' have diode boundary conditions, which avoids issues from gas fallback near the boundary (e.g. *Sur et al.*, 2016). We do not include differential rotation effects. We use static mesh refinement with a resolution of 31.25 pc for $|z| < 8$ and 62.5 pc for 8 kpc $< |z| <$ 20 kpc. These higher resolution refinement regions are four times more extended than in *Holguin et al.* (2019) in order to better capture the phase structure of the plasma farther out of the galaxy.

For the gas initial conditions, we use a vertical equilibrium density solution for a stratified, isothermal self-gravitating system (*Spitzer Jr*, 1942; *Salem and Bryan*, 2014) projected to a stratified parallel-plane box (e.g. *De Avillez and Breitschwerdt*, 2007; *Walch et al.*, 2015; *Farber et al.*, 2018; *Holguin et al.*, 2019). The unperturbed density distribution is as follows

$$\rho(z) = \begin{cases} \rho_0 \operatorname{sech}^2\left(\frac{z}{2z_0}\right) & \rho(z) > \rho_{\rm halo} \\ \rho_{\rm halo} & \text{otherwise,} \end{cases} \tag{4.16}$$

where ρ_0 is the initial midplane density and z_0 is the vertical scale height. We can define the initial disk surface gas density as $\Sigma_0 = \int_{-20\rm kpc}^{20\rm kpc} \rho(z) \mathrm{d}z$. The density $\rho_{\rm halo} = 1.0 \times 10^{-28}$ g/cm^3 is the initial density of the halo.

In order to improve reproducibility, we reduce differences in initial star formation due to machine dependent effects by perturbing the density distribution as follows:

$$\rho(z) = \rho(z) \left(1 + \delta_\rho \sum_{i=1}^{3} \sin(\pi \mathrm{x_i}/\mathrm{L}_\delta)^2/3 \right) \tag{4.17}$$

where x_i represents the spatial coordinates and L_δ is the perturbation wavelength in units of the highest resolution of 31.25 pc. We choose the density distribution parameters (see Table 4.1) such that $\Sigma_0 = 100\ M_\odot/\mathrm{pc}^2$, which corresponds to the average surface density within a radius of 10 kpc in the isothermal self-gravitating solution. There are no stellar particles initially. After the bulk of star formation occurs (about 100 Myr) in the simulation, roughly 20 $M_\odot$ is converted to stellar particles. The gas initial temperature is $T = 10^4$ K. The initial magnetic field follows the density distribution as $B(z) \propto \rho(z)^{2/3}$ with the mid-plane value $B_0 \approx 3\mu G$. The field is oriented along one of the horizontal directions.

From the initial conditions the gas radiatively cools and collapses to a smaller scale height distribution, until the densities become large enough (and the other criteria satisfied as described in Section 4.4.2) for stellar particles to form and begin stellar feedback. We do not include any artificial pressure support, as resulting steady-state properties are insensitive to particular choices of pressure support (*Kim and Ostriker*, 2017). By 100 Myr, stellar feedback suppresses star formation and the simulations tends towards steady state.

4.5 Simulation Results

We run 6 simulations, optimizing for computational expense and exploration of the CR and ionizing radiation parameter space. The simulations are summarized in Table 4.2. In the short name for the simulations 'k' is followed by either 28 or 29, referring to the log of κ_{cr}, 'Hrad' refers to the inclusion of radiative heating in both

Table 4.1: Simulation model parameters

Halo	
$M_{200}^{(1)}$	$10^{12}\mathrm{M}_{\odot}$
$c^{(2)}$	12
Disk	
$\rho_o^{(3)}$	5.64 $\times 10^{-23}$ g cm^{-3}
$z_o^{(4)}$	0.03 kpc
$\Sigma_o^{(5)}$	100 $\mathrm{M}_{\odot}$ pc^{-2}
$T_o^{(6)}$	10^4 K
$B_o^{(7)} = B_{o,x}$	3 μG
δ_ρ	0.1
L_δ	8 δx
Star Formation	
$n_{\mathrm{thresh}}^{(8)}$	10 cm^{-3}
$T_{\mathrm{floor}}^{(9)}$	300 K
$m_{*,\mathrm{min}}^{(10)}$	10^5 $\mathrm{M}_{\odot}$
$\epsilon_{\mathrm{SF}}^{(11)}$	0.05
Stellar Feedback	
$f_*^{(12)}$	0.25
$f_{cr}^{(13)}$	0.1
$f_{*,\mathrm{mom}}^{14}$	5.0
$\epsilon_{\mathrm{SN}}^{(15)}$	$10^{51}\mathrm{erg}/(\mathrm{M_{sf}c^2})$
$M_{\mathrm{sf}}^{(16)}$	100 $\mathrm{M}_{\odot}$
$T_{\mathrm{ion}}^{(17)}$	1.5e4 K
$f_*^{(18)}$	[0, 1]
$f_{*,\mathrm{EUV}}^{(19)}$	0.1
Cosmic Ray Feedback	
$\kappa_{\mathrm{CR}}^{(20)}$	$[10^{28}, 10^{29}]$ cm^{2}s^{-1}
$H_{\mathrm{cr}}^{(21)}$	on/off

Notes. From top to bottom the rows contain: (1) halo mass; (2) concentration parameter; (3) initial midplane density; (4) initial scale height of the gas disk; (5) initial gas surface density; (6) initial temperature; (7) initial magnetic field strength; (8) gas density threshold for star formation; (9) floor temperature; (10) minimum stellar population particle mass; (11) star formation efficiency; (12) fraction of stellar mass returned to the ISM; (13) fraction of supernova energy bestowed unto CRs; (14) SNe momentum feedback boost factor, (15) SN energy per rest mass energy of newly formed stars; (16) rest mass energy of newly formed stars per SN; (17) the transition temperature between neutral and ionized gas; (18) multiplicative factor scaling the net radiative heating, including both the stellar and metagalactic components; (19) escape fraction scaling the EUV component of radiative heating, modeling HII region photon escape; (20) CR diffusivity parallel to the magnetic field; (21) inclusion of CR streaming heating or not.

Table 4.2: Summary of the 6 simulations we conducted, spanning limiting cases in CR diffusivity, as well as radiative and CR streaming heating.

Sim Number	Sim short name	$H_{\rm rad}$	log $k_{\rm cr}$ [cm^{2}s^{-1}]	H$_{\rm cr}$
1	k28	No	28	No
2	k28_Hcr	No	2	Yes
3	k28_Hrad	Yes	28	No
4	k28_Hrad_Hcr	Yes	28	Yes
5	k29_Hrad	Yes	29	No
6	k29_Hrad_Hcr	Yes	29	Yes

the FUV and EUV bands, and 'Hcr' refers to the inclusion of cosmic ray streaming heating. All simulations include CRs. In all simulations that include radiative heating there is a reduction in the total EUV luminosity by a factor $f_{*,\rm EUV} = 0.1$, which is a reasonable mean escape fraction for ionizing photons from HII regions, although in practice there is a lot of scatter (e.g. *Leitherer et al.*, 1995; *Pellegrini et al.*, 2012). Due to our increase in the size of the highest resolution region, the added computational cost of $\kappa_{\rm cr} = 10^{29}$ cm^{2}s^{-1} limits the number of simulations we can run at this higher CR diffusivity.

For illustrative purposes, in Figure 4.2 we highlight both of the simulations with higher CR diffusivity, 'k29_Hrad' and 'k29_Hrad_Hcr', which produce extended outflows. The figure shows slices of a $x - z$ plane through the origin. The color in the slices denotes the value of $n_{\rm i}$, T, $n_{\rm cr}$, $H_{\rm rad}$, and $H_{\rm cr}$ along the plane. Radiative heating produces a volume filling $T \sim 10^4$ K medium around the galactic disk, unlike in our previous simulations in *Holguin et al.* (2019), where there is a significant amount of colder phases. The scale height of radiative heating is smaller compared to that of CR streaming heating, when it is enabled. The outflow is weaker with streaming heating present, although the CR distribution does extend far outside the galaxy for the weaker wind. This case suggests that the CRs are losing significant amounts of energy to the surrounding gas.

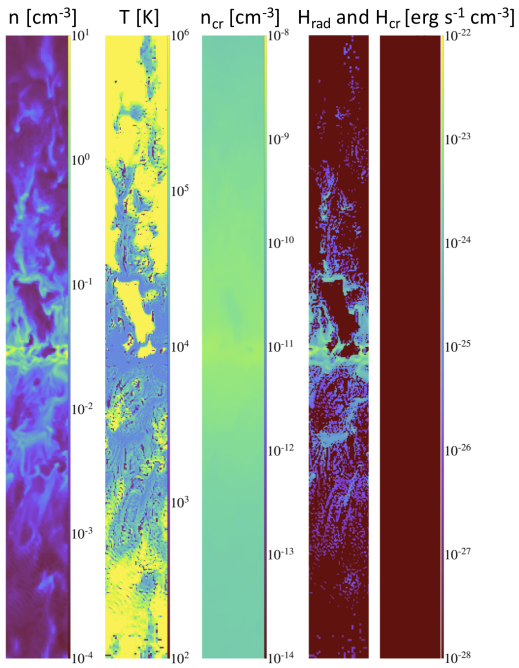

(a) 'k29_Hrad': No CR streaming heating.

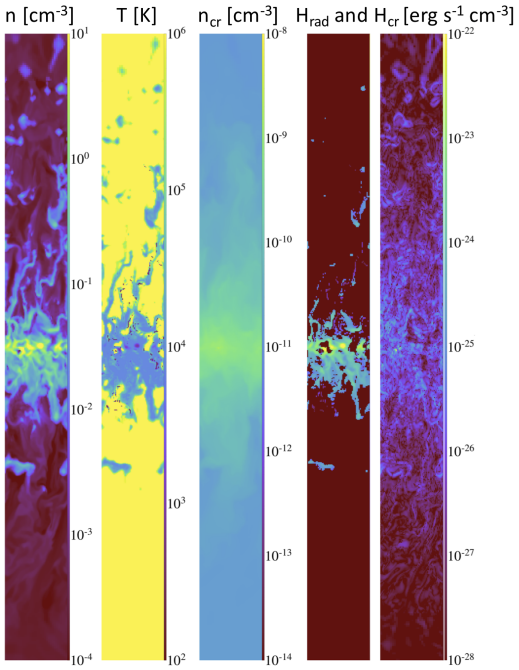

(b) 'k29_Hrad_Hcr': CR streaming heating included.

Figure 4.2: Slice plots from simulations at 120 Myr, both with $\kappa_{\rm cr} = 10^{29}$ cm^{2}s^{-1} and radiative heating. The slice are (left to right) number density n_i, temperature T, cosmic ray number density $n_{\rm cr}$, and heating rates (radiative $H_{\rm rad}$ and CR streaming heating rate $H_{\rm cr}$). The outflow in 'k29_Hrad' extends to the top of the domain at 20 kpc from the midplane. The inclusion of CR streaming heating losses reduces the CR population enough to reduce the extent of the outflow to roughly 10 kpc.

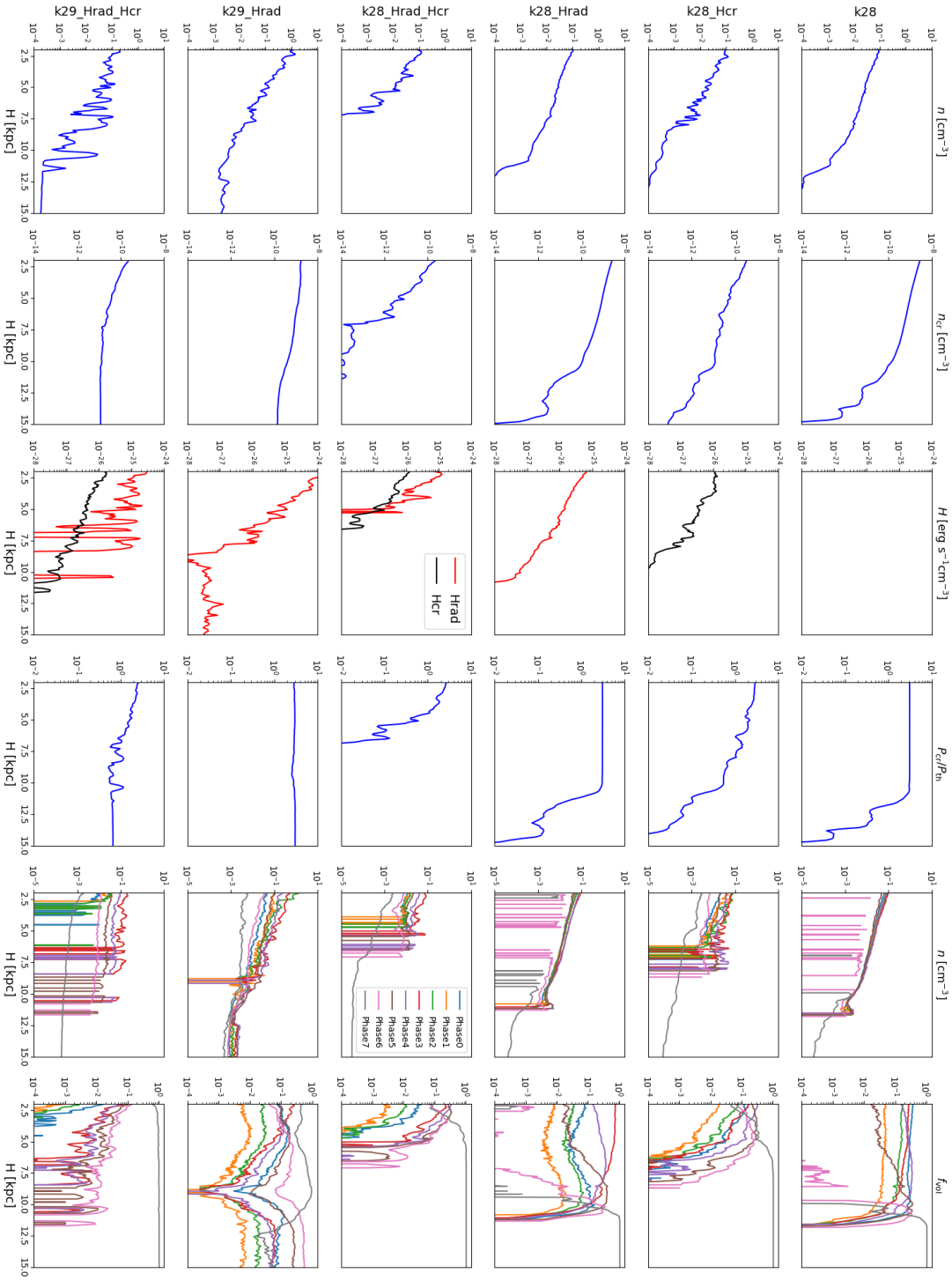

Figure 4.3: Summary of 6 simulations ran with profile plots of key quantities: n, $n_{\rm cr}$, total radiative heating rate H, and non-thermal pressure ratio $P_{\rm cr}/P_{\rm th}$, as well as number density n and volume filling fraction $f_{\rm vol}$ for each gas phase used in Cloudy. The definitions of the phases are in Eq. 4.20. The CR diffusivity runs 'k28' and 'k29' are plotted at 190 and 140 Myr respectively.

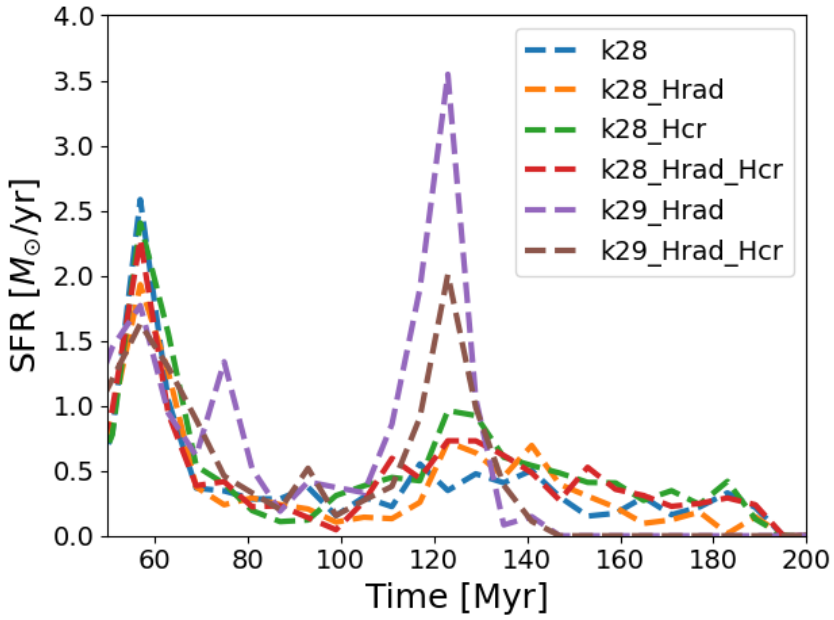

Figure 4.4: SFR of the 6 simulations we ran. There is an initial burst of star formation at 60 Myr. The simulations with higher $\kappa_{\rm cr}$ experience another, larger burst of star formation at 120 Myr, due to CRs leaving the dense disk more efficiently. This removal of pressure support triggers more gravitational collapse and star formation.

In Figures 4.3 and 4.4, we compare the simulation results for all 6 of the simulations we conducted for key quantities. In Figure 4.3 we refer to columns and rows relative to the label orientation, in that the columns show profile quantities like n and $n_{\rm cr}$ and the rows are of different simulations. The last two columns show the number density and volume filling fractions of the phases used for post-processing in Eq. 4.20. First, we describe simulations without CR streaming heating. Radiative heating has the effect of reducing the volume filling fraction of the cold neutral medium (phases 0, 1, and 2) while increasing the fraction of the warm neutral and ionized phases (phases 3 and 4). The hotter phases are not significantly affected, as radiative heating does not affect ionized plasma. The density profiles of the phases remain similar, as the phases are dominated by non-thermal pressure support instead of thermal pressure support, which is shown in the fourth column. The outflows for the lower $\kappa_{\rm cr}$ runs are weaker than in the higher $\kappa_{\rm cr}$ case, in agreement with previous works (e.g. *Salem*

and Bryan, 2014; *Hopkins et al.*, 2020; *Farcy et al.*, 2022) . The outflows extend to roughly 10 kpc for lower CR diffusivity and 20 kpc for higher CR diffusivity. With higher CR diffusivity, the density profiles of the gas phases within 10 kpc are not so tightly overlapping, even though the non-thermal pressure support is dominant. The overlapping of phase densities does occur past 10 kpc. The dominant phases in the outflow are the hot phases (phases 6 and 7), unlike the lower $\kappa_{\rm cr}$ case. There is also a resurgence in star formation for higher $\kappa_{\rm cr}$, likely due to CRs more easily leaving the galactic disk and reducing gas pressure support after their initial injection by the first burst of star formation.

Simulations with CR streaming heating significantly reduce the spatial extent of outflows from the galaxy for both values of $\kappa_{\rm cr}$. The energy transfer to the gas may not have a large influence in its thermal energy for some parts of the cooling curve (see *Hopkins et al.*, 2020), but the energy loss can be significant to the CR population. In a CGM model with a fixed CR flux *Huang and Davis* (2022) similarly found that CR streaming heating can be a dominant mechanism of energy transfer from the CRs. Two quantities point to the outflow weakness being caused by the reduction in CR energy density: $H_{\rm cr}/\Gamma_{\rm cr}$ (the CR energy loss rate relative to hadronic and Coulomb processes in Eq. 4.18) and the loss timescale $\tau_{\rm cr,st} \sim e_{\rm cr}/H_{\rm cr}$ (Eq. 4.19). CR collisional losses are proportional to gas density, so as the density decreases farther away from the galaxy, these losses are reduced. Setting the collisional and collisionless CR loss terms equal to each other yields a critical number density,

$$\begin{aligned} H_{\rm cr} &\sim \Gamma_{\rm cr} \\ n &\sim 0.1 \text{ cm}^{-3} \text{ B}_{\mu\text{G}} \text{ L}_{\rm cr}, \end{aligned} \tag{4.18}$$

where $L_{\rm cr}$ is the length scale of the global cosmic ray distribution and $B_{\mu G}$ is the magnetic field strength in μG. Below this density, collisionless losses dominate over collisional losses. For reasonable parameters in the low density medium above

the galaxy, CR streaming losses should be the dominant loss mechanism below $n \sim 0.1$ cm^{-3}. We also calculate the timescale of CR energy loss via CR streaming heating,

$$\begin{aligned} \tau_{\rm cr,st} &= e_{\rm cr}/H_{\rm cr} \\ &= e_{\rm cr}/|v_{\rm A} \cdot \nabla P_{\rm cr}| \\ &\sim 100 \text{ Myr } \left(\frac{\rm L_{cr}}{\rm kpc}\right) \left(\frac{\rm n}{\rm cm^{-3}}\right)^{1/2} {\rm B}_{\mu\rm G}^{-1}, \end{aligned} \tag{4.19}$$

which indicates that for reasonable parameters, the energy loss timescale is of order the total simulation time of 200 Myr, or shorter in lower density regions. The column for $P_{\rm cr}/P_{\rm th}$ in Figure 4.3 shows that in the simulations with CR streaming heating, CRs retain pressure dominance in the disk (within 3 kpc) but farther out of the galaxy, thermal pressure dominates, as expected by our analysis above. In the heating rate column, we note that CR streaming heating does not match the radiative heating rate until roughly 7-10 kpc in simulations with both heating mechanisms included. Although, it is likely we could be overestimating the radiative heating rate farther away from the galaxy since a non-attenuated parallel-plane radiation field does not decay with height. In global simulations, the radiative heating rate could fall faster with height above the disk, allowing other heating mechanisms like CR streaming heating to dominate for a larger range in height.

4.6 Post-Processing Framework with Cloudy

4.6.1 Division of Simulation Domain and Cloudy Model Setup

In order to efficiently produce synthetic plasma diagnostics from our simulations, we use the spectral synthesis code, Cloudy (*Ferland et al.*, 2017). A typical Cloudy parallel-plane model takes inputs of hydrogen density, plasma temperature, metalicity, and incoming spectra (radio to x-ray), resulting in outputs of species ionization state

and outgoing spectra. We use the MHD simulations to inform various Cloudy models. Cloudy is able to calculate the plasma temperature. However, this calculation does not include the various feedback mechanisms present in the three dimensional MHD simulation, so we let the model temperature be informed by the simulation. We calculate the galactic midplane spectra $J_{\nu,*}$ by assigning spectra to each simulation stellar population particle based on particle age and mass using Starburst99.

Figure 4.5 shows a diagram that illustrates the post-processing framework. We divide the simulation domain into parallel-plane sections that are two resolution elements in height. Within each section i, we calculate the mean and standard deviation of n and T of each gas phase. We define eight gas phases in each section i from the temperature floor to hot coronal gas as follows,

$$\begin{aligned}
&\text{Phase 0} : T < 500\text{K} \\
&\text{Phase 1} : 500\text{K} < \text{T} < 2000\text{K} \\
&\text{Phase 2} : 2000\text{K} < \text{T} < 8000\text{K} \\
&\text{Phase 3} : 8000\text{K} < \text{T} < 1.5 \times 10^4\text{K} \\
&\text{Phase 4} : 1.5 \times 10^4\text{K} < \text{T} < 3 \times 10^4\text{K} \\
&\text{Phase 5} : 3 \times 10^4\text{K} < \text{T} < 10^5\text{K} \\
&\text{Phase 6} : 10^5\text{K} < \text{T} < 10^6\text{K} \\
&\text{Phase 7} : 10^6\text{K} < \text{T}
\end{aligned} \tag{4.20}$$

which include rough matches to the traditional ISM phases (phase 3: warm, neutral medium; phase 4: warm, ionized medium). Each phase j has mean density $\langle \rho_{i,j} \rangle$, temperature $\langle T_{i,j} \rangle$, and associated standard deviations $\sigma_{\rho,i}$ and $\sigma_{T,i}$ respectively, as well as the filling fraction $f_{\text{vol;i,j}}$ of each phase in that section. A Cloudy model is assigned density $\rho^{\text{C}}_{i,j}$ and temperature $T^{C}_{i,j}$ by drawing from a Gaussian distribution defined by the mean and standard deviation of density and temperature of each

phase, with values limited to be within one standard deviation. We draw properties 10 times in order to produce 10 separate profiles of density and temperature in the domain. These separate profiles allow us to produce intervals in the synthetic line ratio profiles. The incoming spectra for each model is the midplane spectra $J_{\nu;*}$ if $i = 0$ (lowest height section) or $J_{\nu;i-1}$ (the outgoing spectra from section below the current one) otherwise. The output spectra of the Cloudy model is $J_{\nu;i,j}$. The total outgoing spectra $J_{\nu,i}$ for section i is the sum of the eight spectra in each phase $J_{\nu;i,j}$ weighted by the phase filling fraction $f_{\mathrm{vol;i,j}}$, which becomes the input spectra to the Cloudy models in the next section $i + 1$. Through this framework, we obtain estimates of the ionization state of numerous species and are then able to generate plasma diagnostics that are spatially (with midplane height) and temporally dependent.

The parameter f_* is a binary value that activates or suppresses the presence of radiative heating. Due to limited resolution, we do not resolve the giant star forming complexes where massive stars form. We multiply the ionizing part of the stellar spectrum by an escape fraction $f_{*,\mathrm{EUV}}$ to account for the absorption of hydrogen ionizing photons after emission from stars and out into the ISM. We also have $f_{\mathrm{bkg,EUV}}$, the fraction of the metagalactic background field present. $f_{\mathrm{bkg,EUV}}$ is a binary on/off option. Since the post-processing models the outward and not inward propagation of radiation, the metagalactic background field must be included in each Cloudy model as a binary on/off option. The metagalactic field is added to a Cloudy model by specifying the desired field name. We use 'HM12' (*Haardt and Madau*, 2012) for our work. In order to avoid adding the previous slab attenuated background field every time we transmit a spectra to a new domain section, we add the 'no isotropic' option, which automatically removes the attenuated component of the isotropic spectra sources. Overall, we have consistency between the the choices in post-processing parameters and simulation parameters (e.g., same f_*, $f_{*,\mathrm{EUV}}$ and $f_{\mathrm{bkg,EUV}}$ in simulation and post-processing).

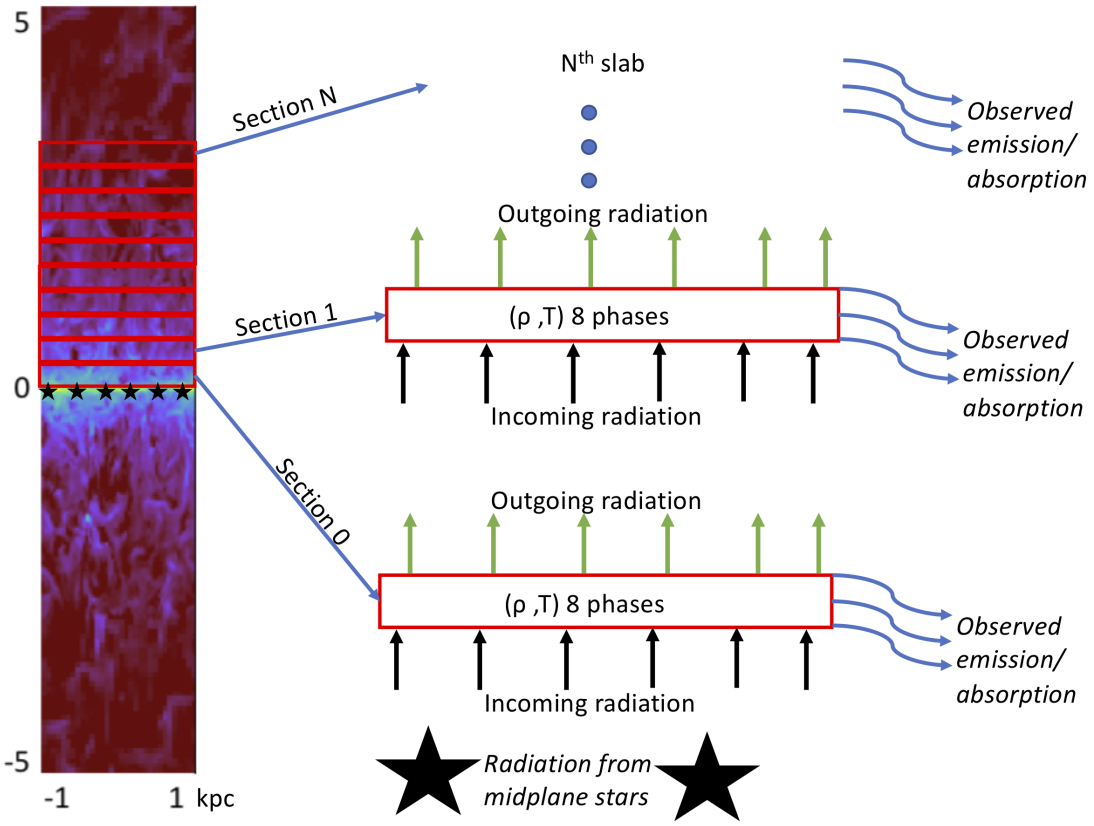

Figure 4.5: Diagram of MHD simulation and Cloudy post-processing framework. A slice ($2 \times 2 \times 5$ kpc) of an example simulation is shown divided up into red parallel plane sections, the properties of which are used to inform Cloudy models. Each section holds eight temperature phases, from Eq. 4.20, each with mean density ρ, temperature T and volume filling factor $f_{\rm vol}$. The midplane spectra from the stellar population particles is transmitted outward through the sections. We calculate the ionization state of H, C, N, O, and Si ions in each section.

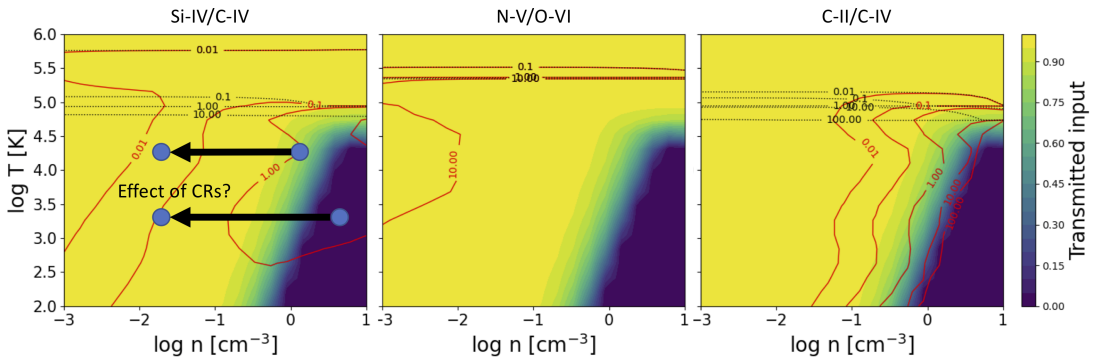

Figure 4.6: Line ratio diagnostics from Cloudy in density and temperature space for a 50 pc slab ($\sim$ 2 high resolution cell widths from our MHD simulations). The black dotted contours show the line ratio values assuming collisional ionization, while the red contours show the values with the addition of photoionization from a constant SFR stellar population spectrum (SFR = 1 $M_\odot$/yr). The background color shows the transmission fraction through the slab for reference. The addition of the stellar field significantly changes the line ratio contours at $T < 10^5$ K, except for N-V/O-VI. We sketch the potential effect of non-thermal pressure support on the Si-IV/C-IV plot. The right pair of blue dots are placed roughly where the traditional warm, ionized medium and cold, neutral phases exist based on thermal equilibrium. When the dominant pressure source is non-thermal pressure, multiple phases can exist at the same density (e.g. *Ji et al.*, 2020). When these phases are shifted to lower densities, the line ratio values are closer to Milky Way values. In a realistic system the dominant pressure support will vary between thermal and non-thermal, so the analysis here provides limiting cases.

4.6.2 Theoretical Expectations

We focus on three relatively common absorption diagnostic line ratios: two intermediate (ionization energy > 13.6 eV) ion ratios, Si-IV/C-IV and N-V/O-VI, as well as one low ion, C-II/C-IV (*Tumlinson et al.*, 2017). These diagnostics are chosen as they span temperature ranges from the warm, neutral phases (phases 3,4) to just below the hot phase (phase 5). Line ratio diagnostics are convenient to use because our parallel-plane domain represents only a piece of the galaxy, preventing an accurate prediction in the total ion column densities. In order to explore the temperature and density parameter space that the simulation post-processing will effectively draw from, we run a grid of 20 by 20 data points of Cloudy models in $n_{\rm i} = [10^{-3}, 10^{1}]$ cm^{-3} and $T = [10^{2}, 10^{6}]$ K, evenly spaced in log space, similar to common analyses done in

observationally focused work (e.g., *Fox et al.*, 2005). The Cloudy models all assume the same domain thickness of 50 pc, roughly the size of two of the highest resolution elements in the MHD simulations. The input radiation field is that of the SFR = 1 $M_{\odot}\mathrm{yr}^{-1}$ stellar population spectra from Starburst99, multiplied by an escape fraction $f_{*,\mathrm{EUV}} = 0.1$. The results are shown in Figure 4.6 for Si-IV/C-IV, N-V/O-VI, and C-II/C-IV from left to right. The black line contours correspond to the line ratio values without any external radiation field. The red line contours show the line ratio values with the stellar field included. The background filled color corresponds to the transmission fraction of the incoming spectra through the slab. This color is plotted to illustrate the optical thickness of the medium to the spectra.

The relatively constant value of Si-IV/C-IV ~ 0.2 observed in the Milky Way (*Savage and Wakker*, 2009; *Werk et al.*, 2019) is a useful guide for examining the line ratio parameter space. Without external radiative effects (i.e. only collisional ionization), the only gas phases that could produce the observed line have $T \sim 10^5$ K, as we expect from the ionization energy of the ions. The value of the line ratio is also quite sensitive to the temperature around $T \sim 10^5$ K, with two orders of magnitude changes in value in a narrow temperature band. With a SFR = 1 $\mathrm{M}_{\odot}\mathrm{yr}^{-1}$ stellar field added, the line ratio contours are quite different at $T < 10^{5.5}$ K. Lower temperature models in the range $T = [10^3, 10^4]$ K are able to produce Si-IV/C-IV ~ 0.2, but only at low densities of $n \sim 10^{-1.5}$ cm^{-3}. Under standard ISM thermal pressure balance (*McKee and Ostriker*, 1977; *Draine*, 2010), these phases of gas are required to be much denser to remain in pressure equilibrium with the hot gas phase. By providing a non-thermal pressure source, cosmic rays can allow multiple phases to exist at the same density (see *Ji et al.*, 2020), in particular, by allowing more tenuous cold phases. The overplotted blue circles roughly mark where (right) thermally and (left) non-thermally gas phases exist. Whereas in the thermally supported case, lower temperature phases cannot reproduce observed line ratio values even with an external

radiation field, with cosmic rays, a variety of phases from $T = 10^3$ K to $T = 10^5$ K could reproduce the observed line ratio values.

The parameter space for C-II/C-IV is similar to that of Si-IV/C-IV. The addition of a stellar radiation field allows phases with $T < 10^5$ K to produce lower line ratio values. With non-thermal pressure support, these tenuous, cold phases can plausibly exist and contribute to the observed signal. The N-V/O-VI line ratio is more resistant to change by the external stellar field, as expected by the higher ionization energy of the ions. Typical observed values of the line ratio are in the range $[10^{-1.5}, 10^1]$ (*Wakker et al.*, 2012), which are found in a small part of the parameter space in Figure 4.6. Some line values of roughly 10^1 can occur at $\sim 10^4$ K with a stellar radiation field present, but only in very tenuous gas with $n < 10^{-2}$ cm^{-3}. We additionally tested (not shown here) the effect of only the metagalatic background field and found that it produces effects in between that of the collisional ionization and stellar field cases. The metagalactic background field itself is not sufficient to change the parameter space significantly.

Besides pressure support, CR streaming heating could have an impact on the gas thermal state. Radiative heating does not occur in a significantly ionized gas, so the radiation field does not heat this gas (although radiative effects on the line emission/absorption still can occur). *Wiener et al.* (2013b) suggested that because the CR scale height extends well outside the galactic disk and collisionless CR streaming heating affects the ionized medium, CRs could provide a plausible heating mechanism to explain anomalously high electron densities outside the disk (*Reynolds et al.*, 1999). Regardless of the pressure equilibrium (thermal or non-thermal), additional energy injection into the ISM/CGM plasma reduces the value of the Si-IV/C-IV and C-II/C-IV line ratios in Figure 4.6.

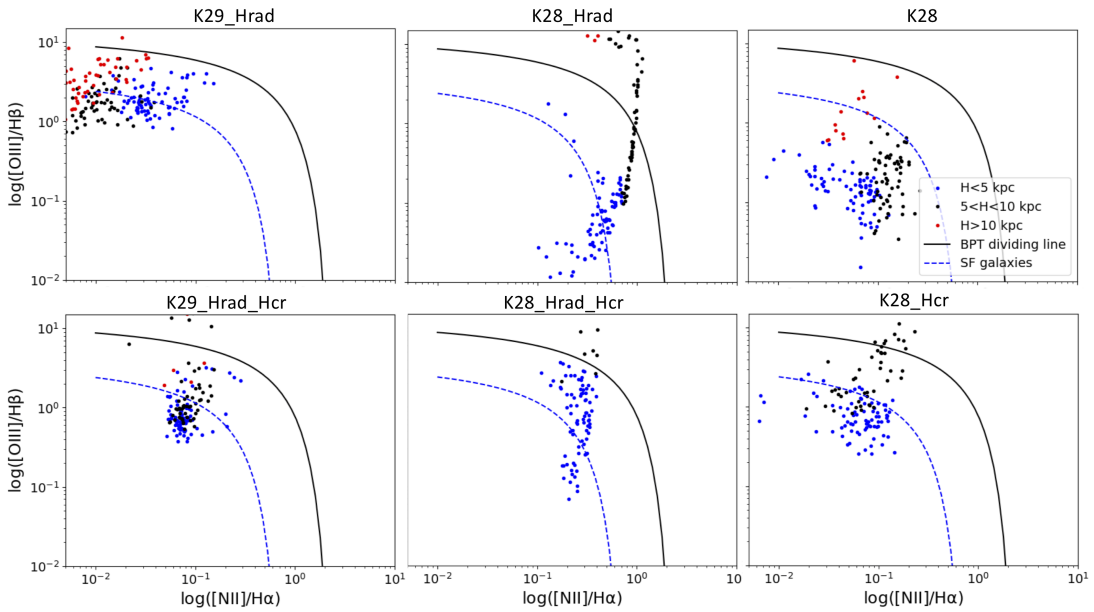

Figure 4.7: BPT diagram of 6 simulations. The solid line denotes the general line between star forming and active galaxies fitted from the *Kewley et al.* (2001) fit, while the dashed line denotes the rough trend for star forming galaxies. The $\kappa = 10^{28}$ cm^{2}s^{-1} simulations are shown at 190 Myr, and the $\kappa = 10^{29}$ cm^{2}s^{-1} are shown at 120 Myr (same time shown in Figure 4.2). Generally, the regions closer to the galactic disk (< 5 kpc) in all of the simulations were roughly on the star forming sequence, except for 'k28', which did not include radiative or CR streaming heating.

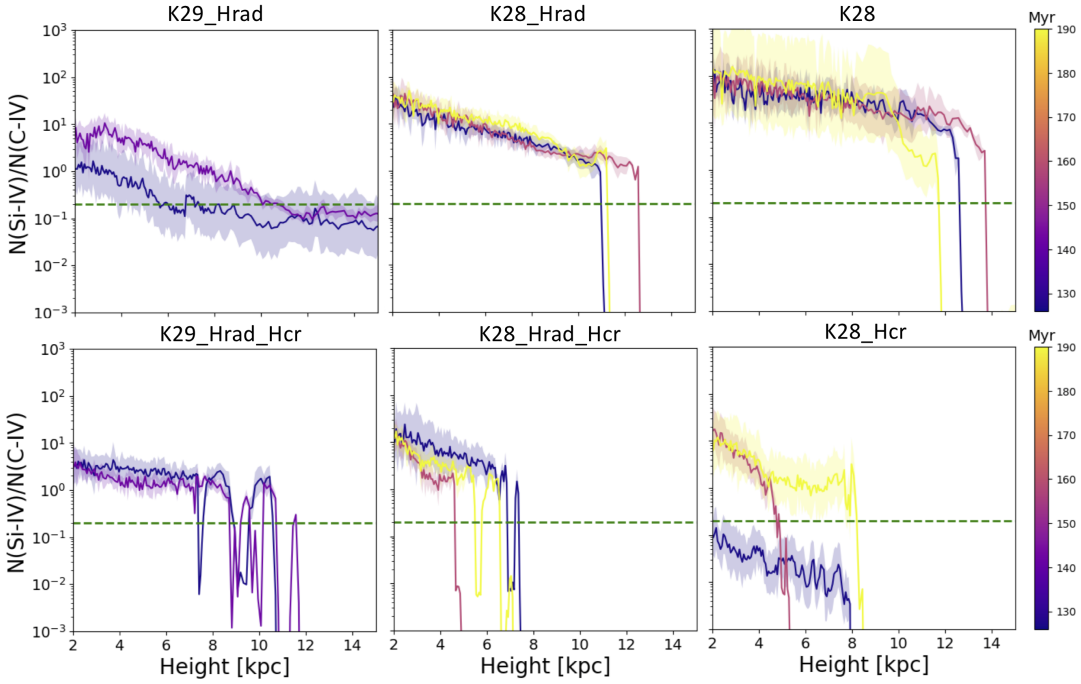

Figure 4.8: Line ratio profiles of Si-IV/C-IV for 6 simulations, colored by simulation time. The dashed, green line denotes the observed value in the Milky Way [cite more] (*Werk et al.*, 2019). For high CR diffusivity, 'k29_Hrad' (not including CR streaming heating) had the best match to Milky Way value. For low CR diffusivity, the addition of CR streaming heating reduced the line ratio values towards observed values, but the gas outflow was weak.

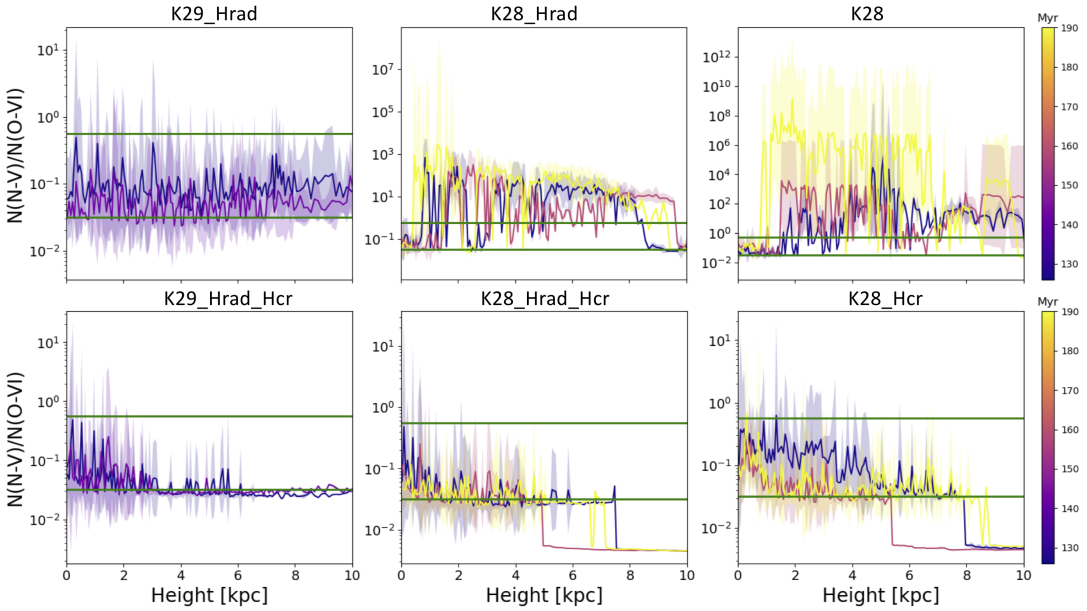

Figure 4.9: Line ratio profiles of N-V/O-VI for 6 simulations, colored by simulation time. The solid green lines denote the rough range of observed values compiled in *Wakker et al.* (2012) from many sources. Both simulations with high CR diffusivity have line ratio values within the observed range, while for low CR diffusivity, only the simultions with CR streaming heating have line ratio values consistently within the range.

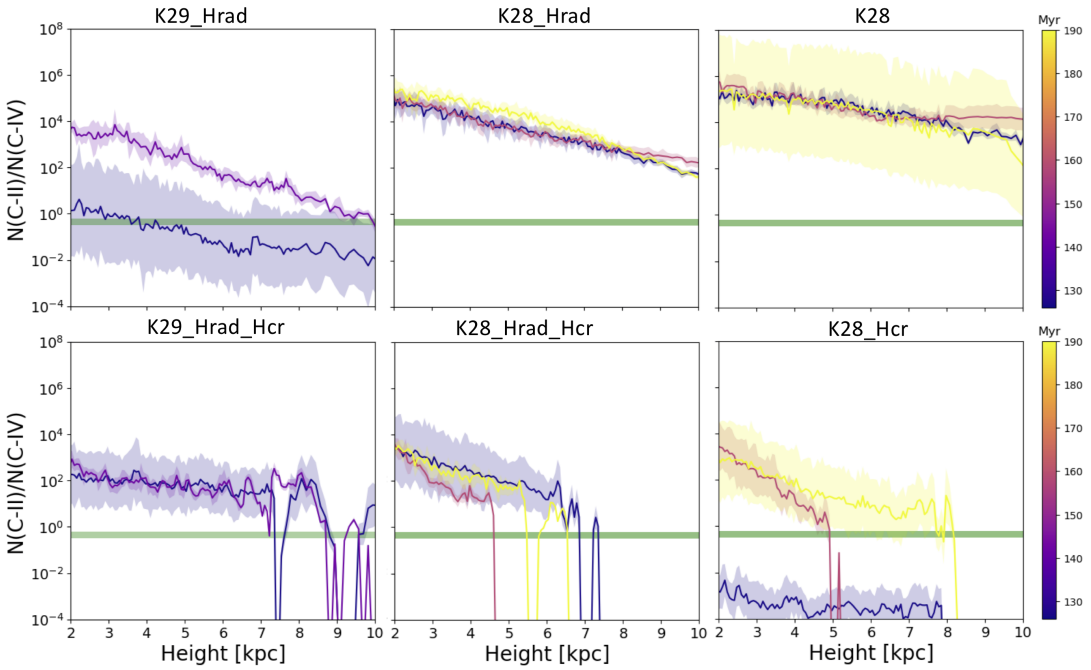

Figure 4.10: Line ratio profiles of C-II/C-IV for 6 simulations, colored by simulation time. The green range denotes the mean value ± standard deviation of the ratio from data in *Fox et al.* (2005). This value is meant to provide a rough guide for typical values around the Milky Way halo. The results were similar to that of Si-IV/C-IV in Figure 4.8, where the simulations closer to observed values were 'k29_Hrad' and 'k28_Hcr' at high and low CR diffusivity respectively.

4.7 Post-Processing Results

We post-process 6 simulations using the method described in Section 4.6.1. Figure 4.7 shows where each simulation falls on the BPT diagram (*Baldwin et al.*, 1981), color coded for different distances from the midplane. Each axis on the plot is a line ratio in emission. The BPT diagram is commonly used to divide observed galaxies into those whose HII regions are primarily ionized by stars and those primarily ionized by an active-galactic nuclei (AGN). In other words, the dividing line on the BPT diagram separates galaxies into those ionized by a softer or harder spectrum respectively (*Veilleux and Osterbrock*, 1987). Figures 4.8, 4.9, and 4.10 show the time evolution of the resulting line ratio profiles in height for Si-IV/C-IV, N-V/O-VI, and C-II/C-IV respectively. For Si-IV/C-IV, we plot the observed Milky Way value of ~ 0.2. For N-V/O-VI, we plot lines bounding the range of observed values. For C-II/C-IV, we plot the mean value from *Fox et al.* (2005).

The BPT diagrams are useful in that they help summarize the properties of the ionizing radiation field, as well as ISM plasma conditions and metalicity (*Kewley et al.*, 2013a). The data points from 'k28' are below the typical star forming sequence, as expected by the lack of stellar radiation present in the run. The addition of only CR streaming heating in 'k28_Hcr' moves the data points vertically in O-III/Hβ, overlapping star forming sequence. The addition of stellar radiation for low CR transport speed tends to move the near-disk data points horizontally and narrows values in N-II/Hα. The higher CR transport simulations are both roughly around the star forming sequence, towards higher O-III/Hβ and lower N-II/Hα values than in the lower CR transport ones. The effect of streaming heating at this time in the simulations is higher N-II/Hα.

Many of the simulations over predict Si-IV/C-IV. The simulation 'k28' has the largest line ratio predictions, with Si-IV/C-IV $\sim 10^2$. The poor predictions of this simulation make sense as it has the least amount of physics included. The addition of

radiative effects in 'k28_Hrad' reduces the line ratio by a factor of 10 across the entire profile. The profile is also less variable in space and time than the profile from the 'k28' run. If we instead add CR streaming heating, as in the 'k28_Hcr' run, we see that the line ratio values are even lower, including a profile at 120 Myr that is below the observed value. The outflows in this run are more suppressed, as mentioned in Section 4.5, so this run does not entirely match the observed data that extends up to 15 kpc. At higher $\kappa_{\rm cr}$ the impact of CR streaming heating reverses: the run without $H_{\rm cr}$, 'k29_Hrad', is favored over 'k29_Hrad_Hcr'. The simulation 'k29_Hrad' shows both an extended outflow far out of the galaxy and the Si-IV/C-IV ratio approaches observed values.

The N-V/O-VI line ratio provides another metric to evaluate the simulations with. Values of this line ratio could favor particular underling physical processes, such as cooling flows, shock heating, or turbulent mixing. In this work, we simply use the range of values seen observationally, as summarized by *Wakker et al.* (2012), in order to broadly evaluate each model. The N-V and O-VI ions have a larger ionization potential than Si-IV and C-IV ions, so they trace gas phases well-above those directly influenced by radiative heating (i.e. see Figure 4.6). Generally the simulations favored for N-V/O-VI are the same ones favored for Si-IV/C-IV. The simulation that least matches the observed bounds is the 'k28' run, which has N-V/O-VI many orders of magnitude above the bounds. This behavior can be traced to the lack of $T \sim 10^{5-6}$ K (phase 5) gas. O-VI sharply peaks within phase 5 temperature range, so a severe lack of phase 5 gas produces large line ratios. As expected by the higher ionization potentials, adding radiative heating as in 'k28_Hrad' does not significantly improve results. The runs with CR streaming heating do have predicted line values near observed bounds. At higher $\kappa_{\rm cr}$, both runs with and without CR streaming heating produced reasonable N-IV/O-VI values.

C-II/C-IV traces lower temperature gas phases than the previous line ratios dis-

cussed. As before, the 'k28' over predicts the line ratio value (i.e. there is too much colder, neutral material). Adding CR streaming heating, results in profiles that are much closer to the example observations. The simulation 'k28_Hcr' (without radiative heating) in particular, produces values at 190 Myr that are quite close to the example observations, and is the only simulation at lower CR diffusivity that has an under predicting profile (120 Myr). This behavior could be due to the fact that this simulation uniquely has an outflow dominated by phase 3 gas (warm, neutral medium) as shown by the filling fraction in Figure 4.3. Of the simulations with higher CR diffusivity, the run 'k29_Hrad_Hcr' produces the best match to the observed line ratio values at 120 Myr, although not at 140 Myr.

4.8 Discussion

There is no strong preference in simulation type based on the BPT diagrams summarized in Figure 4.7. The diagrams showed that the inner 5 kpc of the galaxies (most comparable to the observed lines from the ISM of galaxies (e.g., *Kewley et al.*, 2013b) generally follow the star forming sequence, except 'k28' which explicitly excluded the stellar and metagalatic field. For some simulations, especially 'k28_Hrad', the regions farther out of the galaxy tend to cross the line between star forming and active galaxies. This is an indication that the spectra in these simulations are becoming harder with height, possibly due to higher photon absorption in the lower CGM. The fact that Figure 4.3 shows the dominant volume filling phase in 'k28_Hrad' is phase 3 (warm, neutral medium) supports this idea.

In our absorption line results, the importance of the CR streaming heating depends on the CR diffusivity. At $\kappa_{\rm cr} = 10^{28}$ cm^{2}s^{-1}, the simulations with CR streaming heating are favored over those without the collisionless heating based on the three line ratio diagnostics studied. At $\kappa_{\rm cr} = 10^{29}$ cm^{2}s^{-1}, the conclusion is reversed: the simulation with streaming heating, while closer to observations compared to the 'k28' set

of models, is less favored compared to the run without cosmic ray streaming heating. The predictions in the 'k29_Hrad' run match better than those in 'k29_Hrad_Hcr' for Si-IV/C-IV, but the conclusions are less clear for other diagnostics. The main difference between these simulations occurs due to the extent of the galactic outflow. In both 'k28' and 'k29' choices of CR diffusion, streaming heating removes enough energy from the CRs such that a weaker outflow occurs and predictions look worse compared to observations. One interpretation of this result is that CR confinement occurs not via self-confinement, but instead is due to extrinsic turbulence, which is not associated with collisionless plasma heating. There are many theoretical arguments regarding self-confinement versus extrinsic turbulence models that are outside the scope of this work (see for example *Yan and Lazarian*, 2002; *Blasi et al.*, 2012; *Zweibel*, 2013; *Xu*, 2021; *Kempski and Quataert*, 2021).

If CR streaming heating is indeed present in the real galactic environment, for high $\kappa_{\rm cr}$, there must be a mechanism for streaming heating suppression that our model does not take into account. Our resolution scale is above that of expected pc-scale clouds of dense material in the CGM (*Gronke and Oh*, 2018; *Farber and Gronke*, 2022), so we do not model phenomena at these small scales. According to the timescale of CR losses to collisionless heating in Eq. 4.19, the loss timescale is proportional to $L_{\rm cr}$, the length scale of the cosmic ray distribution, which locally can change significantly at the cloud interface. Proper accounting of energy losses due to CR streaming heating requires accurate modeling of cloud-scale physics. The path of the CR distribution through a turbulent, clumpy medium has been an active area of interest (e.g., *Wiener et al.*, 2017a, 2019; *Brüggen and Scannapieco*, 2020). For example, *Bustard and Zweibel* (2021) focused on the propagation of CRs through a clumpy medium, accounting for effects of cloud partial ionization. Cloud ionization can change where the CR gradient forms at cloud interfaces, influencing where significant collisionless heating occurs. Also, partial ionization, with associated ion-neutral transport enhancement of CRs,

allows CRs to more easily pass through clouds. Of course, in a more realistic model, the cloud ionization should be influenced by the stellar and metagalactic radiation field.

The dependence of results on CR diffusivity also demonstrates the necessity of more detailed CR transport models in order to better account for the impact of feedback effects on UV diagnostics. The improvement in the values of diagnostics at low CR diffusivity could indicate that CR streaming heating indeed improves line ratios, but only accompanied by a corresponding weaker wind. In a realistic system, the CR diffusivity could vary greatly on pc-scales as the cosmic rays traverse CGM inhomogeneities: for example, *Bustard and Zweibel* (2021) showed that the formation of CR bottlenecks depends on cloud ionization. The pressure anisotropy instability (*Zweibel*, 2020) may contribute to CR confinement in these environments. Other models of CR transport will similarly cause a cascade of coupled effects. For example, in the CR transport model studied in (*Holguin et al.*, 2019), CR transport is enhanced within roughly a kpc of the midplane due to turbulence, but is much less enhanced farther out of the disk where turbulence is weaker. This type of model causes enhanced star formation (and subsequent outflows powered by the stellar feedback) because CRs can more easily escape the dense disk. This model also reduces CR losses from dense gas, which leaves a greater reservoir of CR energy outside of the disk. Recent work has also investigated the potential significance of dust damping of Alfvén waves to cosmic ray confinement (*Squire et al.*, 2021). The properties of the galactic radiation field impact the subsequent coupling of dust to the CR system.

4.8.1 Caveats and Further Work

In the following list we describe potential caveats in our work and additional research directions:

- The observational values we use in Figures 4.8, 4.9, and 4.10 are meant as

rough guides to aid simulation comparison. These values can vary depending on the what objects are within the measurement line-of-sight. The synthetic line ratio data points from the simulations all most certainly trace a larger range of physical situations than would be traced by a particular observation (e.g. high velocity clouds).

- The values of synthetic UV diagnostics depend on SFR peaks that may be fluctuations. More work is needed to see how relevant these peaks are to changes in model assumptions.

- We do not focus on interstellar dust effects on the predicted line ratios. Dust preferentially reduces certain elements compared to others. Preferential depletion of Si onto dust will lower the Si-IV/C-IV ratio allowing some previously observationally inconsistent models to be viable, as *Werk et al.* (2019) notes. The exact depletion of elements relative to others is still debated. More detailed models of dust creation/destruction (e.g. *Oberg*, 2016) each can influence line diagnostics based on their own resulting elemental depletion.

- CR transport is an active area of research. More detailed work in plasma turbulence and charged particle transport, especially at spatial scales below which the fluid approximation for CRs holds, are needed in order to better understand the impact of CRs on global galaxy scales (e.g., *Bai*, 2022).

- We use a single cooling function assuming solar metalicity. We do not explicitly track ion species with the code, and we do not include non-equilibrium effects in the cooling.

- Our resolution is relatively limited compared to the scale of many important processes operating at the CGM cloud pc-scales. For example, we do not resolve turbulent mixing layers, cloud formation/destruction, or CR-cloud interaction.

- Our model of parallel-plane radiation propagation through the domain, especially with un-resolved CGM cloud structure, is a crude approximation of real ionizing photon transport through the galaxy and halo. This work is meant to be a proof-of-concept highlighting potential UV plasma diagnostics to use as metrics to evaluate models of cosmic ray and ionizing radiation within galactic simulations.

- In addition to our simulation domain being an approximation of a global galactic disk and halo, it is also not cosmological. Cosmological processes such as mergers and gas accretion are not present in our simulations.

4.9 Conclusions

We perform MHD simulations of a section of a galactic disk, focusing on addition of radiative heating and CR feedback. We test the effects of inclusion or absence of radiative heating, the value of CR transport parallel to the magnetic field ($\kappa_{\rm cr} = 10^{28}$ or 10^{29} cm^{2}s^{-1}), and the inclusion of collisionless CR streaming heating. We post-process the simulations using parallel-plane Cloudy models informed by the simulation results in order to produce synthetic observations of four UV diagnostics: the BPT diagram, Si-IV/C-IV, N-V/O-VI, and C-II/C-IV. We compare predicted UV diagnostics to observational values and evaluate the relative ability of the simulations to reproduce observations. Our conclusions are:

- The inclusion of radiative heating in simulations reduces synthetic Si-IV/C-IV values, bringing them closer to the observed value of 0.2. Radiative heating is unable to similarly improve the N-V/O-VI diagnostic predictions, due to the higher ionization potentials of the ions. Other mechanisms are needed to better match all of the UV diagnostics included in this work.

- The inclusion of CR streaming heating in our simulations reduces the strength of galactic outflows due to the additional energy losses of the CR population.
- In simulations with slower CR transport, the addition of CR streaming heating results in synthetic diagnostics values closer to observed values. However, slower CR transport results in a less extended outflow.
- The simulations with the inclusion of faster CR transport produce the closest predictions to observed UV diagnostics. Without CR streaming heating losses included in feedback, the outflows extend out to the edge of the domain at a height of 20 kpc above the midplane.
- The type of analysis presented in this proof-of-concept demonstrates the potential use of UV diagnostics as additional constraints on key galactic physical models that are currently not well understood, such as cosmic ray transport and feedback.

4.10 Townsend Cooling and Heating

The radiative cooling code using the Townsend method (*Townsend*, 2009) implemented in *Farber et al.* (2018); *Holguin et al.* (2019); *Farber et al.* (2022) is updated to include radiative heating. Figure 4.11 shows an isolated test of the radiative heating part of the code. The code reproduces the analytic result well.

4.11 Cosmic Ray Loss Model

We test our implementation of CR losses. We evolve a 1 kpc^3 box of uniform gas and CR density, with only the plasma-CR energy exchange due to CR hadronic and Coulomb losses included. The analytic solution of the simple differential equation of

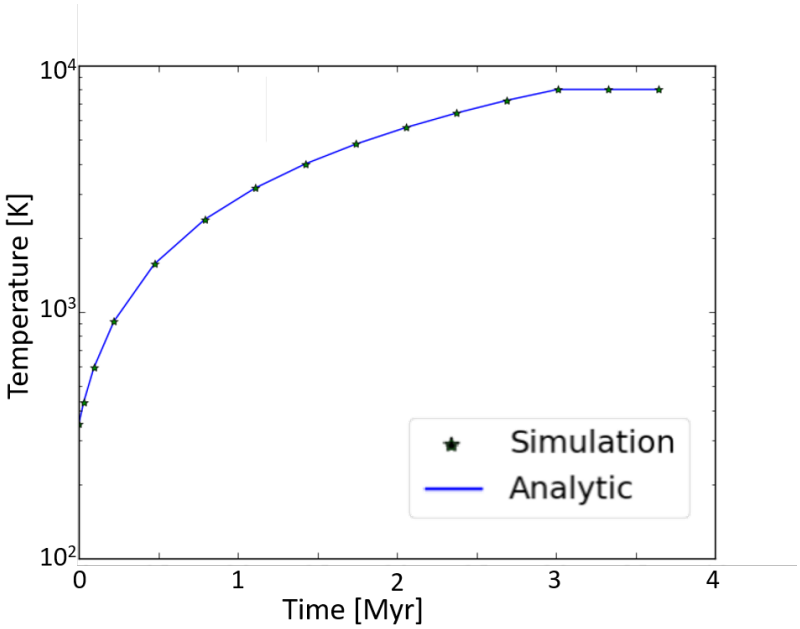

Figure 4.11: Evolution of gas temperature undergoing constant radiative heating. The simulated data fits the analytic prediction well.

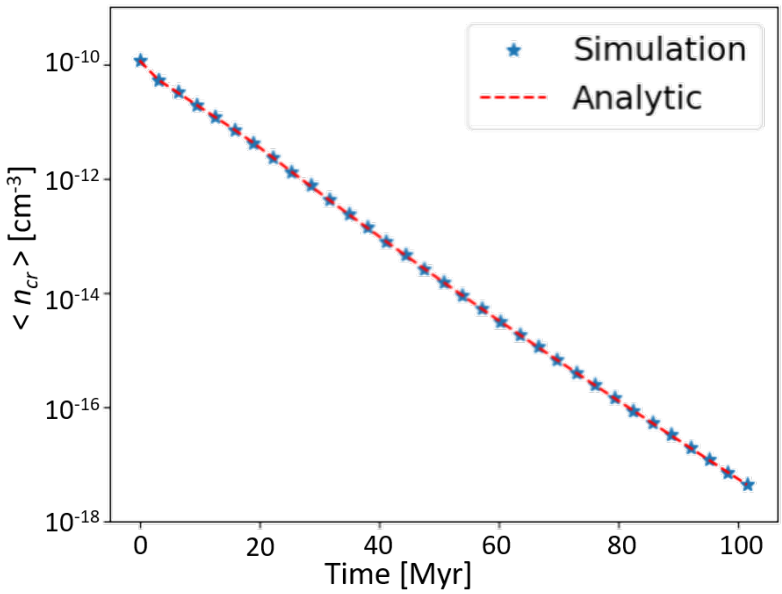

Figure 4.12: Evolution of mean $n_{\rm cr}$ within a 1 kpc^3 box of uniform gas and CR density. CR losses (hadronic and Coulomb) are the only energy transfer mechanism included, as gas radiative cooling is turned off. The evolution follows the analytic prediction closely.

the CR loss rate $\frac{\mathrm{de_{cr}}}{\mathrm{dt}}$ proportional to e_{cr} at fixed gas number density is

$$e_{\mathrm{cr}}(t) = e_{\mathrm{cr},0}\ \exp(\mathrm{t}/\tau_{\mathrm{cr}}), \tag{4.21}$$

where $e_{\mathrm{cr},0}$ is the initial CR energy density and τ_{cr} is the timescale for CR losses defined as $\Gamma_{\mathrm{cr}} = e_{\mathrm{cr}}/\tau_{\mathrm{cr}}$ from Eq. 4.14. The decay of n_{cr} in the simulation matches the analytic solution well.

CHAPTER V

Summary and Conclusions

5.1 Thesis Results Summary

In this thesis, I described results from an analysis of state-of-the-art cosmological galaxy simulations quantifying contribution of stars to the circumgalactic medium radiation field, and results from two sets of galactic disk simulations I conducted to target particular cosmic ray feedback mechanisms.

First, I focus on radiative feedback, another highly non-linear and computationally challenging physical mechanism. The stellar contribution to the radiation field is difficult to treat compared to the metagalactic component as local radiation sources vary spatially and temporally with the evolution of the galaxy. Many analyses of circumgalactic medium diagnostics suffer from degeneracies in properties of the underlying plasma. By quantifying the extent of stellar ionizing radiation around a galaxy, I am able to provide a guide for when analyses are justified in a simpler treatment of radiation by ignoring local sources, or if modeling local sources is needed for accurate results.

Using a Monte-Carlo radiative transfer (*Ma et al.*, 2020) I post-process 12 FIRE-2 (*Hopkins et al.*, 2018) state of the art cosmological galaxy simulations in the range of present day halo mass $M_{\rm vir} = [10^{11}, 10^{13}]M_{\odot}$ and redshift $z = [0, 3.5]$. I produce four runs per galaxy snapshot with varying assumptions in ionizing sources that allow

us to uncover the relative contribution from local and extragalctic sources: (i) full stellar and metagalactic photons included, (ii) suppressed stellar and full metagalactic photons included, (iii) only stellar photons and no attenuation, and (iv) only stellar photons, with attenuation from the updated gas structure in case (i). I find that for $z < 1.0$ and at all halo masses the stellar radiation field is dominant over the metagalactic field up to $\sim 0.1\ R_{\rm vir}$. At higher redshift $1 < z < 3.5$, the stellar radiation field extends up to $\sim 0.2\ R_{\rm vir}$. These findings aid both computational and observational future works in determining the relevant ionization processes in a particular region of interest for the work, for example simplifying analyses by including only the metagalactic field when focusing on the outer circumgalactic medium. I also estimate the escape fraction of photons through the circumgalactic medium and find that halos of $M_{\rm vir} > 10^{12}$ have can high escape fractions up to 0.5, although there is a lot of scatter.

Second, I explored the impact of physically-motivated cosmic ray transport within an elongated section of a Milky Way-like galactic disk. I extend the model of *Ruszkowski et al.* (2017), which assumed a cosmic ray streaming speed at fixed multiples of the Alfvén speed, by implementing cosmic ray transport that depends on the properties of the turbulent, magnetized galactic medium. In the self-confinement model of cosmic ray transport, Alfvén waves confine the bulk cosmic ray population. Turbulent motion damps these confining waves, allowing cosmic rays to stream faster along the magnetic field. I derive the cosmic ray transport speed using the *Lazarian* (2016) model of Alfvénic turbulence. I find that simulated galaxy and outflow properties are sensitive to the strength of turbulence assumed. Stronger turbulence leads to higher star formation rates, more extended outflows, and a suppressed instantaneous mass loading. These results underscore the need for improved descriptions of cosmic ray transport in order to obtain accurate galactic models.

Third, I run updated elongated slab magneotohydrodynamic simulations of a

galactic disk section. In analyses from the work I described first, I find that at inner-circumgalactic medium scales, we should consider radiative effects from stellar sources. I update our simulations to include a simplified, parallel-plane model of radiative heating. I further improve the realism of our simulations by adding momentum injection in supernova feedback and cosmic ray collisional losses. I narrow-in on three key limiting parameters: inclusion of radiative effects, cosmic ray diffusivity, and inclusion of collisionless gas heating due to cosmic ray streaming losses.

Ultraviolet diagnostics contain a wealth of information about the dynamical, thermal, and ionization state of circumgalactic medium. These diagnostics could be used to help constrain models of cosmic ray transport, in addition to traditional constraints such as gamma ray or radio emission. I couple the magnetohydrodynamic simulation results with the Cloudy spectral synthesis code in order to produce synthetic line diagnostics. I find that the inclusion of radiative effects reduces the Si-IV/C-IV line ratio, moving it closer to observed values; however, radiative effects do not similarly move N-V/O-VI closer to observed values, as the ionization potential of these ions is greater. In simulations with lower cosmic ray diffusivity ($\kappa_{\rm cr} = 10^{28}$ cm^{2}s^{-1}), the addition of cosmic ray streaming seems to move synthetic diagnostics in both Si-IV/C-IV and N-V/O-VI closer to observed ranges. Unfortunately, cosmic ray streaming also removes enough energy from cosmic rays that the outflows are weaker. Faster cosmic ray diffusivity ($\kappa_{\rm cr} = 10^{29}$ cm^{2}s^{-1}) results in stronger outflows. In these simulations, the model that does not include cosmic ray streaming heating produces closer results to Si-IV/C-IV and N-V/O-VI observations, although the model with cosmic ray heating included is still closer to observed line ratio values than predictions from lower cosmic ray diffusivity models.

5.2 Future Work

Current descriptions of cosmic ray transport still contain much uncertainty. This uncertainty propagates to the study of cosmic ray feedback in galaxies. *Hopkins et al.* (2021d) implemented an impressive number of cosmic ray transport model choices, including both extrinsic and self-confinement, ruling out many models based on γ-ray, 'grammage', and cosmic ray energy density. Within the allowed models, there is not a strong consensus: they all tend to produce galaxies that appear similar with respect to observables. The allowed cases with physically-motivated cosmic ray transport are not particularly unique. Additionally, there are follow-up arguments that these models are problematic with respect to constraints from the cosmic ray energy spectrum (*Hopkins et al.*, 2021c).

Interstellar/circumgalactic medium cloud scale ($\sim$ pc) simulations are especially important to explore. As briefly mentioned in Chapter 4, cosmic ray and radiative feedback properties can change greatly based on cloud-scale physics. For example, cosmic ray bottle necks at the interfaces of clouds have different properties depending on the ionization state of the cloud (*Bustard and Zweibel*, 2021). Results such as these underscore the need to further explore the cloud-scale interactions between cosmic ray and radiative feedback—two feedback mechanisms non-linearly coupled to the plasma ionization state. The continued development of efficient numerical methods and increasing computational power will allow these types of computational studies. The development of improved synthetic observation methods (e.g. *Hummels et al.*, 2017) is also of increasing importance, as they allow the realism of models to be evaluated.

Galactic simulations, as well as simulations of many other plasma physics systems, are headed towards using models better informed from targeted micro-scale investigations. Kinetic and hybrid (see *Caprioli*, 2015; *Shalaby et al.*, 2021; *Bai*, 2022) plasma simulations with cosmic rays are needed to further develop our understanding

of cosmic rays and their interaction with magnetized turbulence.

BIBLIOGRAPHY

BIBLIOGRAPHY

Aarseth, S. J., and F. Hoyle (1963), Dynamical evolution of clusters of galaxies, i, *Monthly Notices of the Royal Astronomical Society*, *126*(3), 223–255.

Accardo, L., et al. (2014), High statistics measurement of the positron fraction in primary cosmic rays of 0.5–500 gev with the alpha magnetic spectrometer on the international space station, *Physical review letters*, *113*(12), 121,101.

Ackermann, M., et al. (2012), Fermi-lat observations of the diffuse γ-ray emission: implications for cosmic rays and the interstellar medium, *The Astrophysical Journal*, *750*(1), 3.

Ackermann, M., et al. (2013), Detection of the characteristic pion-decay signature in supernova remnants, *Science*, *339*(6121), 807–811.

Agertz, O., A. V. Kravtsov, S. N. Leitner, and N. Y. Gnedin (2013), Toward a complete accounting of energy and momentum from stellar feedback in galaxy formation simulations, *The Astrophysical Journal*, *770*(1), 25.

Andrews, B. H., and T. A. Thompson (2011), Assessing radiation pressure as a feedback mechanism in star-forming galaxies, *The Astrophysical Journal*, *727*(2), 97.

Anglés-Alcázar, D., C.-A. Faucher-Giguère, D. Kereš, P. F. Hopkins, E. Quataert, and N. Murray (2017a), The cosmic baryon cycle and galaxy mass assembly in the fire simulations, *Monthly Notices of the Royal Astronomical Society*, *470*(4), 4698–4719.

Anglés-Alcázar, D., C.-A. Faucher-Giguère, E. Quataert, P. F. Hopkins, R. Feldmann, P. Torrey, A. Wetzel, and D. Kereš (2017b), Black holes on fire: stellar feedback limits early feeding of galactic nuclei, *Monthly Notices of the Royal Astronomical Society: Letters*, *472*(1), L109–L114.

Baade, W., and F. Zwicky (1934), Cosmic rays from super-novae, *Proceedings of the National Academy of Sciences*, *20*(5), 259–263.

Bai, X.-N. (2022), Toward first-principles characterization of cosmic-ray transport coefficients from multiscale kinetic simulations, *The Astrophysical Journal*, *928*(2), 112.

Baldwin, J. A., M. M. Phillips, and R. Terlevich (1981), Classification parameters for the emission-line spectra of extragalactic objects., *Publications of the Astronomical Society of the Pacific*, *93*(551), 5.

Barnes, J., and P. Hut (1986), A hierarchical o (n log n) force-calculation algorithm, *nature*, *324*(6096), 446–449.

Beck, R., and M. Krause (2005), Revised equipartition and minimum energy formula for magnetic field strength estimates from radio synchrotron observations, *Astronomische Nachrichten: Astronomical Notes*, *326*(6), 414–427.

Behroozi, P. S., R. H. Wechsler, and C. Conroy (2013), The average star formation histories of galaxies in dark matter halos from z= 0-8, *The Astrophysical Journal*, *770*(1), 57.

Bell, A. (1978), The acceleration of cosmic rays in shock fronts–i, *Monthly Notices of the Royal Astronomical Society*, *182*(2), 147–156.

Bell, A. (2013), Cosmic ray acceleration, *Astroparticle Physics*, *43*, 56–70.

Bell, E. F., D. H. McIntosh, N. Katz, and M. D. Weinberg (2003), A first estimate of the baryonic mass function of galaxies, *The Astrophysical Journal*, *585*(2), L117.

Bergström, L., and D. Hooper (2006), Dark matter and gamma rays from draco: Magic, glast and cactus, *Physical Review D*, *73*(6), 063,510.

Bland-Hawthorn, J., S. Veilleux, and G. Cecil (2007), Galactic winds: a short review, *Astrophysics and Space Science*, *311*(1), 87–98.

Blandford, R. D., and J. P. Ostriker (1978), Particle acceleration by astrophysical shocks, *The Astrophysical Journal*, *221*, L29–L32.

Blasi, P., E. Amato, and P. D. Serpico (2012), Spectral breaks as a signature of cosmic ray induced turbulence in the galaxy, *Physical Review Letters*, *109*(6), 061,101.

Boettcher, E., E. G. Zweibel, J. Gallagher III, and R. A. Benjamin (2016), Testing a dynamical equilibrium model of the extraplanar diffuse ionized gas in ngc 891, *The Astrophysical Journal*, *832*(2), 118.

Booth, C., O. Agertz, A. V. Kravtsov, and N. Y. Gnedin (2013), Simulations of disk galaxies with cosmic ray driven galactic winds, *The Astrophysical Journal Letters*, *777*(1), L16.

Boulares, A., and D. P. Cox (1990), Galactic hydrostatic equilibrium with magnetic tension and cosmic-ray diffusion, *The Astrophysical Journal*, *365*, 544–558.

Bourne, M. A., K. Zubovas, and S. Nayakshin (2015), The resolution bias: low-resolution feedback simulations are better at destroying galaxies, *Monthly Notices of the Royal Astronomical Society*, *453*(2), 1829–1842.

Brandenburg, A., and A. Lazarian (2013), Astrophysical hydromagnetic turbulence, *Space Science Reviews*, *178*(2), 163–200.

Breitschwerdt, D., J. McKenzie, and H. Voelk (1991), Galactic winds. i-cosmic ray and wave-driven winds from the galaxy, *Astronomy and Astrophysics*, *245*, 79–98.

Brüggen, M., and E. Scannapieco (2020), The launching of cold clouds by galaxy outflows. iv. cosmic-ray-driven acceleration, *The Astrophysical Journal*, *905*(1), 19.

Bryan, G. L., et al. (2014), Enzo: An adaptive mesh refinement code for astrophysics, *The Astrophysical Journal Supplement Series*, *211*(2), 19.

Bustard, C., and E. G. Zweibel (2021), Cosmic-ray transport, energy loss, and influence in the multiphase interstellar medium, *The Astrophysical Journal*, *913*(2), 106.

Bustard, C., E. G. Zweibel, and E. D'Onghia (2016), A versatile family of galactic wind models, *The Astrophysical Journal*, *819*(1), 29.

Butsky, I. S., D. B. Fielding, C. C. Hayward, C. B. Hummels, T. R. Quinn, and J. K. Werk (2020), The impact of cosmic rays on thermal instability in the circumgalactic medium, *The Astrophysical Journal*, *903*(2), 77.

Bykov, A., D. Ellison, A. Marcowith, and S. Osipov (2018), Cosmic ray production in supernovae, *Space Science Reviews*, *214*(1), 1–34.

Bykov, A. M. (2014), Nonthermal particles and photons in starburst regions and superbubbles, *The Astronomy and Astrophysics Review*, *22*(1), 1–54.

Caprioli, D. (2015), Cosmic-ray acceleration and propagation, *arXiv preprint arXiv:1510.07042*.

Casse, F., M. Lemoine, and G. Pelletier (2001), Transport of cosmic rays in chaotic magnetic fields, *Physical Review D*, *65*(2), 023,002.

Cen, R., and J. P. Ostriker (1992), Galaxy formation and physical bias, *The Astrophysical Journal*, *399*, L113–L116.

Cen, R., A. Jameson, F. Liu, and J. P. Ostriker (1990), The universe in a box-thermal effects in the standard cold dark matter scenario, *The Astrophysical Journal*, *362*, L41–L45.

Chan, T., D. Kereš, P. Hopkins, E. Quataert, K. Su, C. Hayward, and C. Faucher-Giguère (2019), Cosmic ray feedback in the fire simulations: constraining cosmic ray propagation with gev γ-ray emission, *Monthly Notices of the Royal Astronomical Society*, *488*(3), 3716–3744.

Chen, B. (1997), Comparisons of a galactic kinematic model with two proper-motion surveys in the vicinity of the north galactic pole, *The Astrophysical Journal*, *491*(1), 181.

Chevalier, R., and A. W. Clegg (1985), Wind from a starburst galaxy nucleus, *Nature*, *317*(6032), 44–45.

Clarke, C., and M. Oey (2002), Galactic porosity and a star formation threshold for the escape of ionizing radiation from galaxies, *Monthly Notices of the Royal Astronomical Society*, *337*(4), 1299–1308.

Cox, D. P. (2005), The three-phase interstellar medium revisited, *Annu. Rev. Astron. Astrophys.*, *43*, 337–385.

Cramer, N., F. Verheest, and S. Vladimirov (2002), The alfvén resonance in a dusty plasma with a distribution of grain sizes, *Physics of Plasmas*, *9*(12), 4845–4850.

Croton, D. J., et al. (2006), The many lives of active galactic nuclei: cooling flows, black holes and the luminosities and colours of galaxies, *Monthly Notices of the Royal Astronomical Society*, *365*(1), 11–28.

Cummings, A., E. Stone, B. Heikkila, N. Lal, W. Webber, G. Jóhannesson, I. Moskalenko, E. Orlando, and T. Porter (2016), Galactic cosmic rays in the local interstellar medium: Voyager 1 observations and model results, *The Astrophysical Journal*, *831*(1), 18.

Dalgarno, A., and R. McCray (1972), Heating and ionization of hi regions, *Annual review of astronomy and astrophysics*, *10*(1), 375–426.

De Avillez, M. A., and D. Breitschwerdt (2007), The generation and dissipation of interstellar turbulence: results from large-scale high-resolution simulations, *The Astrophysical Journal*, *665*(1), L35.

Diesing, R., and D. Caprioli (2018), Effect of cosmic rays on the evolution and momentum deposition of supernova remnants, *Physical review letters*, *121*(9), 091,101.

Dolag, K., and F. Stasyszyn (2009), An mhd gadget for cosmological simulations, *Monthly Notices of the Royal Astronomical Society*, *398*(4), 1678–1697.

Draine, B. T. (2010), *Physics of the interstellar and intergalactic medium*, vol. 19, Princeton University Press.

Dubey, A., L. Reid, and R. Fisher (2008), Introduction to flash 3.0, with application to supersonic turbulence, *Physica Scripta*, *2008*(T132), 014,046.

Dubois, Y., and R. Teyssier (2010), Magnetised winds in dwarf galaxies, *Astronomy & Astrophysics*, *523*, A72.

Efstathiou, G. (2000), A model of supernova feedback in galaxy formation, *Monthly Notices of the Royal Astronomical Society*, *317*(3), 697–719.

El-Badry, K., et al. (2018), Gas kinematics, morphology and angular momentum in the fire simulations, *Monthly Notices of the Royal Astronomical Society*, *473*(2), 1930–1955.

Eldridge, J., E. Stanway, L. Xiao, L. McClelland, G. Taylor, M. Ng, S. Greis, and J. Bray (2017), Binary population and spectral synthesis version 2.1: construction, observational verification, and new results, *Publications of the Astronomical Society of Australia*, *34*.

Everett, J. E., E. G. Zweibel, R. A. Benjamin, D. McCammon, L. Rocks, and J. S. Gallagher III (2008), The milky way's kiloparsec-scale wind: a hybrid cosmic-ray and thermally driven outflow, *The Astrophysical Journal*, *674*(1), 258.

Farber, R., M. Ruszkowski, H.-Y. Yang, and E. Zweibel (2018), Impact of cosmic-ray transport on galactic winds, *The Astrophysical Journal*, *856*(2), 112.

Farber, R. J., and M. Gronke (2022), The survival of multiphase dusty clouds in hot winds, *Monthly Notices of the Royal Astronomical Society*, *510*(1), 551–567.

Farber, R. J., M. Ruszkowski, S. Tonnesen, and P. Holguin (2022), Stress-testing cosmic ray physics: The impact of cosmic rays on the surviving disk of ram pressure stripped galaxies, *arXiv preprint arXiv:2201.04203*.

Farcy, M., J. Rosdahl, Y. Dubois, J. Blaizot, and S. Martin-Alvarez (2022), Radiation-magnetohydrodynamics simulations of cosmic ray feedback in disc galaxies, *Monthly Notices of the Royal Astronomical Society*.

Farmer, A. J., and P. Goldreich (2004), Wave damping by magnetohydrodynamic turbulence and its effect on cosmic-ray propagation in the interstellar medium, *The Astrophysical Journal*, *604*(2), 671.

Faucher-Giguere, C. A., A. Lidz, M. Zaldarriaga, and L. Hernquist (2009), *The Astrophysical Journal*, *703*, 1416.

Feldmann, R., P. F. Hopkins, E. Quataert, C.-A. Faucher-Giguere, and D. Kereš (2016), The formation of massive, quiescent galaxies at cosmic noon, *Monthly Notices of the Royal Astronomical Society: Letters*, *458*(1), L14–L18.

Ferland, G., et al. (2017), The 2017 release of cloudy, *RMxAA*, *53*(2).

Fermi, E. (1949), On the origin of the cosmic radiation, *Physical review*, *75*(8), 1169.

Field, G., D. Goldsmith, and H. Habing (1969), Cosmic-ray heating of the interstellar gas, *The Astrophysical Journal*, *155*, L149.

Fielding, D., E. Quataert, M. McCourt, and T. A. Thompson (2017), The impact of star formation feedback on the circumgalactic medium, *MNRAS*, *466*(4), 3810–3826.

Foote, E., and R. Kulsrud (1979), Hydromagnetic waves in high β plasmas, *Tech. rep.*, Princeton Univ.

Fox, A., and R. Davé (2017), *Gas accretion onto galaxies*, vol. 430, Springer.

Fox, A. J., B. P. Wakker, B. D. Savage, T. M. Tripp, K. R. Sembach, and J. Bland-Hawthorn (2005), Multiphase high-velocity clouds toward he 0226–4110 and pg 0953+ 414, *The Astrophysical Journal*, *630*(1), 332.

Fryxell, B., et al. (2000), Flash: An adaptive mesh hydrodynamics code for modeling astrophysical thermonuclear flashes, *The Astrophysical Journal Supplement Series*, *131*(1), 273.

Fumagalli, M., J. X. Prochaska, D. Kasen, A. Dekel, D. Ceverino, and J. R. Primack (2011), Absorption-line systems in simulated galaxies fed by cold streams, *Monthly Notices of the Royal Astronomical Society*, *418*(3), 1796–1821.

Galtier, S., S. Nazarenko, A. C. Newell, and A. Pouquet (2000), A weak turbulence theory for incompressible magnetohydrodynamics, *Journal of plasma physics*, *63*(5), 447–488.

Garrison-Kimmel, S., et al. (2017), Not so lumpy after all: modelling the depletion of dark matter subhaloes by milky way-like galaxies, *Monthly Notices of the Royal Astronomical Society*, *471*(2), 1709–1727.

Garrison-Kimmel, S., et al. (2019), The local group on fire: Dwarf galaxy populations across a suite of hydrodynamic simulations, *Monthly Notices of the Royal Astronomical Society*, *487*(1), 1380–1399.

Gentry, E. S., M. R. Krumholz, A. Dekel, and P. Madau (2017), Enhanced momentum feedback from clustered supernovae, *Monthly Notices of the Royal Astronomical Society*, *465*(2), 2471–2488.

Gentry, E. S., P. Madau, and M. R. Krumholz (2020), Momentum injection by clustered supernovae: testing subgrid feedback prescriptions, *Monthly Notices of the Royal Astronomical Society*, *492*(1), 1243–1256.

Giacalone, J. (1998), Cosmic-ray transport coefficients, in *Cosmic rays in the heliosphere*, pp. 351–363, Springer.

Gilmore, G., and N. Reid (1983), New light on faint stars–iii. galactic structure towards the south pole and the galactic thick disc, *Monthly Notices of the Royal Astronomical Society*, *202*(4), 1025–1047.

Girichidis, P., T. Naab, M. Hanasz, and S. Walch (2018), Cooler and smoother–the impact of cosmic rays on the phase structure of galactic outflows, *Monthly Notices of the Royal Astronomical Society*, *479*(3), 3042–3067.

Girichidis, P., et al. (2016), Launching cosmic-ray-driven outflows from the magnetized interstellar medium, *The Astrophysical Journal Letters*, *816*(2), L19.

Globus, N., and T. Piran (2017), The extragalactic ultra-high-energy cosmic-ray dipole, *The Astrophysical Journal Letters*, *850*(2), L25.

Gnedin, N. Y., and A. V. Kravtsov (2011), Environmental dependence of the kennicutt–schmidt relation in galaxies, *The Astrophysical Journal*, *728*(2), 88.

Goldreich, P., and S. Sridhar (1995), Toward a theory of interstellar turbulence. 2: Strong alfvenic turbulence, *The Astrophysical Journal*, *438*, 763–775.

Greengard, L., and V. Rokhlin (1987), A fast algorithm for particle simulations, *Journal of computational physics*, *73*(2), 325–348.

Grenier, I. A., J. H. Black, and A. W. Strong (2015), The nine lives of cosmic rays in galaxies, *Annual Review of Astronomy and Astrophysics*, *53*, 199–246.

Gronke, M., and S. P. Oh (2018), The growth and entrainment of cold gas in a hot wind, *Monthly Notices of the Royal Astronomical Society: Letters*, *480*(1), L111–L115.

Guedes, J., S. Callegari, P. Madau, and L. Mayer (2011), Forming realistic late-type spirals in a λcdm universe: the eris simulation, *The Astrophysical Journal*, *742*(2), 76.

Guo, F., and S. P. Oh (2008), Feedback heating by cosmic rays in clusters of galaxies, *Monthly Notices of the Royal Astronomical Society*, *384*(1), 251–266.

Guo, Q., S. White, C. Li, and M. Boylan-Kolchin (2010), How do galaxies populate dark matter haloes?, *Monthly Notices of the Royal Astronomical Society*, *404*(3), 1111–1120.

Haardt, F., and P. Madau (2012), Radiative transfer in a clumpy universe. iv. new synthesis models of the cosmic uv/x-ray background, *The Astrophysical Journal*, *746*(2), 125.

Hafen, Z., et al. (2019), The origins of the circumgalactic medium in the fire simulations, *Monthly Notices of the Royal Astronomical Society*, *488*(1), 1248–1272.

Haggerty, C. C., and D. Caprioli (2020), Kinetic simulations of cosmic-ray-modified shocks. i. hydrodynamics, *The Astrophysical Journal*, *905*(1), 1.

Hanasz, M., H. Lesch, T. Naab, A. Gawryszczak, K. Kowalik, and D. Wóltański (2013), Cosmic rays can drive strong outflows from gas-rich high-redshift disk galaxies, *The Astrophysical Journal Letters*, *777*(2), L38.

Hess, V. F. (1912), Uber beobachtungen der durchdringenden strahlung bei sieben freiballonfahrten, *Phys. Zeits.*, *13*, 1084–1091.

Higdon, J. (1984), Density fluctuations in the interstellar medium: Evidence for anisotropic magnetogasdynamic turbulence. i-model and astrophysical sites, *The Astrophysical Journal*, *285*, 109–123.

Hill, A. S., M. R. Joung, M. M. M. Low, R. A. Benjamin, L. M. Haffner, C. Klingenberg, and K. Waagan (2012), Vertical structure of a supernova-driven turbulent, magnetized ism, *The Astrophysical Journal*, *750*(2), 104.

Hillas, A. M. (2006), Cosmic rays: Recent progress and some current questions, *arXiv preprint astro-ph/0607109*.

Holguin, F., M. Ruszkowski, A. Lazarian, R. Farber, and H. K. Yang (2019), Role of cosmic-ray streaming and turbulent damping in driving galactic winds, *Monthly Notices of the Royal Astronomical Society*, *490*(1), 1271–1282.

Holguin, F., R. Farber, M. Ruszkowski, et al. (2022a), *In Prep*.

Holguin, F., C. Hayward, and X. o. Ma (2022b), Contribution of stars within the host galaxy to the ionizing radiation field of the circumgalactic medium, *In prep*.

Hopkins, P. F. (2015), A new class of accurate, mesh-free hydrodynamic simulation methods, *MNRAS*, *450*(1), 53–110.

Hopkins, P. F., E. Quataert, and N. Murray (2012), Stellar feedback in galaxies and the origin of galaxy-scale winds, *Monthly Notices of the Royal Astronomical Society*, *421*(4), 3522–3537.

Hopkins, P. F., D. Kereš, J. Oñorbe, C.-A. Faucher-Giguère, E. Quataert, N. Murray, and J. S. Bullock (2014), Galaxies on fire (feedback in realistic environments): stellar feedback explains cosmologically inefficient star formation, *Monthly Notices of the Royal Astronomical Society*, *445*(1), 581–603.

Hopkins, P. F., T. Chan, S. Garrison-Kimmel, S. Ji, K.-Y. Su, C. B. Hummels, D. Kereš, E. Quataert, and C.-A. Faucher-Giguère (2020), But what about...: cosmic rays, magnetic fields, conduction, and viscosity in galaxy formation, *Monthly Notices of the Royal Astronomical Society*, *492*(3), 3465–3498.

Hopkins, P. F., I. S. Butsky, G. V. Panopoulou, S. Ji, E. Quataert, C.-A. Faucher-Giguere, and D. Keres (2021a), First predicted cosmic ray spectra, primary-to-secondary ratios, and ionization rates from mhd galaxy formation simulations, *arXiv preprint arXiv:2109.09762*.

Hopkins, P. F., T. Chan, J. Squire, E. Quataert, S. Ji, D. Kereš, and C.-A. Faucher-Giguère (2021b), Effects of different cosmic ray transport models on galaxy formation, *Monthly Notices of the Royal Astronomical Society*, *501*(3), 3663–3669.

Hopkins, P. F., J. Squire, I. S. Butsky, and S. Ji (2021c), Standard self-confinement and extrinsic turbulence models for cosmic ray transport are fundamentally incompatible with observations, *arXiv preprint arXiv:2112.02153*.

Hopkins, P. F., J. Squire, T. Chan, E. Quataert, S. Ji, D. Kereš, and C.-A. Faucher-Giguère (2021d), Testing physical models for cosmic ray transport coefficients on galactic scales: self-confinement and extrinsic turbulence at gev energies, *Monthly Notices of the Royal Astronomical Society*, *501*(3), 4184–4213.

Hopkins, P. F., J. Squire, and I. S. Butsky (2022a), A consistent reduced-speed-of-light formulation of cosmic ray transport valid in weak-and strong-scattering regimes, *Monthly Notices of the Royal Astronomical Society*, *509*(3), 3779–3797.

Hopkins, P. F., et al. (2018), Fire-2 simulations: physics versus numerics in galaxy formation, *Monthly Notices of the Royal Astronomical Society*, *480*(1), 800–863.

Hopkins, P. F., et al. (2022b), Fire-3: Updated stellar evolution models, yields, & microphysics and fitting functions for applications in galaxy simulations, *arXiv preprint arXiv:2203.00040*.

Huang, X., and S. W. Davis (2022), The launching of cosmic ray-driven outflows, *Monthly Notices of the Royal Astronomical Society*, *511*(4), 5125–5141.

Hummels, C. B., B. D. Smith, and D. W. Silvia (2017), Trident: a universal tool for generating synthetic absorption spectra from astrophysical simulations, *The Astrophysical Journal*, *847*(1), 59.

Iacobelli, M., et al. (2013), Studying galactic interstellar turbulence through fluctuations in synchrotron emission-first lofar galactic foreground detection, *Astronomy & astrophysics*, *558*, A72.

Iapichino, L., M. Viel, and S. Borgani (2013), Turbulence driven by structure formation in the circumgalactic medium, *Monthly Notices of the Royal Astronomical Society*, *432*(3), 2529–2540.

Ipavich, F. M. (1975), Galactic winds driven by cosmic rays, *The Astrophysical Journal*, *196*, 107–120.

Irwin, J., et al. (2012), Continuum halos in nearby galaxies: an evla survey (chang-es). i. introduction to the survey, *The Astronomical Journal*, *144*(2), 43.

Jacob, S., R. Pakmor, C. M. Simpson, V. Springel, and C. Pfrommer (2018), The dependence of cosmic ray-driven galactic winds on halo mass, *Monthly Notices of the Royal Astronomical Society*, *475*(1), 570–584.

Jefferies, J. T. (1968), Spectral line formation, *A Blaisdell Book in the Pure and Applied Sciences, Waltham, Mass.: Blaisdell, 1968*.

Ji, S., T. Chan, C. B. Hummels, P. F. Hopkins, J. Stern, D. Kereš, E. Quataert, C.-A. Faucher-Giguère, and N. Murray (2020), Properties of the circumgalactic medium in cosmic ray-dominated galaxy haloes, *Monthly Notices of the Royal Astronomical Society*, *496*(4), 4221–4238.

Jiang, Y.-F., and S. P. Oh (2018), A new numerical scheme for cosmic-ray transport, *The Astrophysical Journal*, *854*(1), 5.

Joung, M. R., M.-M. Mac Low, and G. L. Bryan (2009), Dependence of interstellar turbulent pressure on supernova rate, *The Astrophysical Journal*, *704*(1), 137.

Kandel, D., A. Lazarian, and D. Pogosyan (2018), Statistical properties of galactic cmb foregrounds: dust and synchrotron, *Monthly Notices of the Royal Astronomical Society*, *478*(1), 530–540.

Kannan, R., E. Garaldi, A. Smith, R. Pakmor, V. Springel, M. Vogelsberger, and L. Hernquist (2022), Introducing the thesan project: radiation-magnetohydrodynamic simulations of the epoch of reionization, *Monthly Notices of the Royal Astronomical Society*, *511*(3), 4005–4030.

Katz, H. (2022), Ramses-rtz: non-equilibrium metal chemistry and cooling coupled to on-the-fly radiation hydrodynamics, *Monthly Notices of the Royal Astronomical Society*, *512*(1), 348–365.

Katz, N., and J. E. Gunn (1991), Dissipational galaxy formation. i-effects of gasdynamics, *The Astrophysical Journal*, *377*, 365–381.

Kempski, P., and E. Quataert (2021), Reconciling cosmic-ray transport theory with phenomenological models motivated by milky-way data, *arXiv preprint arXiv:2109.10977*.

Kennicutt Jr, R. C. (1998), The global schmidt law in star-forming galaxies, *The Astrophysical Journal*, *498*(2), 541.

Kewley, L. J., M. Dopita, R. Sutherland, C. Heisler, and J. Trevena (2001), Theoretical modeling of starburst galaxies, *The Astrophysical Journal*, *556*(1), 121.

Kewley, L. J., M. A. Dopita, C. Leitherer, R. Davé, T. Yuan, M. Allen, B. Groves, and R. Sutherland (2013a), Theoretical evolution of optical strong lines across cosmic time, *The Astrophysical Journal*, *774*(2), 100.

Kewley, L. J., C. Maier, K. Yabe, K. Ohta, M. Akiyama, M. A. Dopita, and T. Yuan (2013b), The cosmic bpt diagram: confronting theory with observations, *The Astrophysical Journal Letters*, *774*(1), L10.

Kim, C. G., and E. C. Ostriker (2017), Three-phase interstellar medium in galaxies resolving evolution with star formation and supernova feedback (tigress): Algorithms, fiducial model, and convergence, *The Astrophysical Journal*, *846*(2), 133.

Kim, C. G., and E. C. Ostriker (2018), Numerical simulations of multiphase winds and fountains from star-forming galactic disks. i. solar neighborhood tigress model, *The Astrophysical Journal*, *853*(2), 173.

Kim, C.-G., E. C. Ostriker, and R. Raileanu (2016), Superbubbles in the multiphase ism and the loading of galactic winds, *The Astrophysical Journal*, *834*(1), 25.

Kroupa, P. (2001), On the variation of the initial mass function, *Monthly Notices of the Royal Astronomical Society*, *322*(2), 231–246.

Krymskii, G. (1977), A regular mechanism for the acceleration of charged particles on the front of a shock wave, in *Akademiia Nauk SSSR Doklady*, vol. 234, pp. 1306–1308.

Kulsrud, R., and W. P. Pearce (1969), The effect of wave-particle interactions on the propagation of cosmic rays, *The Astrophysical Journal*, *156*, 445.

Kulsrud, R. M. (2005), Plasma physics for astrophysics, ed, *RM Kulsrud*.

Larson, R. B. (1974), Effects of supernovae on the early evolution of galaxies, *Monthly Notices of the Royal Astronomical Society*, *169*(2), 229–245.

Lazarian, A. (2016), Damping of alfvén waves by turbulence and its consequences: From cosmic-ray streaming to launching winds, *The Astrophysical Journal*, *833*(2), 131.

Lazarian, A., and E. T. Vishniac (1999), Reconnection in a weakly stochastic field, *The Astrophysical Journal*, *517*(2), 700.

Lazarian, A., and H. Yan (2014), Superdiffusion of cosmic rays: implications for cosmic ray acceleration, *The Astrophysical Journal*, *784*(1), 38.

Lee, D. (2013), A solution accurate, efficient and stable unsplit staggered mesh scheme for three dimensional magnetohydrodynamics, *Journal of Computational Physics*, *243*, 269–292.

Lee, D., and A. E. Deane (2009), An unsplit staggered mesh scheme for multidimensional magnetohydrodynamics, *Journal of Computational Physics*, *228*(4), 952–975.

Leitherer, C., H. C. Ferguson, T. M. Heckman, and J. D. Lowenthal (1995), The lyman continuum in starburst galaxies observed with the hopkins ultraviolet telescope, *The Astrophysical Journal*, *454*(1), L19.

Leitherer, C., D. Schaerer, J. D. Goldader, R. M. G. Delgado, C. Robert, D. F. Kune, D. F. de Mello, D. Devost, and T. M. Heckman (1999), Starburst99: synthesis models for galaxies with active star formation, *The Astrophysical Journal Supplement Series*, *123*(1), 3.

Li, J.-T., et al. (2016), Chang-es–vi. probing supernova energy deposition in spiral galaxies through multiwavelength relationships, *Monthly Notices of the Royal Astronomical Society*, *456*(2), 1723–1738.

Li, Y., G. L. Bryan, M. Ruszkowski, G. M. Voit, B. W. O'Shea, and M. Donahue (2015), Cooling, agn feedback, and star formation in simulated cool-core galaxy clusters, *The Astrophysical Journal*, *811*(2), 73.

Ma, X., D. Kasen, P. F. Hopkins, C.-A. Faucher-Giguère, E. Quataert, D. Kereš, and N. Murray (2015), The difficulty of getting high escape fractions of ionizing photons from high-redshift galaxies: a view from the fire cosmological simulations, *Monthly Notices of the Royal Astronomical Society*, *453*(1), 960–975.

Ma, X., E. Quataert, A. Wetzel, P. F. Hopkins, C.-A. Faucher-Giguère, and D. Kereš (2020), No missing photons for reionization: moderate ionizing photon escape fractions from the fire-2 simulations, *Monthly Notices of the Royal Astronomical Society*, *498*(2), 2001–2017.

Martizzi, D., C.-A. Faucher-Giguère, and E. Quataert (2015), Supernova feedback in an inhomogeneous interstellar medium, *Monthly Notices of the Royal Astronomical Society*, *450*(1), 504–522.

Martizzi, D., D. Fielding, C.-A. Faucher-Giguère, and E. Quataert (2016), Supernova feedback in a local vertically stratified medium: interstellar turbulence and galactic winds, *Monthly Notices of the Royal Astronomical Society*, *459*(3), 2311–2326.

Mathis, J. S. (1986), The photoionization of the diffuse galactic gas, *The Astrophysical Journal*, *301*, 423–429.

McCourt, M., P. Sharma, E. Quataert, and I. J. Parrish (2012), Thermal instability in gravitationally stratified plasmas: implications for multiphase structure in clusters and galaxy haloes, *MNRAS*, *419*(4), 3319–3337.

McKee, C. F., and E. C. Ostriker (2007), Theory of star formation, *Annu. Rev. Astron. Astrophys.*, *45*, 565–687.

McKee, C. F., and J. P. Ostriker (1977), A theory of the interstellar medium-three components regulated by supernova explosions in an inhomogeneous substrate, *The Astrophysical Journal*, *218*, 148–169.

McQuinn, M., and J. K. Werk (2018), Implications of the large o vi columns around low-redshift l galaxies, *The Astrophysical Journal*, *852*(1), 33.

Ménard, B., and M. Fukugita (2012), Cosmic dust in mg ii absorbers, *The Astrophysical Journal*, *754*(2), 116.

Moore, G. E. (1965), Cramming more components onto integrated circuits.

Mueller, D., S. P. Swordy, P. Meyer, J. L'Heureux, and J. M. Grunsfeld (1991), Energy spectra and composition of primary cosmic rays, *The Astrophysical Journal*, *374*, 356–365.

Muratov, A. L., D. Kereš, C.-A. Faucher-Giguère, P. F. Hopkins, E. Quataert, and N. Murray (2015), Gusty, gaseous flows of fire: galactic winds in cosmological simulations with explicit stellar feedback, *Monthly Notices of the Royal Astronomical Society*, *454*(3), 2691–2713.

Murray, N., E. Quataert, and T. A. Thompson (2005), On the maximum luminosity of galaxies and their central black holes: feedback from momentum-driven winds, *The Astrophysical Journal*, *618*(2), 569.

Murray, N., B. Ménard, and T. A. Thompson (2011), Radiation pressure from massive star clusters as a launching mechanism for super-galactic winds, *The Astrophysical Journal*, *735*(1), 66.

Nagashima, K., K. Fujimoto, and R. Jacklyn (1998), Galactic and heliotail-in anisotropies of cosmic rays as the origin of sidereal daily variation in the energy region¡ 104 gev, *Journal of Geophysical Research: Space Physics*, *103*(A8), 17,429–17,440.

Navarro, J. F., C. S. Frenk, and S. D. White (1997), A universal density profile from hierarchical clustering, *The Astrophysical Journal*, *490*(2), 493.

Newman, S. F., et al. (2012), The sins/zc-sinf survey of z 2 galaxy kinematics: outflow properties, *The Astrophysical Journal*, *761*(1), 43.

Oppenheimer, B. D., M. Segers, J. Schaye, A. J. Richings, and R. A. Crain (2018), Flickering agn can explain the strong circumgalactic o vi observed by cos-halos, *Monthly Notices of the Royal Astronomical Society*, *474*(4), 4740–4755.

Orr, M. E., C. C. Hayward, E. J. Nelson, P. F. Hopkins, C.-A. Faucher-Giguère, D. Kereš, T. Chan, D. M. Schmitz, and T. B. Miller (2017), Stacked star formation rate profiles of bursty galaxies exhibit "coherent" star formation, *The Astrophysical Journal Letters*, *849*(1), L2.

Orr, M. E., et al. (2020), Swirls of fire: spatially resolved gas velocity dispersions and star formation rates in fire-2 disc environments, *Monthly Notices of the Royal Astronomical Society*, *496*(2), 1620–1637.

Osterbrock, D. E., and G. J. Ferland (2006), *Astrophysics Of Gas Nebulae and Active Galactic Nuclei*, University science books.

Ostriker, E. C., C. F. McKee, and A. K. Leroy (2010), Regulation of star formation rates in multiphase galactic disks: a thermal/dynamical equilibrium model, *The Astrophysical Journal*, *721*(2), 975.

Oberg, K. I. (2016), Photochemistry and astrochemistry: Photochemical pathways to interstellar complex organic molecules, *Chemical Reviews*, *116*(17), 9631–9663.

Pacini, D. (1912), *La radiazione penetrante alla superficie ed in seno alle acque*, Stab. tip. Toscano.

Paglione, T. A., and R. D. Abrahams (2012), Properties of nearby starburst galaxies based on their diffuse gamma-ray emission, *The Astrophysical Journal*, *755*(2), 106.

Pakmor, R., C. Pfrommer, C. M. Simpson, and V. Springel (2016), Galactic winds driven by isotropic and anisotropic cosmic-ray diffusion in disk galaxies, *The Astrophysical Journal Letters*, *824*(2), L30.

Pandya, V., et al. (2021), Characterizing mass, momentum, energy, and metal outflow rates of multiphase galactic winds in the fire-2 cosmological simulations, *Monthly Notices of the Royal Astronomical Society*, *508*(2), 2979–3008.

Pellegrini, E. W., M. Oey, P. Winkler, S. Points, R. Smith, A. Jaskot, and J. Zastrow (2012), The optical depth of h ii regions in the magellanic clouds, *The Astrophysical Journal*, *755*(1), 40.

Peng, Y.-j., et al. (2010), Mass and environment as drivers of galaxy evolution in sdss and zcosmos and the origin of the schechter function, *ApJ*, *721*(1), 193.

Pfrommer, C. (2020), The physics of galaxy clusters, Accessed Ma.r 21, 2022 [online].

Pillepich, A., et al. (2018), Simulating galaxy formation with the illustristng model, *Monthly Notices of the Royal Astronomical Society*, *473*(3), 4077–4106.

Points, S., Y.-H. Chu, S. Snowden, and R. Smith (2001), Large-scale diffuse x-ray emission from the large magellanic cloud, *The Astrophysical Journal Supplement Series*, *136*(1), 99.

Pomerantz, M., and S. Duggal (1974), The sun and cosmic rays, *Reviews of Geophysics*, *12*(3), 343–361.

Raymond, J. C., D. P. Cox, and B. W. Smith (1976), Radiative cooling of a low-density plasma, *The Astrophysical Journal*, *204*, 290–292.

Reedy, R. C., J. R. Arnold, and D. Lal (1983), Cosmic-ray record in solar system matter, *Annual Review of Nuclear and Particle Science*, *33*(1), 505–538.

Reynolds, R., and D. Cox (1992), Heating the warm ionized medium, *The Astrophysical Journal*, *400*, L33.

Reynolds, R. J., L. Haffner, and S. Tufte (1999), Evidence for an additional heat source in the warm ionized medium of galaxies, *The Astrophysical Journal*, *525*(1), L21.

Rosdahl, J., J. Blaizot, D. Aubert, T. Stranex, and R. Teyssier (2013), Ramses-rt: radiation hydrodynamics in the cosmological context, *Monthly Notices of the Royal Astronomical Society*, *436*(3), 2188–2231.

Rosen, A., and J. N. Bregman (1995), Global models of the interstellar medium in disk galaxies, *The Astrophysical Journal*, *440*, 634.

Rozwadowska, K., F. Vissani, and E. Cappellaro (2021), On the rate of core collapse supernovae in the milky way, *New Astronomy*, *83*, 101,498.

Rubin, V. C., and W. K. Ford Jr (1970), Rotation of the andromeda nebula from a spectroscopic survey of emission regions, *The Astrophysical Journal*, *159*, 379.

Ruszkowski, M., H.-Y. K. Yang, and E. Zweibel (2017), Global simulations of galactic winds including cosmic-ray streaming, *The Astrophysical Journal*, *834*(2), 208.

Salem, M., and G. L. Bryan (2014), Cosmic ray driven outflows in global galaxy disc models, *Monthly Notices of the Royal Astronomical Society*, *437*(4), 3312–3330.

Sanderbeck, P. R. U., M. McQuinn, A. D'Aloisio, and J. K. Werk (2018), The sources of extreme ultraviolet and soft x-ray backgrounds, *The Astrophysical Journal*, *869*(2), 159.

Sansonetti, J. E., and W. C. Martin (2005), Handbook of basic atomic spectroscopic data, *Journal of physical and chemical reference data*, *34*(4), 1559–2259.

Savage, B. D., and B. P. Wakker (2009), The extension of the transition temperature plasma into the lower galactic halo, *The Astrophysical Journal*, *702*(2), 1472.

Schlickeiser, R., and F. Jenko (2010), Cosmic ray transport in non-uniform magnetic fields: consequences of gradient and curvature drifts, *Journal of plasma physics*, *76*(3-4), 317–327.

Schmidt, W., A. Almgren, H. Braun, J. Engels, J. Niemeyer, J. Schulz, R. Mekuria, A. Aspden, and J. Bell (2014), Cosmological fluid mechanics with adaptively refined large eddy simulations, *Monthly Notices of the Royal Astronomical Society*, *440*(4), 3051–3077.

Schure, K., A. Bell, L. O'C Drury, A. Bykov, et al. (2012), Diffusive shock acceleration and magnetic field amplification, *Space science reviews*, *173*(1), 491–519.

Sedov, L. I. (1946), Propagation of strong shock waves, *Journal of Applied Mathematics and Mechanics*, *10*, 241–250.

Segers, M. C., B. D. Oppenheimer, J. Schaye, and A. J. Richings (2017), Metals in the circumgalactic medium are out of ionization equilibrium due to fluctuating active galactic nuclei, *MNRAS*, *471*(1), 1026–1044.

Semenov, V. A., A. V. Kravtsov, and N. Y. Gnedin (2018), How galaxies form stars: the connection between local and global star formation in galaxy simulations, *The Astrophysical Journal*, *861*(1), 4.

Shalaby, M., T. Thomas, and C. Pfrommer (2021), A new cosmic-ray-driven instability, *The Astrophysical Journal*, *908*(2), 206.

Sharma, P., B. D. Chandran, E. Quataert, and I. J. Parrish (2009), Buoyancy instabilities in galaxy clusters: convection due to adiabatic cosmic rays and anisotropic thermal conduction, *The Astrophysical Journal*, *699*(1), 348.

Shen, S., P. Madau, J. Guedes, L. Mayer, J. X. Prochaska, and J. Wadsley (2013), The circumgalactic medium of massive galaxies at z 3: a test for stellar feedback, galactic outflows, and cold streams, *The Astrophysical Journal*, *765*(2), 89.

Simpson, C. M., R. Pakmor, F. Marinacci, C. Pfrommer, V. Springel, S. C. Glover, P. C. Clark, and R. J. Smith (2016), The role of cosmic-ray pressure in accelerating galactic outflows, *The Astrophysical Journal Letters*, *827*(2), L29.

Slavin, J. D., C. F. McKee, and D. J. Hollenbach (2000), Photoionization of galactic halo gas by old supernova remnants, *The Astrophysical Journal*, *541*(1), 218.

Smith, A., X. Ma, V. Bromm, S. L. Finkelstein, P. F. Hopkins, C.-A. Faucher-Giguère, and D. Kereš (2019), The physics of lyman α escape from high-redshift galaxies, *MNRAS*, *484*(1), 39–59.

Smith, R. W. (1982), *The expanding universe: Astronomy's' great debate', 1900-1931*, Cambridge University Press.

Somerville, R. S., and R. Davé (2015), Physical models of galaxy formation in a cosmological framework, *Annual Review of Astronomy and Astrophysics*, *53*, 51–113.

Songaila, A. (2001), The minimum universal metal density between redshifts of 1.5 and 5.5, *The Astrophysical Journal*, *561*(2), L153.

Sparre, M., C. C. Hayward, R. Feldmann, C.-A. Faucher-Giguère, A. L. Muratov, D. Kereš, and P. F. Hopkins (2017), (star) bursts of fire: observational signatures of bursty star formation in galaxies, *Monthly Notices of the Royal Astronomical Society*, *466*(1), 88–104.

Speagle, J. S., C. L. Steinhardt, P. L. Capak, and J. D. Silverman (2014), A highly consistent framework for the evolution of the star-forming "main sequence" from z 0-6, *The Astrophysical Journal Supplement Series*, *214*(2), 15.

Spitzer Jr, L. (1942), The dynamics of the interstellar medium. iii. galactic distribution., *The Astrophysical Journal*, *95*, 329.

Springel, V., et al. (2005), Simulations of the formation, evolution and clustering of galaxies and quasars, *nature*, *435*(7042), 629–636.

Squire, J., P. F. Hopkins, E. Quataert, and P. Kempski (2021), The impact of astrophysical dust grains on the confinement of cosmic rays, *Monthly Notices of the Royal Astronomical Society*, *502*(2), 2630–2644.

Sternberg, A., C. F. McKee, and M. G. Wolfire (2002), Atomic hydrogen gas in dark matter minihalos and the compact high-velocity clouds, *The Astrophysical Journal Supplement Series*, *143*(2), 419.

Stinson, G., A. Seth, N. Katz, J. Wadsley, F. Governato, and T. Quinn (2006), Star formation and feedback in smoothed particle hydrodynamic simulations–i. isolated galaxies, *Monthly Notices of the Royal Astronomical Society*, *373*(3), 1074–1090.

Stone, J. M., E. C. Ostriker, and C. F. Gammie (1998), Dissipation in compressible magnetohydrodynamic turbulence, *The Astrophysical Journal*, *508*(1), L99.

Strauss, R., and M. Potgieter (2014), Where does the heliospheric modulation of galactic cosmic rays start?, *Advances in Space Research*, *53*(7), 1015–1023.

Strickland, D. K., and T. M. Heckman (2009), Supernova feedback efficiency and mass loading in the starburst and galactic superwind exemplar m82, *The Astrophysical Journal*, *697*(2), 2030.

Strong, A. W., I. V. Moskalenko, and V. S. Ptuskin (2007), Cosmic-ray propagation and interactions in the galaxy, *Annu. Rev. Nucl. Part. Sci.*, *57*, 285–327.

Sur, S., E. Scannapieco, and E. C. Ostriker (2016), Galaxy outflows without supernovae, *The Astrophysical Journal*, *818*(1), 28.

Sutherland, R. S., and M. A. Dopita (1993), Cooling functions for low-density astrophysical plasmas, *The Astrophysical Journal Supplement Series*, *88*, 253–327.

Tasker, E. J., and G. L. Bryan (2006), Simulating star formation and feedback in galactic disk models, *The Astrophysical Journal*, *641*(2), 878.

Taylor, G. I. (1950), The formation of a blast wave by a very intense explosion i. theoretical discussion, *Proceedings of the Royal Society of London. Series A. Mathematical and Physical Sciences*, *201*(1065), 159–174.

Thomas, T., and C. Pfrommer (2019), Cosmic-ray hydrodynamics: Alfvén-wave regulated transport of cosmic rays, *Monthly Notices of the Royal Astronomical Society*, *485*(3), 2977–3008.

Thompson, T. A., E. Quataert, D. Zhang, and D. H. Weinberg (2016), An origin for multiphase gas in galactic winds and haloes, *Monthly Notices of the Royal Astronomical Society*, *455*(2), 1830–1844.

Townsend, R. (2009), An exact integration scheme for radiative cooling in hydrodynamical simulations, *The Astrophysical Journal Supplement Series*, *181*(2), 391.

Tumlinson, J., M. S. Peeples, and J. K. Werk (2017), The circumgalactic medium, *Annual Review of Astronomy and Astrophysics*, *55*, 389–432.

Uhlig, M., C. Pfrommer, M. Sharma, B. B. Nath, T. Enßlin, and V. Springel (2012), Galactic winds driven by cosmic ray streaming, *Monthly Notices of the Royal Astronomical Society*, *423*(3), 2374–2396.

Veilleux, S., and D. E. Osterbrock (1987), Spectral classification of emission-line galaxies, *The Astrophysical Journal Supplement Series*, *63*, 295–310.

Veilleux, S., G. Cecil, and J. Bland-Hawthorn (2005), Galactic winds, *Annu. Rev. Astron. Astrophys.*, *43*, 769–826.

Verner, D., G. Ferland, K. Korista, and D. Yakovlev (1996), Atomic data for astrophysics. ii. new analytic fits for photoionization cross sections of atoms and ions, *Astrophysical Journal*, *465*(1), 487–498.

Vogelsberger, M., S. Genel, V. Springel, P. Torrey, D. Sijacki, D. Xu, G. Snyder, D. Nelson, and L. Hernquist (2014), Introducing the illustris project: simulating the coevolution of dark and visible matter in the universe, *Monthly Notices of the Royal Astronomical Society*, *444*(2), 1518–1547.

Von Hoerner, S. (1963), Die numerische integration des n-körper-problems für sternhaufen, ii., *Zeitschrift fur Astrophysik*, *57*.

Wakker, B. P., B. D. Savage, A. J. Fox, R. A. Benjamin, and P. R. Shapiro (2012), Characterizing transition temperature gas in the galactic corona, *The Astrophysical Journal*, *749*(2), 157.

Walch, S., et al. (2015), The silcc (simulating the lifecycle of molecular clouds) project–i. chemical evolution of the supernova-driven ism, *Monthly Notices of the Royal Astronomical Society*, *454*(1), 238–268.

Wang, P., and T. Abel (2009), Magnetohydrodynamic simulations of disk galaxy formation: the magnetization of the cold and warm medium, *The Astrophysical Journal*, *696*(1), 96.

Weinberg, D. H., L. Hernquist, and N. Katz (1997), Photoionization, numerical resolution, and galaxy formation, *The Astrophysical Journal*, *477*(1), 8.

Weingartner, J. C., and B. Draine (2001a), Dust grain-size distributions and extinction in the milky way, large magellanic cloud, and small magellanic cloud, *The Astrophysical Journal*, *548*(1), 296.

Weingartner, J. C., and B. Draine (2001b), Photoelectric emission from interstellar dust: Grain charging and gas heating, *The Astrophysical Journal Supplement Series*, *134*(2), 263.

Wentzel, D. G. (1968), Hydromagnetic waves excited by slowly streaming cosmic rays, *The Astrophysical Journal*, *152*, 987.

Wentzel, D. G. (1974), Cosmic-ray propagation in the galaxy-collective effects, *Annual review of astronomy and astrophysics*, *12*, 71–96.

Werk, J. K., K. H. Rubin, H. V. Bish, J. Prochaska, Y. Zheng, J. M. O'Meara, D. Lenz, C. Hummels, and A. J. Deason (2019), The nature of ionized gas in the milky way galactic fountain, *The Astrophysical Journal*, *887*(1), 89.

Werk, J. K., et al. (2014), The cos-halos survey: physical conditions and baryonic mass in the low-redshift circumgalactic medium, *ApJ*, *792*(1), 8.

Wetzel, A. R., P. F. Hopkins, J.-h. Kim, C.-A. Faucher-Giguère, D. Kereš, and E. Quataert (2016), Reconciling dwarf galaxies with λcdm cosmology: simulating a realistic population of satellites around a milky way–mass galaxy, *The Astrophysical Journal Letters*, *827*(2), L23.

White, S. D., and M. J. Rees (1978), Core condensation in heavy halos: a two-stage theory for galaxy formation and clustering, *Monthly Notices of the Royal Astronomical Society*, *183*(3), 341–358.

Wiegert, T., et al. (2015), Chang-es. iv. radio continuum emission of 35 edge-on galaxies observed with the karl g. jansky very large array in d configuration—data release 1, *The Astronomical Journal*, *150*(3), 81.

Wiener, J., S. P. Oh, and F. Guo (2013a), Cosmic ray streaming in clusters of galaxies, *Monthly Notices of the Royal Astronomical Society*, *434*(3), 2209–2228.

Wiener, J., E. G. Zweibel, and S. P. Oh (2013b), Cosmic ray heating of the warm ionized medium, *The Astrophysical Journal*, *767*(1), 87.

Wiener, J., S. P. Oh, and E. G. Zweibel (2017a), Interaction of cosmic rays with cold clouds in galactic haloes, *Monthly Notices of the Royal Astronomical Society*, *467*(1), 646–660.

Wiener, J., C. Pfrommer, and S. P. Oh (2017b), Cosmic ray driven galactic winds: streaming of diffusion, *Monthly Notices of the Royal Astronomical Society*, *467*, 906–921.

Wiener, J., E. G. Zweibel, and M. Ruszkowski (2019), Cosmic ray acceleration of cool clouds in the circumgalactic medium, *Monthly Notices of the Royal Astronomical Society*, *489*(1), 205–223.

Wulf, T. (1910), About the radiation of high penetration capacity contained in the atmosphere, *Physikalische Zeitschrift*, *5*, 152–157.

Wunsch, R., S. Walch, F. Dinnbier, and A. Whitworth (2018), Tree-based solvers for adaptive mesh refinement code flash-i: gravity and optical depths, *Monthly Notices of the Royal Astronomical Society*, *475*(3), 3393–3418.

Xu, S. (2021), Diffusion of cosmic rays in mhd turbulence, *arXiv preprint arXiv:2110.08282*.

Xu, S., and A. Lazarian (2018), Resonance-broadened transit time damping of particles in mhd turbulence, *The Astrophysical Journal*, *868*(1), 36.

Yan, H., and A. Lazarian (2002), Scattering of cosmic rays by magnetohydrodynamic interstellar turbulence, *Physical review letters*, *89*(28), 281,102.

Yan, H., and A. Lazarian (2004), Cosmic-ray scattering and streaming in compressible magnetohydrodynamic turbulence, *The Astrophysical Journal*, *614*(2), 757.

Yan, H., and A. Lazarian (2008), Cosmic-ray propagation: nonlinear diffusion parallel and perpendicular to mean magnetic field, *The Astrophysical Journal*, *673*(2), 942.

Yang, H.-Y., M. Ruszkowski, P. Ricker, E. Zweibel, and D. Lee (2012), The fermi bubbles: supersonic active galactic nucleus jets with anisotropic cosmic-ray diffusion, *The Astrophysical Journal*, *761*(2), 185.

Yang, H. Y. K., and M. Ruszkowski (2017), The spatially uniform spectrum of the fermi bubbles the leptonic active galactic nucleus jet scenario, *The Astrophysical Journal*, *850*(1), 185.

Yang, H.-Y. K., M. Ruszkowski, and E. Zweibel (2013), The fermi bubbles: gamma-ray, microwave and polarization signatures of leptonic agn jets, *Monthly Notices of the Royal Astronomical Society*, *436*(3), 2734–2746.

Yoast-Hull, T. M., J. E. Everett, J. Gallagher, and E. G. Zweibel (2013), Winds, clumps, and interacting cosmic rays in m82, *The Astrophysical Journal*, *768*(1), 53.

Zaw, I., G. R. Farrar, and J. E. Greene (2009), Galaxies correlating with ultra-high energy cosmic rays, *The Astrophysical Journal*, *696*(2), 1218.

Zhang, D. (2018), A review of the theory of galactic winds driven by stellar feedback, *Galaxies*, *6*(4), 114.

Zhang, D., and T. A. Thompson (2012), Radiation pressure-driven galactic winds from self-gravitating discs, *Monthly Notices of the Royal Astronomical Society*, *424*(2), 1170–1178.

Zhu, Q., B. Smith, and L. Hernquist (2017), Gas cooling in hydrodynamic simulations with an exact time integration scheme, *Monthly Notices of the Royal Astronomical Society*, *470*(1), 1017–1025.

Zweibel, E. G. (2013), The microphysics and macrophysics of cosmic rays, *Physics of Plasmas*, *20*(5), 055,501.

Zweibel, E. G. (2017), The basis for cosmic ray feedback: Written on the wind, *Physics of Plasmas*, *24*(5), 055,402.

Zweibel, E. G. (2020), The role of pressure anisotropy in cosmic-ray hydrodynamics, *The Astrophysical Journal*, *890*(1), 67.

Zwicky, F. (1937), On the masses of nebulae and of clusters of nebulae, *The Astrophysical Journal*, *86*, 217.

Zwicky, F. (1939), Cosmic rays from supernovae, *Physical Review*, *55*(10), 986.